21105

NATIONAL LIBRARY
OTTAWA

BIBLIOTHÈQUE NATIONALE
OTTAWA

CANADA

NAME OF AUTHOR........GEORGE E.E. SEDGWICK........

TITLE OF THESIS........CW CO2 LASER SYSTEMS
........POWERED BY TRANSVERSE
........ELECTRICAL DISCHARGES

UNIVERSITY..of ALBERTA........

DEGREE FOR WHICH THESIS WAS PRESENTED........PH.D.........

YEAR THIS DEGREE GRANTED........1974........

Permission is hereby granted to THE NATIONAL LIBRARY OF CANADA to microfilm this thesis and to lend or sell copies of the film.

The author reserves other publication rights, and neither the thesis nor extensive extracts from it may be printed or otherwise reproduced without the author's written permission.

(Signed)....G.E. Sedgwick...

PERMANENT ADDRESS:

905 Michener Pk
Edmonton, Alta
c/o DEP'T of ELECTRICAL
ENGINEERING.

DATED..April 23....1974.

NL-91 (10-68)

THE UNIVERSITY OF ALBERTA

CW CO_2 LASER SYSTEMS POWERED BY TRANSVERSE ELECTRICAL DISCHARGES

by

© GEORGE E. E. SEDGWICK

A THESIS

SUBMITTED TO THE FACULTY OF GRADUATE STUDIES AND RESEARCH

IN PARTIAL FULFILMENT OF THE REQUIREMENTS FOR THE DEGREE

OF DOCTOR OF PHILOSOPHY

DEPARTMENT OF ELECTRICAL ENGINEERING

EDMONTON, ALBERTA

SPRING, 1974

UNIVERSITY OF ALBERTA

FACULTY OF GRADUATE STUDIES AND RESEARCH

The undersigned certify that they have read, and recommend to the Faculty of Graduate Studies and Research for acceptance, a thesis entitled CW CO_2 LASER SYSTEMS POWERED BY TRANSVERSE ELECTRICAL DISCHARGES submitted by George E. E. Sedgwick in partial fulfilment of the requirements for the degree of Doctor of Philosophy.

. . . .
Supervisor

. . . .

. . . .

. . . .

. . . .

William P. Judd
. . . .
External Examiner

Date December 3, 1973

ABSTRACT

The results of an experimental and theoretical investigation are presented for CW CO_2 lasers powered by a DC glow discharge *transverse* to the laser axis. Related topics and research are reviewed in the first part of this thesis.

In the initial phase, a laser was constructed in which a DC cold-cathode glow discharge was established between a strip anode and a multi-element cathode arranged across a rectangular cavity, *transverse* to the laser axis. Gas flow was *open-cycle*, *low velocity*, and *collinear* with the laser axis. Incorporation of a wire mesh grid between anode and cathode raised the laser gain and power by a factor of two to three. V-I characteristics are illustrated. The effect of cathode-fall on laser efficiency is emphasized.

In the second phase, a multi-electrode DC *transverse* discharge laser was designed and constructed employing *high-velocity closed-cycle* flow *transverse* to the laser and discharge axes. Heat removal by convective cross-flow raised the laser power and efficiency by an order of magnitude over diffusion-dominated flow. Interaction of the discharge and flow is described. Theoretical gain calculations are compared with experiment.

ACKNOWLEDGMENT

The author wishes to acknowledge the assistance provided by Dr. H.J. Seguin during the course of this thesis. Assistance from others, particularly the workshop staff, is also gratefully acknowledged.

The work described in this thesis was carried out under support from the National Research Council of Canada and Defence Research Board of Canada whose assistance is gratefully acknowledged.

The author also extends a special acknowledgment to his wife, Mary, whose diligence and patience during the course of this thesis and the typing of the manuscript are greatly appreciated.

TABLE OF CONTENTS

Page

CHAPTER 1 INTRODUCTION 1

1.1 Electrical Excitation of CW CO_2 Lasers 1

1.2 Glow Discharge Phenomena 3

1.3 Energy Transfer Processes 12

1.4 The Effects of Discharge-Induced Gas Composition Changes 20

1.5 Scope of the Thesis 25

References 27

CHAPTER 2 TRANSVERSE EXCITATION WITH AXIAL GAS FLOW 36

2.1 Introduction 36

2.2 Glow Discharge Model with Grid 38

2.3 Experimental System 44

2.4 Characteristics of the Glow Discharge 47

2.5 Small Signal Amplification 69

2.6 Laser Output Power 76

2.7 The Variation of Output Intensity with Flow Rate 80

Page

2.8 Measurements of Gas Temperature and Ion Saturation Current 83

2.9 The Relationship of Maximum Laser Power to the V-I Characteristic 87

2.10 Transverse Discharge with Low Velocity Cross-Flow 91

2.11 Summary 93

References 97

CHAPTER 3 TRANSVERSE EXCITATION WITH HIGH VELOCITY CROSS-FLOW 101

3.1 Introduction 101

3.2 Theoretical Analysis of the Cross-Flow Laser System 105

3.3 Experimental System 125

3.4 Correlation of Side-Light Measurements with V-I Characteristics 141

3.5 Translational Temperature Profiles 147

3.6 Measurements of Ionization Density 151

3.7 Experimental Spatial Small-Signal Gain Profiles 164

Page

3.8 Comparison of Theoretical and Experimental Small-Signal Gains 172

3.9 Laser Output Power 185

References 195

Appendix 3-1 Electron Density of the Cross-flow Laser Plasma 207

Appendix 3-2 Design of a Single-ended Positive Branch Unstable Resonator 211

CHAPTER 4 CONCLUSIONS AND SUGGESTIONS FOR FUTURE RESEARCH 214

4.1 Summary of Results and Conclusions 214

4.2 Suggestions for Future Research 222

LIST OF TABLES

		Page
Table 2.1	Experimental Parameters for Typical Thermocouple and Electrostatic Probe Scans of Figure 2.20	93
Table 2.2	Summary of Axial-Flow Box Laser	103
Table 3.1	CO_2 Vibrational Relaxation Rate Coefficients	124
Table 3.2	Effective Electron Excitation Rates at 2eV	125
Table 3.3	Details of Anode Assembly for Cross-Flow System	130
Table 3.4	Details of Multiple Hollow-Cathode Assembly for Cross-Flow System	133
Table 3.5	Thermocouple, Pitot-Static, and Electrostatic Probe Details	137
Table 3.6	Probe and Plasma Parameters	159

LIST OF FIGURES

		Page
FIGURE 1.1	Longitudinal and Transverse Glow Discharges	4
FIGURE 1.2	Vibrational Energy Level Diagram of the Low-Lying Levels of CO_2, N_2, CO, and O_2	13
FIGURE 2.1(a)	Schematic Diagram of Experimental Laser	45
FIGURE 2.1(b)	Transverse Discharge Laser	46
FIGURE 2.2	V-I Characteristic for Isolated Grids	48
FIGURE 2.3	Transverse Discharge with 16 - Mesh Grids	50
FIGURE 2.4	Variation of V-I Characteristic with Grid to Cathode Separation, d_{GC}	52
FIGURE 2.5	V-I Characteristic Curves for Constant Grid to Cathode Potentials and 16 - Mesh Grids	54
FIGURE 2.6	Variation of Grid Current with Discharge Current and Parameter V_{GC}	55
FIGURE 2.7	V-I Characteristic Curves for Constant V_{GC} and 10 - Mesh Grids	57

		Page
FIGURE 2.8	V-I Characteristic with Parameter V_{GC} for 14-Mesh Grid	58
FIGURE 2.9	V-I Characteristic with Parameter V_{GC} for 20-Mesh Grid	59
FIGURE 2.10	V-I Characteristic for Self-Biased Grid	62
FIGURE 2.11	Variation of V-I Characteristics with Total Pressure for an Isolated Grid	64
FIGURE 2.12	Cross-Section of Various Cathode Electrodes Tested	66
FIGURE 2.13	V-I Characteristics of Various Cathode Materials without Grids	69
FIGURE 2.14	Experimental Set-Up for Recording Small-Signal Gain of Transverse Discharge Axial Flow Laser	71
FIGURE 2.15	The Discharge Current Dependence of the Small-Signal Gain for Various Isolated Grid Positions	72
FIGURE 2.16	Current Variation of the Small-Signal Gain with Gas Pressure for an Isolated Grid at Constant d_{GC}	74

		Page
FIGURE 2.17	Multimode Output Power Versus Total Discharge Current for Various Isolated Grid Positions	77
FIGURE 2.18	Multimode Output Power for Self-Biased Grids	79
FIGURE 2.19(a)	The Variation of Output Power with Total Discharge Current for Various Flow Rates	81
FIGURE 2.19(b)	The Variation of Output Power with Flow Rate	82
FIGURE 2.20(a)	Schematic of Thermocouple and Electrostatic Probe Scanning Arrangement	84
FIGURE 2.20(b)	Spatial Variation of Gas Temperature and Electrostatic Probe Current Operating in the Ion-Saturation Regime	84
FIGURE 2.21	The Relationship of Laser Power, Gas Temperature, and Positive Glow Potential with Single Electrode Discharge Current	88
FIGURE 2.22	The Variation of the Reduced Field (E/N) and Reduced Average Electron Energy ($\bar{u}_r$) with Discharge Current for Constant d_{GC}	90

Page

FIGURE 2.23 Comparison of Output Power Versus Discharge Current for Axial and Cross Flows 92

FIGURE 3.1(a) Diagram of High-Velocity Cross-Flow Laser 126

FIGURE 3.1(b) Side Elevation of Experimental Laser 127

FIGURE 3.1(c) Top View 127

FIGURE 3.2 Cross-Sections of Electrode Structures Employing a Continuous Convex Cathode and a Single Row of Hollow Cathodes 129

FIGURE 3.3 Diagram of Multiple Row Electrode Assembly 132

FIGURE 3.4 (a) Probe Configuration as Viewed Along the Laser Axis
(b) Diagram of Radial Sweep of Langmuir and Thermocouple Probes 135

FIGURE 3.5 Visual Changes of the Positive Column with Flow Velocity 142

FIGURE 3.6 Variation of Discharge Potential with Flow Velocity 146

FIGURE 3.7 Translation Temperature Variation Across the Laser Cavity for Various Gas Flow Velocities 148

Page

FIGURE 3.8 Ion-Saturation Current to a Cylindrical Electrostatic Probe Normal to the Flow 153

FIGURE 3.9 Variation of Ion-Saturation Current in Direction of Flow 155

FIGURE 3.10 Calculated Spatial Profiles of the Electron Density along the Channel Centerline in the Direction of Flow 162

FIGURE 3.11 Experimental Arrangement for Recording Spatial Gain Profiles of the Cross-Flow Laser 165

FIGURE 3.12 Horizontal Gain Profiles 166

FIGURE 3.13 The Variation of Small-Signal Gain with Discharge Current for Various Positions of the Probe Beam Between the Electrodes 168

FIGURE 3.14 The Spatial Variation of Small-Signal Gain with Gas Flow Velocity 170

FIGURE 3.15 The Variation of Small-Signal Gain with Discharge Current for Various Flow Rates 171

FIGURE 3.16(a) Calculated Small-Signal Gain Coefficient and Translational Temperature Compared with Experiment for a Centerline Flow Velocity of 35m/sec. 177

Page

FIGURE 3.16(b) Computed Gain Coefficient and Translational Temperature compared with Experiment for a Centerline Flow Velocity of Approximately 75m/sec. 178

FIGURE 3.17 Calculated Small-Signal Gain Coefficient as a Function of the Effective Excitation Product at the Spatial Peak of the Electron Pump. 180

FIGURE 3.18 The Variation of the Calculated Small-Signal Gain Coefficient with Centerline Gas Velocity for Constant Discharge Current 183

FIGURE 3.19 Schematic of the Unstable Resonator 186

FIGURE 3.20 Laser Power Versus Electrical Input Power for Various Externally Coupled Resonators and Flow Conditions 188

FIGURE 3.21 Multimode Laser Power as a Function of Flow Velocity for Constant Discharge Current 190

FIGURE 3.22 Laser Power and Efficiency Versus Discharge Input Power for an Internal Two-Path Resonator 192

LIST OF SYMBOLS

c_p - specific heat at constant pressure

d - grid sheath thickness

d_c - cathode fall distance

d_{AC} - anode to cathode distance

d_{GC} - grid to cathode distance

e - vibrational instantaneous specific energy

E - electric field strength

e^* - equilibrium specific vibrational energy

e_L - specific energy given to radiation field

e_E - specific electrical input energy

f_{ep} - electron pump spatial function

f_i - fundamental frequency of vibration of mode i

f_L - frequency of laser radiation

H - height of channel

I_c - intensity of intra-cavity radiation field

I_D - discharge current

I_i - total ion current collected by electrostatic probe

j_i - random ion current density

k_{ij} - rate constant for collisional relaxation

K_{io} - effective electron vibrational deactivation rate

K_{oi} - effective electron vibrational excitation rate to mode i

K_R - ratio of electron deactivation and excitation rates

ℓ_p - electrostatic probe length

L - resonator length

L_a - length of active medium along laser axis

M - Mach number; resonator magnification factor; molecular weight.

N - total number density of neutrals

N_i - number density of vibrational mode i

N_s - number density of neutral species s

N_{eq} - equivalent Fresnel number

n_i - ion number density

n_e - electron number density

p - static gas pressure

p_o - stagnation or total gas pressure

$P(J)$- rotational distribution function of upper laser level

Q - input power per unit width of flow channel

Q_i - molecular partition functions

Q_{s-CO_2} collision cross-section for rotational relaxation of CO_2 by species s.

R - reflectivity of output mirror

R_e - electric Reynold's number

T - translational or free-stream gas temperature

T_o - stagnation gas temperature

T_1 - vibrational temperature of CO_2 symmetric mode

T_2 - vibrational temperature of CO_2 bending mode

T_3 - vibrational temperature of CO_2 asymmetric mode

T_4 - vibrational temperature of N_2

T_5 - vibrational temperature of CO

T_e - electron temperature

T_i - ion temperature

u - gas flow velocity

$\bar{u}_r$ - reduced average electron energy; equals 2/3 of average energy

V - probe to plasma potential or probe bias

V_C - cathode fall potential

V_D - discharge potential

V_F - floating or isolated potential

V_G - grid to plasma potential

V_n - normal cathode fall potential

V_{GC} - grid to cathode potential

v_D - electron drift velocity

X_R - stimulated emission cross-section

z - distance in flow direction

z_p - position of peak electron pump

α - ratio of Debye length and probe diameter

γ - coefficient for secondary emission; ratio of gas specific heats

δ - dissociation fraction

δ_c - radiation output coupling fraction

Θ_i - characteristic temperature of vibrational mode i

θ_J - multiplicity of the upper laser level

λ_D - plasma Debye length

λ_i - ionic mean free path

λ_L - laser wavelength

μ_i - ionic mobility

ρ - gas mass density

τ - collisional relaxation time

τ_s - spontaneous emission lifetime of upper laser level

χ - normalized probe potential

Ψ_s - mole fractions of species s

CHAPTER 1

INTRODUCTION

1.1 Electrical Excitation of CW CO_2 Lasers

The electrical glow discharge is an effective means of excitation of the CO_2 laser as shown by the early experiments of Patel [1].* Since that time considerable research has been conducted into the improvement of the volumetric efficiency, that is, increasing the output power per unit volume of active medium. The aim is the development of a compact, efficient high-power laser of many kilowatts for industrial applications. Initially high output powers were achieved by construction of long cylindrical tubes requiring many kilovolts of potential for operation. Gas heating of the central core maintained an approximately constant output power with diameter [2], consequently, higher output powers were achieved by adding sections to an already long system [3]. Attempts were made by Freiberg and Clark [4] and Sedgwick and Seguin [5] to reduce the high running potentials by providing excitation perpendicular to the laser axis. Discharge instabilities, however, forced the use of segmented electrode structures. As a result active volume was sacrificed for the low voltage operation.

The CO_2 laser process is a strong function of gas temperature. The translational temperature has to be low to prevent thermal population of the lower laser level which leads to a decrease in the population inversion and output power. To increase the efficiency of heat transfer convective removal of the heated gas was demonstrated by Tiffany, Targ and Foster [6] with a cross-flow system using relatively low flow velocities. The cross-flow technique resulted in at least an order of magnitude improvement in the volumetric efficiency. An additional feature of this system was the use of closed-cycle flow which for industrial applications is of considerable economic importance.

---

* Numbers in [ ] refer to references listed at the end of the Chapter. References are listed in the order in which they appear in the text.

Since that time many schemes have been attempted to effectively couple the electrical energy into the flowing gas mixture. Buczek et al [7] used a longitudinal discharge, that is, along the laser axis, stabilized against the transverse flow by a small magnetic field. Brown [8] demonstrated an electric discharge mixing laser in which cool CO_2 was mixed into the high velocity flow downstream of the electrical discharge and just upstream of the resonator. This scheme, however, is probably limited to open cycle flow. Hill [9] used aerodynamic techniques to stabilize a large volume multiple-electrode excitation established in the direction of flow. A closed-cycle system was designed to operate at output powers in the 20 KW range. Finally Seguin and Sedgwick [10] adapted a multiple-electrode arrangement transverse to both the flow and the laser axis. This feature exploited both the low velocity convective heat removal and the low running potential of transverse excitation.

1.2 Glow Discharge Phenomena

Since most of the investigations of this thesis were concerned with cold-cathode glow discharges some of the pertinent aspects are outlined in the following paragraphs. Glow discharges are comprehensively reviewed by von Engel [11], Francis [12], and Cobine [13].

First, the visible light from a low pressure D.C. discharge in a long tube is divided into several more or less distinct regions as indicated diagrammatically in Figure 1.1(a). Beginning at the cathode successive regions are labelled: 1 - Aston dark space; 2 - cathode glow; 3 - cathode dark space; 4 - Negative glow; 5 - Faraday dark space; 6 - positive column; 7 - anode dark space; 8 - anode glow. As the gas pressure is raised to a few millimeters, regions 1,2,3, and 7 have contracted toward the electrodes to such an extent that the tube is filled by the negative glow, the Faraday dark space, the positive column, and the anode glow. For a long tube the positive column fills most of the length.

1.2.1 *Negative Glow and Faraday Dark Space*

For the experimental gas pressure of Chapter 2, typically 10mm, the cathode dark space was very thin and the negative glow appeared to cover the cathodes. The negative glow extended outwards to a distance governed by the cathode material, electrode surface condition, gas constituents, gas density and the discharge current. As indicated in Figure 1.1(d) a relatively large cathode-fall potential, V_c, occurs across the cathode-fall distance, d_c. V_c is produced by a positive space charge in the cathode dark space. This space charge accelerates electrons leaving the cathode to produce sufficient ionization that each electron is replaced by positive-ion bombardment of the cathode. This requires

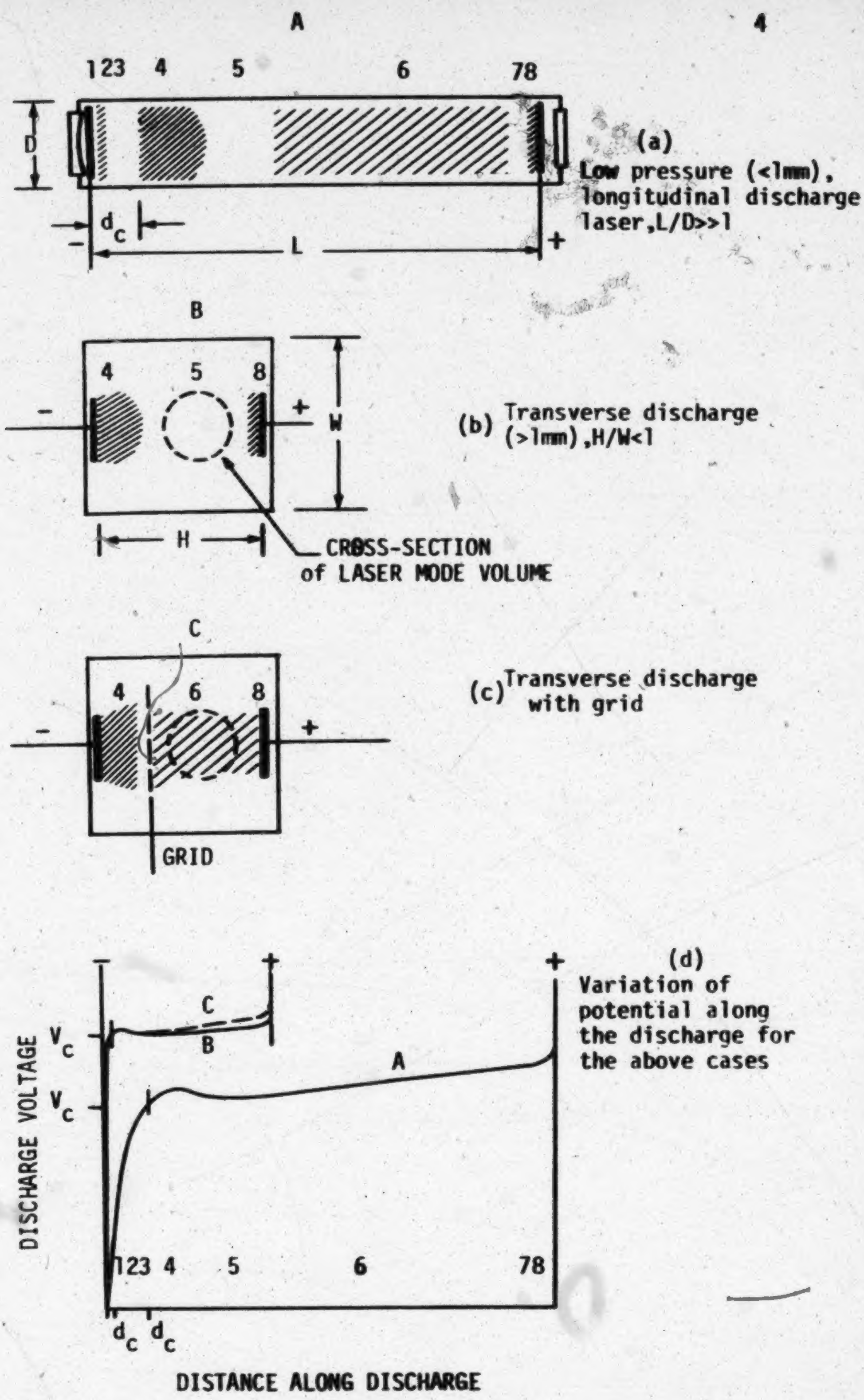
A
1 2 3 4 5 6 7 8
D
d_c
L
-
+
(a)
Low pressure (<1mm), longitudinal discharge laser, L/D>>1
B
4 5 8
-
+
W
H
CROSS-SECTION of LASER MODE VOLUME
(b) Transverse discharge (>1mm), H/W<1
C
4 6 8
-
+
GRID
(c) Transverse discharge with grid
(d)
Variation of potential along the discharge for the above cases
DISCHARGE VOLTAGE
V_c
V_c
C
B
A
1 2 3 4 5 6 7 8
d_c d_c
DISTANCE ALONG DISCHARGE

FIGURE 1.1. LONGITUDINAL AND TRANSVERSE GLOW DISCHARGES. The numbers refer to regions described in the text.

a certain minimum potential related to the Paschen minimum for the breakdown voltage. In other words, the distance d_c is such that the product of d_c and pressure, p, corresponds approximately to that for the Paschen minimum. From this consideration, then, the observed decrease of d_c (and cathode dark space) with pressure maintains the optimum value of pd_c.

For low discharge current, I_D, the negative glow does not completely cover the cathode. Raising I_D causes the glow to expand over the surface with a constant cathode drop potential (and current density) referred to as the "*normal*" cathode fall, V_n. A discharge operating in this regime likewise is termed a normal glow discharge. Once the glow has completely covered the cathode, however, further raising of I_D necessitates an increase in the potential drop to provide additional ionization. This positive resistance region is termed the "*abnormal*" glow. A negative resistance region is eventually reached where transition takes place from the abnormal glow to a highly contracted low voltage arc discharge. The ballast resistance determines to a large extent the operating regime but difficulties are encountered with glow to arc transitions as discussed in section 1.2.4.

The cathode fall, V_c, is an important parameter of the low pressure transverse discharge laser of Chapter 2. In this thesis transverse discharge refers to electrical excitation established across the smallest dimension of the laser cavity and thereby perpendicular to the laser axis. Schematic representations are illustrated in Figures 1(b) and (c). A large V_c (several hundred volts) produces an extended negative glow of low laser gain, undesirable gas heating and is responsible for low overall efficiency due to the considerable power dissipated in the cathode region. According to Cobine [13] the cathode drop, V_n, increases nearly linearly with the work function of the material. Francis, [12] however, states that "modern" values show no proportionality. That V_n does not show a simple relationship with work function, as Francis points out, may be expected since V_n is probably determined by the coefficient for secondary emission, γ, which depends both on the cathode material and the gas.

The negative glow is the region of most intense ionization within the discharge. The intense ionization is caused by electrons which enter the negative glow with several hundred eV corresponding to the cathode drop potential. The high energy electrons lose energy rapidly at the cathode edge of the negative glow, however, probe studies in the middle of the negative glow indicate the presence of three groups of electrons; primary (>25eV), secondary (4-7eV), and ultimate (≈0.5eV). Most studies have been of pure gas mixtures, such as helium [14] and neon [15], however, it is expected that a similar situation exists in the negative glow of the CO_2 laser mixture. Towards the Faraday dark space most of the electrons become slow (ultimate) but even in other regions of the glow there are many more slow electrons than fast. The role of the electron energies of the negative glow in connection with a grid inserted into the Faraday dark space is discussed in Chapter 2.

The fact that the secondary electrons appear to have an energy range for pumping the CO_2 laser prompted Willet and Janney [16] to investigate a hollow cathode discharge in CO_2. The device gave only low gain in a CO_2 - He mixture. The reason is unclear but probably was due in part to the gas heating associated with the relatively large power dissipated in the cathode regions. Freiberg and Clark [4] also observed that the negative glow and Faraday dark space produced low gains. That the Faraday dark space shows only low gain is expected since the lack of visible glow from this region indicates low electron energies. As the calculations of Nighan [17] show, electron pumping of the CO_2 laser is drastically reduced for an average electron energy less than 0.5eV. The current in the Faraday dark space is by diffusion from the concentration gradient in the negative glow with the electron current to the anode dominating. The transition from the Faraday dark space to the positive glow is controlled by charged particle diffusion losses to the walls. In other words, increased loss necessitates higher electron energies for a higher ionization rate and the positive column expands at the expense of the Faraday dark space.

1.2.2 *Positive Column*

When a discharge is struck within the confining walls of a long tube most of its length is filled with the positive glow or column. The positive glow represents the region of maximum pumping of the CO_2 laser mixture. A measure of the optimization of this "active" medium is obtained through the similarity parameter, E/N, the ratio of the electric field to the total neutral concentration. The reduced field, E/N, is directly related to the average energy of the electrons. In this regard Nighan [17] has performed calculations to show the variation of the average electron energy with E/N.

The value of E/N required to support the discharge is controlled by charged-particle loss from the plasma. For the case of a longitudinal discharge, E/N is controlled by ambipolar diffusion to the confining walls. Consequently, E/N shows an inverse relationship with tube diameter. This was experimentally confirmed by Tyte and Sage [18] for the CO_2 laser mixture. If the walls are made sufficiently remote a situation can arise where the high gain positive column is absent [13] and the Faraday dark space reaches to the anode as reported by Sedgwick and Seguin [5] for a transverse structure, Figure 1(b). In this case, a grid was found useful for creating a positive glow as illustrated in Figure 1(c).

When an electrical discharge is subjected to high velocity cross-flow, as in Chapter 3, additional loss mechanisms take place in the form of convection into the afterglow and turbulent diffusion to the walls. If a plasma is subjected to turbulent gas flow the charged-particles acquire the turbulent motions of the neutral particles. Turbulence can change both the microscopic and macroscopic properties of the plasma. For instance, changes are produced in the particle energies and densities while the overall plasma shape may be modified. Experiments performed by Garosi et al [19] with a longitudinal discharge in low pressure argon support the fact that ambipolar diffusion controls the loss for low flow velocities while for higher flow rates ambipolar losses are augmented by turbulent diffusion to the column boundary. The laser structures of Hill [9] and Eckbreth and Owen [20] employed flow conditioners upstream of a segmented electrode structure in rapid-flow longitudinal-discharge arrangements. The increased turbulence caused the plasma in the vicinity of the electrodes to diffuse more rapidly. As a result local thermal inhomogeneities were reduced thus permitting a higher stable power loading of the discharge.

Convection and turbulent diffusion were assumed to have considerable effect on the cross-flow discharge of Chapter 3. The decay of the flowing after-glow may also have been influenced by turbulent diffusion to the channel walls.

1.2.3 *Electrode effects*

(1) Glow to arc transitions

For the excitation of a large volume through a transversely applied field it is desirable to have continuous electrodes extending the full length of the structure. The formation of a uniform continuously operating, as opposed to a pulsed, discharge over large electrodes is not readily realizable in practice. This is true, particularly at the gas and current densities of the CO_2 laser. The break-down of the discharge into a highly contracted or more likely a highly destructive arc mode is greatly enhanced by localized gas heating. Heating causes a reduction in local gas density which the discharge then favours. The net result is the localization of the full discharge current which rapidly develops into an arc.

The cathode plays a dominant role in these glow to arc transitions. The cathode current density is roughly proportional to the square of the pressure, p, and the length of the cathode fall region is inversely proportional to p. As a result, the energy dissipated per unit volume in the vicinity of the cathode is proportional to p^3 [21]. To reduce the cathode dissipation an electrode material is desired that gives the least cathode drop when used with the CO_2 laser gas mixture. As pointed out earlier this does not necessarily mean the material of lowest work function since the important parameter is γ, the coefficient for secondary emission.

Cathode metals with low heats of sublimation exhibit a sudden transition from the glow to the arc. The suggestion is that localized increases in vapor density are accompanied by an increase in current density. This process is cumulative and results in an arc spot. If the metals are arranged according to their heats of sublimation the order is the same as when arranged according to the minimum current to produce arcing [22]. Mercury and cadmium are at the top of the list while tungsten and carbon are at the bottom.

Maskrey and Dugdale conducted experiments in which arcs were found to be initiated at the sites of insulation inclusions [23]. The presence of volatile contamination was found to be conducive, if not necessary, for initiation of this arcing. The contamination also caused a marked increase in the conditioning time of the electrode surface. The mechanism proposed for arc initiation is a burst of cathodic vapour as a result of dielectric breakdown of an insulation inclusion. There seems to be no difference in initiation if the particles of low conductivity are sitting on the surface. This suggests that metals that chemically react with the discharge to form highly resistive surface layers are likely to show a much higher tendency to arc, as found for Al in the CO_2 laser mixture [5].

(2) Surface chemistry

The surface chemistry of the electrodes has a strong influence on the gas composition, particularly, for sealed-off systems, flowing or non-flowing. As already mentioned Al appears to react fairly quickly to produce a highly insulating surface layer [5].

Molybdenum, nickel, and tantalum are more stable, giving higher reproducibility of laser characteristics in a sealed-off laser [24]. Copper shows a relatively rapid adsorption of CO_2. Platinum produces very little dissociation of CO_2. It is assumed that this is primarily due to the catalytic action of platinum in the oxidation of CO, [25]. Unfortunately, however, platinum has a high "sputtering" rate which makes its use as a cathode material impractical. In experiments with a sealed CO_2 laser using a Ni cathode, Carbone[26] observed a Ni film sputtered on the adjacent tube walls while a carbon deposit formed beneath the electrode. Oxygen reacted with the Ni film to produce NiO. Freudenthal [27] analyzed a deposit formed near a cathode of platinum. A complex mass spectrum was obtained in which it was discovered that both carbon and oxygen were diminished by the formation of the deposit.

(3) Cathode geometry

As mentioned previously in section 1.2.1, the negative glow represents a region of high gas heating and low laser gain. Consequently, a reduction or elimination of the negative glow from the laser cavity is desirable. Once the surface of a flat cathode is covered with negative glow any further increase in discharge current results in an increase in the cathode drop potential and a lengthening of the negative glow.

The hollow-cathode has desirable features [28]. First, most of the negative glow is confined to the interior of the tube with an increase in the useful discharge length and a reduction in gas heating. Secondly, by proper choice of hole diameter a higher current can be drawn over that of the flat cathode for the same cathode-drop potential. If it is desired to laterally extend the discharge several hollow-cathodes may be incorporated into a single surface producing an inverted brush electrode [29]. Here the proper choice of hole diameter is controlled by the minimum hole size that will still force the discharge over the complete electrode surface for the desired operating current. Holes of too small diameter will result, at worst, in a single hollow-cathode supplying the necessary discharge current with a subsequent reduction in discharge volume. An alternative is to provide an array of closely spaced individually ballasted hollow-cathodes of small diameter as used in the experiments presented in Chapter 3.

The previous paragraphs emphasize the role played by the cathode in cold cathode glow discharges. The anode presents less difficulty since the anode potential fall is the order of the least ionization potential of the gas mixture [30]. This is an order of magnitude less than the cathode fall. As a result the anode plays a much smaller role in gas heating and glow to arc transitions. In Chapter 2, the experiments were conducted with a single continuous strip anode.

1.3 Energy Transfer Processes

In the electric discharge CO_2 laser, energy is coupled from the electric field via the electron component of the plasma directly and indirectly to the upper laser level, (00^01) of the CO_2 asymmetric vibrational mode. The lower vibrational levels of the various constituents of an initial $CO_2/N_2/He$ mixture are illustrated in Figure 1.2. CO and O_2 appear by way of dissociation of CO_2 as discussed later in section 1.4. CO_2 molecular structure, spectroscopy, and transfer processes in the laser gas mixture are comprehensively reviewed by Cheo [31]. Reference is made to more recent experiments in the following paragraphs which discuss energy transfer processes and their

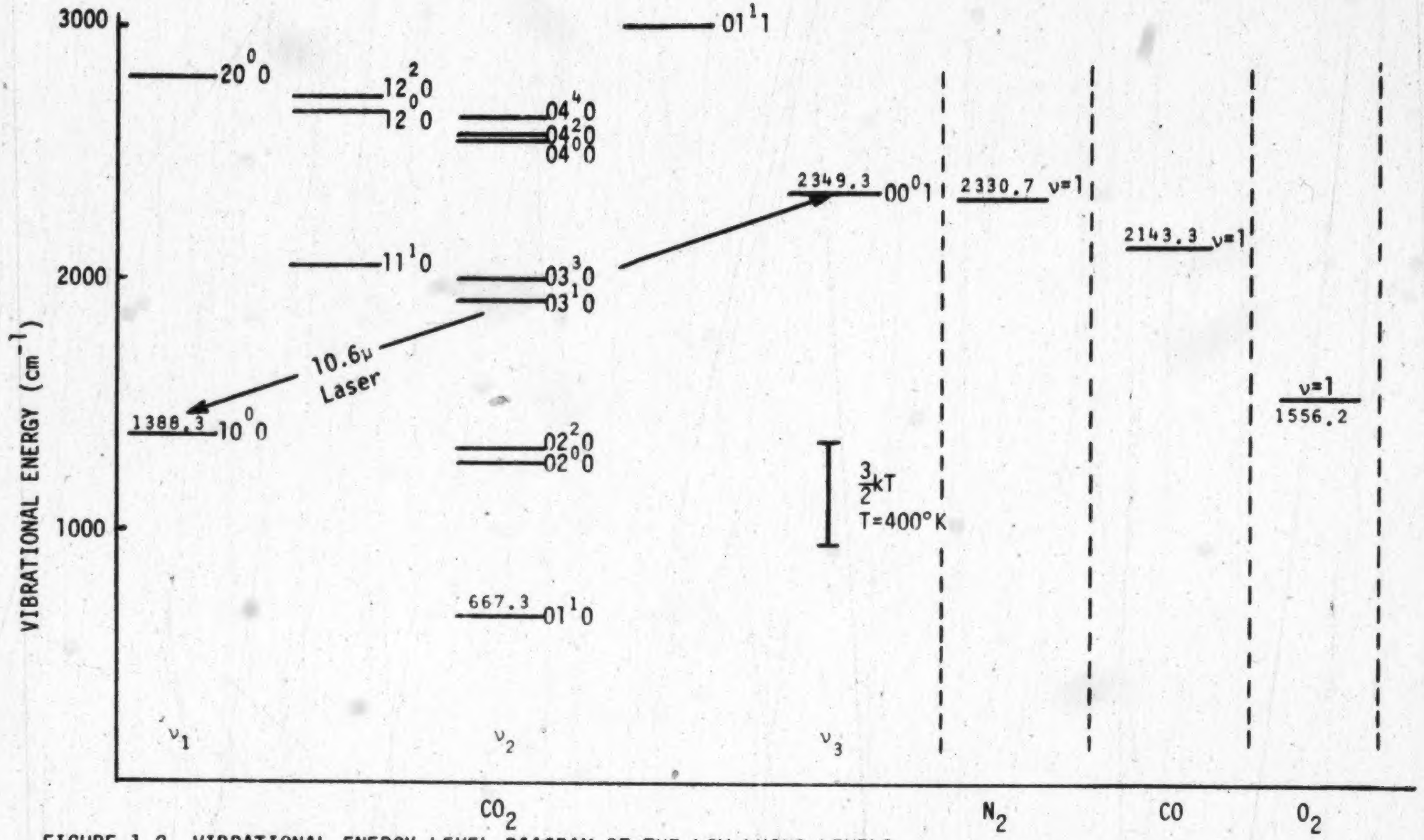
VIBRATIONAL ENERGY (cm^{-1})
3000
2000
1000
20^00
12^20
12^00
11^10
1388.3
10^00
10.6μ
Laser
04^40
04^20
04^00
03^30
03^10
02^20
02^00
667.3
01^10
01^11
2349.3
00^01
$\frac{3}{2}$kT
T=400°K
2330.7 ν=1
2143.3 ν=1
ν=1
1556.2
ν_1
ν_2
ν_3
CO_2
N_2
CO
O_2

FIGURE 1.2. VIBRATIONAL ENERGY LEVEL DIAGRAM OF THE LOW-LYING LEVELS OF CO_2, N_2, CO, AND O_2. The average energy of translation is shown for T = 400°K.

significance in establishing a population inversion between the (10^00) and (00^01) vibrational levels of CO_2. The stimulated emission process is discussed later in Chapter 3, section 3.2.

Excitation of the (00^01) level occurs both by inelastic collisions with electrons and energy transfer from vibrationally excited N_2 and CO. Deactivation of the (00^01) level occurs via spontaneous and stimulated emission, molecular collisions, and as recent experimental evidence suggests, collisions with electrons. The spontaneous lifetimes [32] of the involved levels are much longer than collisional time constants for the usual gas densities. Consequently population densities of the upper, (00^01), and lower, (10^00), laser levels are a strong function of collisional relaxation and the intra-cavity field intensity.

The rotational levels of each vibrational level have energies smaller than the average thermal energy of the molecules. The average thermal energy of a molecule at 400^0K, say, is approximately 417 cm^{-1} as opposed to a rotational quantum energy of approximately 45 cm^{-1}. Consequently, rapid exchange of translational and rotational energy occurs by collisions [33] and the rotational levels are assumed to have a Boltzmann distribution at the translational temperature.

1.3.1 *Vibrational - vibrational transfer*

A near resonance exists between levels within a given vibrational mode. This results in rapid equilibration of the levels within each mode through near-resonant energy transfer [34]. Provided that this rate is more rapid than excitation of the various levels and relaxation into other modes, the mode may be considered in equilibrium at some *vibrational* temperature. This assumption is basic to the thermodynamic model [35] used in the analysis of Chapter 3 where each mode is assumed to have a Boltzmann distribution.

Both N_2 and CO have large cross-sections for vibrational excitation through electron impact [36]. These vibrational levels are nearly resonant with levels within the CO_2 asymmetric mode. The resonance together with the long radiative lifetime of vibrationally excited homonuclear diatomics, leads to highly effective pumping of the (00^01) laser level. Intermolecular vibration-vibration transfer is exemplified by collisions of the following type:

$$CO_2(00^01) + N_2(\nu=0) \overset{k}{\rightleftharpoons} CO_2(00^00) + N_2(\nu=1) + 18cm^{-1}$$

$$CO_2(00^01) + CO(\nu=0) \rightleftharpoons CO_2(00^00) + CO(\nu=1) + 206cm^{-1}$$

$$N_2(\nu=1) + CO \rightleftharpoons N_2(\nu=0) + CO(\nu=1) + 188cm^{-1}$$

k=rate constant for the exothermic process.

Large rate constants for vibrational exchange have been measured for CO_2-N_2 ($k=1.9 \times 10^4$ sec^{-1} $torr^{-1}$) [37] and CO_2-CO ($k=8 \times 10^3$ sec^{-1} $torr^{-1}$), references [38] and [39], where k is the rate for the exothermic process. A slower rate has been measured for N_2-CO (k=325 sec^{-1} $torr^{-1}$), reference [40]. Due to the fast equilibration of CO_2 with N_2 and CO, the CO_2 asymmetric mode is considered in equilibrium with the vibrational levels of N_2 and CO for the analysis of Chapter 3 where cross-flow velocities less than 100 m/sec were investigated

In the absence of a radiation field the upper laser level is deactivated by intramolecular vibration-vibration processes. The following reactions are close to resonance:

$$CO_2(00^01) + M \rightleftharpoons CO_2(11^10) + M + 272\text{cm}^{-1}$$

$$CO_2(00^01) + M \rightleftharpoons CO_2(03^10) + 416\text{cm}^{-1}$$

$$CO_2(00^01) + M \rightleftharpoons CO_2(04^00) - 204\text{cm}^{-1}$$

M = collision partner.

Experimental data for the relaxation of CO_2 do not specify the final state. By using rare gases as collision partners with CO_2, Yardley and Moore [41] concluded that the probability of a relaxing collision is more likely when an energy of less than 300 cm^{-1} is exchanged with translations. Also processes to levels below the laser level are likely to dominate. In the analysis of Chapter 3 the first of the above reactions was considered as the dominant mechanism in the heavy-particle relaxation of the upper laser level. A discussion of the rates for this reaction is deferred to Chapter 3, section 3.2.

1.3.2 *Deactivation of the lower laser level*

The lower laser level, (00^01), and the (02^00) level of the bending mode are closely coupled due to Fermi-resonance [42]. Theoretical calculations by Herzfeld [43] for pure CO_2 give a fast rate of energy exchange between these levels.

$$CO_2(10^00,02^00)' + M \rightleftharpoons CO_2(10^00,02^00)'' + M + 102\text{cm}^{-1}$$

M = collision partner

The levels (10^00) and (02^00), each become a mixture of both levels due to Fermi resonance and are designated as $(10^00,02^00)'$ and $(10^00,02^00)''$, reference [42]. A rapid exchange due to Fermi-resonance of (00^01) and (02^00) is usually invoked to simplify laser models in that the symmetric stretch and bending modes are in equilibrium and describable by a single vibrational temperature. Rapid equilibration is assumed within the bending mode. As a result the relaxation of the lower bending level (01^10) to translation becomes the rate determining process for deactivation of the lower laser level.

$$CO_2(01^10) + M \rightleftharpoons CO_2(00^00) + M + 667\text{cm}^{-1}$$

M = collision partner

A summary of rates for the exothermic process are given by Taylor and Bitterman [44]. Pure CO_2 has a rate constant of 194 sec^{-1} torr^{-1} while the rate for a CO_2-He mixture is approximately 3.3×10^3 sec^{-1} torr^{-1} thus illustrating the effectiveness of He collisions for deactivating the (01^10) level. For CO_2-CO a rate constant of 2.5×10^4 sec^{-1} torr^{-1} is listed in reference [31] showing that CO is also a very effective collision partner.

Recent experiments by Rosser et al [68] have indicated that the (10^00) and (01^10) levels are not closely coupled contrary to the above assumptions. In pure CO_2 and mixtures of CO_2 and Xe the measured rate of relaxation of (10^00) is much faster than the accepted rate for (01^10). Additions of He to CO_2 produced only a small increase in the (10^00) rate while the accepted rate for (01^10) shows a large increase as stated above. Both N_2 and CO behaved similarly in greatly reducing the relaxation rate of (10^00). This appears to contradict the pulse-gain data of Cheo [45] which give an effective relaxation rate for the lower laser level. The measured rate constant for nitrogen was low, while that for CO was more than two orders of magnitude higher.

The experiments of reference [68] suggest that the (01^10) bending level may be close to equilibrium with the gas temperature during relaxation of the lower laser level and therefore the symmetric-stretch and bending modes cannot be described by the same vibrational temperature. No reaction mechanism was proposed by reference [68] however, as stated; if the (10^00) and (02^00) are tightly coupled by Fermi-resonance then relaxation of the lower laser level must be controlled by the rate to the (02^20) and (01^10) levels.

1.3.3 *Vibrational excitation and deactivation by electron impact*

Large cross-sections have been measured for vibrational excitation of CO_2, N_2, and CO [36] [46]. The cross-sections peak for electron energies in the range one to three eV. Due to the relatively large energy transfer, the electron energy distribution becomes quite non-Maxwellian. This is shown by the theoretical calculations of Nighan using experimental cross-sections [17]. Electrostatic probe measurements, such as those by Bletzinger and Garscadden, also illustrate the non-Maxwellian nature of the distribution [47]. Using computed distribution functions Nighan calculated "effective" vibrational excitation rates. The resulting rates are not a strong function of gas mixture or electron energy for average energies above approximately 0.5eV.

By calculating the electron fractional power transfer [17] into elastic collisions, rotational excitation, ionization, electronic excitation and vibrational excitation, laser efficiency may be investigated versus electron energy. The electron fractional power transfer was calculated by Bullis et al [48] for a $CO_2/N_2/He$ mixture in the proportions 0.1/0.1/0.8. Power transferred to elastic collisions, rotational excitation, and ionization is small. For a reduced average energy of 0.5eV ($E/N = 8 \times 10^{-17}$ volt cm^2) calculations show that nearly all the energy goes into the vibrational excitation of either CO_2 or N_2. The reduced average energy is defined as 2/3 of the average energy. As the electron energy is raised, electronic excitation becomes significant. At 3eV ($E/N = 6 \times 10^{-16}$ volt cm^2), for instance, approximately 80% of the electron energy is transferred to electronic excitation of CO_2 and N_2. As outlined in section 1.2.2 charged-particle losses from the plasma control the ionization rate required to support the discharge which in turn specifies a certain electron energy. The power transferred to ionization, however, is small, as noted above. Assuming that the required ionization rate is provided by a reduced average energy of leV, reference [48] shows that 70% of the electron energy is transferred to the upper laser level and the vibrational levels of N_2. Since the laser quantum efficiency is 41% a conversion of approximately 30% of the electrical energy to laser radiation is expected for this case. The above computations stress, therefore, that once the average energy has reached a certain threshold any further increase results in reduced efficiency as the fractional power transfer to electronic excitation rises.

Since electron energies are difficult to measure, particularly at pressures above a few millimeters, excitation rates used in this thesis were estimated by the following procedure. First the reduced field, E/N, was measured. The average electron energy was then estimated from reference [17]. Using this average electron energy, effective excitation rates were obtained, again, from the appropriate rate curves of reference [17].

The role of electrons in vibrational deactivation, or collisions of the second kind, has been experimentally investigated recently. The published results suggest that cool electrons are highly effective in vibrational relaxation. Christophe and Offenberger observed an electron rate of the same order as molecular processes [38]. Rosser et al also observed relaxation effects that may be attributed to electrons [68]. They suggest that if electrons contributed to vibrational relaxation in their experiments the probability for deactivation is near unity. Gower and Carswell estimate experimental rates of approximately 1 x 10^{-6} cm^3/sec and 3 x 10^{-6} cm^3/sec for electron deactivation of the upper and lower laser levels respectively, references [39] [49]. By comparison, the effective excitation rate of N_2, for instance, was calculated by reference [17] to be approximately 2 x 10^{-8} cm^3/sec. The results of reference [49] show further that the relaxation of the upper laser level is primarily by electrons.

The above experiments strongly suggest that any model of laser processes must include electron deactivation.

1.4 *The effects of discharge-induced gas composition changes*

The electrical discharge causes considerable chemical change in the CO_2 laser mixture [24] [26], [50] - [59]. One of the largest changes is the dissociation of CO_2. CO_2 dissociation has received considerable investigation but the role of the products, O_2 and CO, remains somewhat unclear. Some dissociation is beneficial, particularly, in the case of a CO_2-He mixture where CO pumps the upper laser level through resonant energy transfer [60] [61] [62]. In the CO_2-N_2-He mixture, however, increasing experimental evidence suggests that the dissociation product O_2 may combine with N_2 producing oxides which seriously degrade laser gain and discharge stability [58] [59]. The discharge characteristics appear to be altered through the formation of stable negative ions [57] [58].

The primary mechanism for CO_2 dissociation is assumed to be electron impact [24] [54]. The degree of dissociation is a function of many parameters including gas composition, total gas pressure, discharge current, average electron energy and gas flow or residence time in the discharge. For low pressures and low flow rates the dissociation fraction, δ, ($\delta = N_{CO}/N_{CO}+N_{CO_2}$ where N is the species number density), can reach as high as 0.7 to 0.8 [51] [52]. For open cycle flow, residence times of the order of one second are required for dissociation equilibrium to be established. For faster flow rates the CO concentration shows an almost linear increase with tube length [54]. The variation of CO concentration is reflected in a change of colour along the discharge length, from pink at the entrance to bluish pink at the exit.

For closed cycle flow, the equilibration time is likewise dependent on the discharge residence time. For a high cross-flow velocity and a short discharge width, gas dwell times are low. As a result, although the chemical state remains "frozen" after passage through the glow, many circulations may be required for equilibration. For the conditions of Chapter 3, times of the order of one minute were typical.

The degree of dissociation is also a function of the constituents and the total gas pressure. Higher gas pressure reduces the CO concentration [52]. This may be related to changes of average electron energy and the processes of adsorption and desorption to and from the walls and electrodes [24] [51]. The greatest dissociation occurs in a CO_2-N_2 mixture and the least in CO_2-He. The triple mixture CO_2-N_2-He shows greater dissociation than CO_2-He [51]. The addition of small quantities of H_2O or H_2 significantly reduces the degree of dissociation [50] [51]. The presence of H_2 also leads to an increase of output power due to its large thermal conductivity and the relaxation of the (01^10) level of the CO_2 bending mode by H_2O molecules formed in the discharge containing H_2.

The average electron energy appears to play a dominant role in the extent of dissociation. The study by Gasilevich et al on the CO_2 concentration in tubes of various diameters found a much greater degree as the tube diameter decreased [51]. This was assumed to be due to the higher average electron energy required to support a discharge in smaller tubes. For a tube of constant diameter, the dissociation equilibrium rises with discharge current.

Nighan's calculations [63] show that increasing CO content in a CO_2-N_2-He mixture accentuates the decrease in the electron distribution function for energies above 2eV as a result of the large vibrational excitation cross-section of CO [36]. For typical laser conditions with 50% dissociation, a calculated 15% of the electron energy is transferred to the CO vibrational levels. Also, as the dissociation increases calculations show a beneficial decline of the electron energy transferred to the coupled symmetric-bending modes of

CO_2 [17].

The electron power transfer to O_2 is small. For typical laser conditions the inelastic collision rate with O_2 is much less than with either CO or CO_2 [64]. Consequently, the vibrational excitation of O_2 due to electron impact appears to be small. O_2 may play a more significant role in the production of new species such as the oxides of nitrogen which greatly affect the discharge kinetics [58] [59]. Reaction of O_2 with the metal electrodes in a sealed-off system may promote further dissociation of CO_2 and consequently limit the laser lifetime [26].

Buser and Sullivan [53] used Le Chatelier's principle to test the reversibility of the dissociation reaction. After equilibration and while operating the discharge, the CO_2 was frozen out at the discharge walls by a liquid nitrogen bath. After the discharge stopped running the system was returned to room temperature and analysis showed that the CO_2 composition had returned to its initial value.

As stated previously, CO added to or by way of dissociation in a CO_2-He mixture enhances the pumping of the CO_2 (00^01) upper laser level through resonant energy transfer. With N_2 added to the mixture the role of CO is diminished. The calculations of Lotkova et al [24] showed that approximately 10% dissociation in an initial CO_2-N_2-He mixture was beneficial through resonant energy transfer. Further dissociation degraded the population inversion due to the decreasing CO_2 concentration and an increased collisional-relaxation rate of the upper level by CO. The computation appears to employ the following reaction for relaxation of vibrationally excited CO to the symmetric-bending modes of CO_2 [65]:

$$CO(\nu=1) + CO_2(00^00) \rightarrow CO(\nu=0) + CO_2(11^10) + 66cm^{-1}$$

A high probability was calculated for this reaction in reference [66]. Experimental measurements by Rosser et al [67], however, show that the rate of the above reaction is small.

Experimentally, the effects of discharge produced species have been investigated by adding the various contaminants to a flowing CO_2 laser mixture and monitoring laser gain and discharge characteristics [58] [60] [61]. The flow rates of added CO or O_2 were the order of the CO_2 flow rate before laser gain was reduced to zero. Since CO increases the discharge impedance some of the gain reduction can be attributed to increased gas heating due to higher power loading of the discharge. O_2 reduces the discharge impedance contrary to the behavior expected from its electro-negative character. It has been suggested in reference [58] that the impedance reduction may be due to efficient cumulative ionization of oxygen. Bletzinger et al found that only small amounts of the nitrogen oxides increased the discharge impedance and reduced the gain [58]. For the gas pressures used (total pressures of 5, 10, and 15mm), additions of NO, N_2O, and NO_2 of approximately 1% of the total flow rate were sufficient to cause complete loss of gain and an unstable constricted positive column. In an associated study [59], discharge generated NO and NO_2 were detected in sufficient quantities to affect laser performance.

The discharge chemistry of the CO_2 laser is understandably complex. Many studies have concentrated on constituent changes with the aim of extending the lifetime of sealed-off tubes. With the advent of electric discharge convection lasers considerable investigation has been directed toward discharge generated species, particularly to find an explanation for the reduced stable power loading observed when convection systems are switched from open to closed-cycle flow [9].

1.5 Scope of the Thesis

The preceding discussion was intended to put the topic of this thesis into perspective as far as the excitation of CO_2 lasers is concerned. The significant physical regions occurring within the glow discharge were discussed. The requirements of the average energy of the electron excitation were outlined as well as the important collisional relaxation processes. Discharge chemistry was discussed with respect to gas composition changes and electrode surface effects. Reasons for the troublesome problem of glow to arc transitions were outlined.

In Chapter 2, investigations of the laser gain and power of transverse electrical excitation with a triple electrode system, using a wire-mesh grid, will be outlined. Data showing the effectiveness of the grid in raising the average energy of the electrons in a slow-flow system will be presented.

In Chapter 3, experiments on laser performance with transverse excitation in a high-velocity cross-flow will be outlined. These include the interaction of the glow-discharge with the flow as well as the improvement of volumetric efficiency effected by convection of heat from the laser region.

A summary of results and conclusions as well as suggestions for future research will be presented in Chapter 4.

REFERENCES

1. C.K.N. Patel, "Interpretation of CO_2 Optical Maser Experiments", Phys. Rev. Letters, Vol. 12, No. 21, p. 588, May 1964.

2. J.D. Rigden and G. Moeller, "Recent Developments in CO_2 Lasers", IEEE J. Quantum Electronics, Vol. QE-2, No. 9, p. 365, September 1966.

3. T.G. Roberts, G.J. Hutcheson, J.J. Ehrlich, W.L. Hales, and T.A. Barr, Jr., "High-Power N_2-CO_2-He Laser Development", IEEE J. Quantum Electronics, Vol. QE-3, No. 11, p. 605, November 1967.

4. R.J. Freiberg and P.O. Clark, "CO_2 Transverse-Discharge Lasers", IEEE J. Quantum Electronics, Vol. QE-6, No. 2, p. 105, February 1970.

5. G. Sedgwick and H. Seguin, "Low Voltage CO_2 Laser Excitation", J. Appl. Optics, Vol. 9, No. 12, p. 2737, December 1970.

6. W.B. Tiffany, R. Targ, and J.D. Foster, "Kilowatt CO_2 Gas-Transport Laser", Appl. Phys. Lett., Vol. 15, No. 3, p. 91, August 1969.

7. C.J. Buczek, R.J. Wayne, P. Chenausky, and R.J. Freiberg, "Magnetically Stabilized Cross-Field CO_2 Laser", Appl. Phys. Lett., Vol. 16, No. 8, p. 321, April 1970.

8. C.O. Brown, "High-Power CO_2 Electric Discharge Mixing Laser", Appl. Phys. Lett., Vol. 17, No. 9, p. 388, November 1970.

9. A.E. Hill, "Uniform Electrical Excitation of Large-Volume High-Pressure Near-Sonic CO_2-N_2-He Flowstream", Appl. Phys. Lett., Vol. 18, No. 5, P. 194, March 1971.

10. H.J. Seguin and G. Sedgwick, "Low Voltage Gas Transport TE CO_2 Laser", Vol. 11, No. 4, p. 745, April 1972.

11. A. von Engel, "Ionized Gases", Oxford University Press, London, 1965.

12. G. Francis, "The Glow Discharge at Low Pressure", Handbuch der Physik, Vol. XXll, edited by S. Flugge (Springer-Verlag, 1956), p. 56.

13. J.D. Cobine, "Gaseous Conductors", Dover Publications, New York, 1958.

14. D.H. Pringle and W.E.J. Farvis, "Electron Groups in the Helium Negative Glow", Phys. Rev., Vol. 96, No. 2 p. 536, October 1954.

15. M.J. Vasile and R.F. Pottie, "The Collection of Positive Ions and Electrons by a Screened Probe in the Neon Negative Glow", Advances in Chemistry Series, No. 80(1969) p. 92.

16. C.S. Willet and G.M. Janney, "Amplification at 10.6μ in the Negative Glow of a Hollow-Cathode Discharge in a CO_2-He Mixture", IEEE J. Quantum Electronics, QE-6, No. 9, p. 568, September 1970.

17. W.L. Nighan, "Electron Energy Distributions and Collision Rates in Electrically Excited N_2, CO, and CO_2", Phys. Rev. A, Vol. 2, No. 5, p. 1989, November 1970.

18. D.C. Tyte and R.W. Sage, "Electron Temperature Measurements in CO_2 Laser Plasmas", Proceedings of IERE Conference on Lasers and Opto-Electronics, IERE Conf. Proc., No. 14, p. 238, 1969.

19. G.A. Garosi, G. Bekefi, and M. Schulz, "Response of a Weakly Ionized Plasma to Turbulent Gas Flow", Phys. Fluids, Vol. 13, No. 11, p. 2795, November 1970.

20. A.C. Eckbreth and F.S. Owen, "Flow Conditioning in Electric Discharge Convection Lasers", Rev. Sci. Instr., Vol. 43, No. 7, p. 995, July 1972.

21. Reference 13, p. 250.

22. Reference 13, p. 314.

23. J.T. Maskrey and R.A. Dugdale, "The Role of Inclusions and Surface Contamination in Arc Initiation at Low Pressures", J. Appl. Phys., Vol. 17, No. 8, p. 1025, August 1966.

24. E.N. Lotkova, V.N. Ochkin, and N.N. Sobolev, "Dissociation of Carbon Dioxide and Inversion in CO_2 Laser", IEEE J. Quantum Electronics, Vol. QE-7, No. 8, p. 396, August 1971.

25. F.M. Taylor, A. Lombardo, and W.C. Eppers, "Effect of a Heated Platinum Wire on a Sealed CO_2 Laser System", Appl. Phys. Lett., Vol. 11, No. 6, p. 180, September 1967.

26. R.J. Carbone, "Long-Term Operation of a Sealed CO_2 Laser", IEEE J. Quantum Electronics, Vol. QE-3, No. 9, September 1967.

27. J. Freudenthal, "Deposits in a Sealed-Off CO_2 Laser-Type Discharge", IEEE J. Quantum Electronics, Vol. QE-6, No. 8, p. 507, August 1970.

28. Reference 11, p. 236.

29. H.M. Musal, "An Inverse Brush Cathode for the Negative-Glow Plasma Source". J. Appl. Phys., Vol. 37, No. 4, p. 1935, March 1966.

30. Reference 12, p. 145.

31. P.K. Cheo, "CO_2 Lasers", Lasers, Vol. 3, edited by A.K. Levine and A.J. De Maria (Marcel Dekker, 1971), p. 111.

32. Reference 31, p. 132.

33. Reference 31, p. 163.

34. L.O. Hocker, M.A. Kovacs, C.K. Rhodes, G.W. Flynn, and A. Javan, "Vibrational Relaxation Measurements in CO_2 Using an Induced-Fluorescence Technique," Phys. Rev. Lett; Vol. 17, No. 5, p. 233, August 1966.

35. B.F. Gordietz, N.N. Sobolev, V.V. Sokovikov, and L.A. Shelepin, "Vibrational Level Inversion Population of Polyatomic Molecules, CO_2 Laser", Phys. Lett., Vol. 25A, No. 2, p. 173, July 1967.

36. G.J. Schulz, "Vibrational Excitation of N_2, CO, and H_2 by Electron Impact", Phys. Rev., Vol. 135, No. 4A, p. A988, August 1964.

37. C.B. Moore, R.E. Wood, B-L. Hu, and J.T. Yardley, "Vibrational Energy Transfer in CO_2 Lasers", J. Chem. Phys., Vol. 46, No. 11, p. 4222, June 1967.

38. B.M. Christophe and A.A. Offenberger, "Excitation and Relaxation of the Upper Laser State in a CO_2 Discharge", Can. J. Phys., Vol. 50, No. 4, p. 368, February 1972.

39. M.C. Gower and A.I. Carswell, "Vibration-Vibration Energy Transfer in CO_2 Glow Discharges", Appl. Phys. Lett., Vol. 21, No. 11, p. 556, December 1972.

40. W.H. Green and J.K. Hancock, "Laser-Excited Vibrational Energy Transfer Studies of HF, CO, and NO", IEEE J. Quantum Electronics, Vol. QE-9, No. 1, p. 50, January 1973.

41. J.T. Yardley and C.B. Moore, "Intramolecular Vibration-to-Vibration Energy Transfer in Carbon Dioxide", J. Chem. Phys., Vol. 46, No. 11, p. 4491, June 1967.

42. Reference 31, p. 123.

43. K.F. Herzfeld, "Deactivation of Vibrations by Collision in the Presence of Fermi Resonance", J. Chem. Phys., Vol. 47, No. 2, p. 743, July 1967.

44. R.L. Taylor and S. Bitterman, "Survey of Vibrational Relaxation Data for Processes Important in the CO_2-N_2 Laser System", Rev. Mod. Phys., Vol. 41, No. 1 p. 26, January 1969.

45. Reference 31, p. 161.

46. M.J.W. Boness and G.J. Schulz, "Vibrational Excitation of CO_2 by Electron Impact", Phys. Rev. Lett., Vol. 21, No. 15, p. 1031, October 1968.

47. P. Bletzinger and A. Garscadden, "The CO_2 Laser Plasma", IEEE Proc., Vol. 59, No. 4, p. 675, April 1971.

48. R.H. Bullis, W.L. Nighan, M.C. Fowler, and W.J. Wiegand, "Physics of CO_2 Electric Discharge Lasers", AIAA Journal, Vol. 10, No. 4, p. 407, April 1972.

49. M.C. Gower and A.I. Carswell, "Vibration-Translation Rates in CO_2 Glow Discharges", Appl. Phys. Lett., Vol. 22, No. 7, p. 321, April 1973.

50. W.J. Witteman and H.W. Werner, "The Effect of Water Vapor and Hydrogen on the Gas Composition of a Sealed-Off CO_2 Laser", Phys. Lett., Vol. 26A, No. 10, p. 454, April 1968.

51. E.S. Gasilevich, V.A. Ivanov, E.N. Lotkova, V.N. Ochkin, N.N. Sobolev, and N. G. Yaroslavskii, "Carbon Dioxide Dissociation in a CO_2 Laser", Soviet Physics-Technical Phys., Vol. 14, No. 1, p. 86, July 1969.

52. A.L.S. Smith, "Molecular Composition Changes in a Flowing CO_2-N_2-He-H_2O Laser", Brit. J. Appl. Phys. (J.Phys.D), Vol. 2, p. 1129, August 1969.

53. R.G. Buser and J.J. Sullivan, "Initial Processes in CO_2 Glow Discharges", J. Appl. Phys., Vol. 41, No. 2, p. 472, February 1970.

54. W.J. Wiegand, M.C. Fowler, and J.A. Benda, "Carbon Monoxide Formation in CO_2 Lasers", Appl. Phys., Lett., Vol. 16, No. 6, p. 237, March 1970.

55. N. Karube and E. Yamaka, "Mass-Spectrometric Studies of a Sealed CO_2 Laser", J. Appl. Phys., Vol. 41, No. 6, p. 2031, May 1970.

56. J. Freudenthal, "Collision Processes in a CO_2 Laser Plasma", J. Appl. Phys., Vol. 41, No. 6, p. 2447, May 1970.

57. W. J. Wiegand, "The Influence of Plasma-Generated Impurities on Molecular Gas Discharges", Bull. Amer. Phys. Soc. Vol. 17, No. 3, p. 398 (1972).

58. P. Bletzinger, M. Hughes, P.D. Tannen, and A. Garscadden, "Influence of Contaminants on the CO_2 Laser", Bull. Amer. Phys. Soc., Vol. 17, No. 3, p. 398 (1972)

P. Bletzinger, D.A. La Borde, W.F. Bailey, W. H. Long, P.D. Tannen, and A. Garscadden, "Influence of Contaminants on the CO_2 Electric Discharge Laser", submitted to IEEE J. Quantum Electronics, obtained by private communication.

59a. P.D. Tannen, P. Bletzinger, and A. Garscadden, "Species Composition in a CO_2 Laser Discharge", Third Conf. on Chemical and Molecular Lasers, St. Louis, Missouri, May 1972 paper MC-6.

59b. P.D. Tannen, P. Bletzinger, and A. Garscadden, "Species Composition in the CO_2 Discharge Laser", submitted to IEEE J. Quantum Electronics, obtained by private communication.

60. T.F. Deutsch, "Gain and Fluorescence Characteristics of Flowing CO_2 Laser Systems", IEEE J. Quantum Electronics, Vol. QE-3, No. 4, p. 151, April 1967.

61. P.K. Cheo, "Effects of Gas Flow on Gain of 10.6 Micron CO_2 Laser Amplifiers", IEEE J. Quantum Electronics, Vol. QE-3, No. 12, p. 683, December 1967.

62. H. Brinkschulte, "The Influence of CO on CO_2 Laser Performance", IEEE J. Quantum Electronics, Vol. QE-4, No. 11, p. 948, November 1968.

63. W.L. Nighan, "Effect of Molecular Dissociation and Vibrational Excitation on Electron Energy Transfer in CO_2 Laser Plasmas", Appl. Phys., Lett., Vol. 15, No. 11, p. 355, December 1969.

64. R.D. Hake and A.V. Phelps, "Momentum-Transfer and Inelastic-Collision Cross Sections for Electrons in O_2, CO, and CO_2", Phys. Rev., Vol. 158, No. 1, p. 70, June 1967.

65. E.N. Lotkova, V.N. Ochkin, and N.N. Sobolev, "Plasma Composition and Population Inversion in a CO_2 Laser", Soviet Phys.-Technical Phys., Vol. 15, No. 7, p. 1085, January 1971.

66. B.F. Gordietz, N.N. Sobolev, V.V. Sokovikov, and L.A. Shelepin, "Population Inversion of the Vibrational Levels in CO_2 Lasers", J. Quantum Electronics, Vol. QE-4, No. 11, p. 796, November 1968.

67. W.A. Rosser, R.D.Sharma, and E.T. Gerry, "Deactivation of Vibrationally Excited Carbon Dioxide (001) by Collisions with Carbon Monoxide", J. Chem. Phys., Vol. 54, No. 3, p. 1196, February 1971.

68. W.A. Rosser, E. Hoag, and E.T. Gerry, "Relaxation of Excess Populations in the Lower Laser Level CO_2(100)", J. Chem. Phys., Vol. 57, No. 10, p.4153, November 1972.

CHAPTER 2

TRANSVERSE EXCITATION WITH AXIAL GAS FLOW

2.1 Introduction

Transverse cold-cathode excitation of a low-flow CO_2-N_2-He laser is described as a means of reducing the high running potentials of a long cylindrical discharge. The geometry is shown in section 2.3, Figure 2.1, consisting of a triple electrode arrangement; a segmented cold-cathode, individual wire-mesh grids and a continuous anode with gas flow along the laser axis. Excitation was established across the smallest dimension of a box laser, with the view that the active medium could be extended laterally without significant changes in discharge potential. Ideally large area electrodes are desired with uniform excitation along the full length of the laser. Experiments showed, however, that the large cathode fall potential and localized gas heating caused the discharge to degenerate into highly contracted arcs. Consequently, a segmented cathode structure was used with a continuous strip anode. Considerable experimentation was conducted into the behavior of the grid as a means of generating uniform positive columns to raise the output power.

A transverse structure with a grid and thermionically emitting cathode was used by Tien [1] and Herceg and Miley [2] for excitation of a He-Ne laser. The structure consisted of continuous large area electrodes with a uniform diffuse glow established between the grid and anode. Freiberg and Clark [3] reported on experiments with a transversely excited CO_2-N_2-He laser in which both the anode and cold-cathode were segmented. Because of the close wall spacing the formation of positive columns was still necessitated by wall diffusion losses. Individual discharges of length 10 cm were formed between walls separated by 1.27 cm. Using 25 anode-cathode pairs of 2.5 cm separation and a 7 folded path resonator an output power of 20W was produced at 750V and 1A discharge current.

By comparison the structure described in this chapter employed excitation across the smallest dimension of the box; anode to cathode separation 2.9 cm as compared to a side wall separation of 8 cm. Grids were installed forming stable positive columns and thereby raising the output power by at least a factor of two. As reported by Sedgwick and Seguin [4] a multimode single path output power of 3W was obtained at 550V and 1A discharge current. This was for a continuous anode and 8 cathode segments separated by 3.8 cm between centers. The continuous anode simplified construction and tended to make the discharge more continuous axially in the anode region. The cathode separation of 3.8 cm, as compared to an anode to cathode distance of 2.9 cm, suggested that considerably closer spacing could be employed before adjacent column interaction produced instability. This was in fact demonstrated later in Chapter 3. It may also be noted that due to limitations of the output coupling aperture, the mode diameter was approximately one-half the excited column height.

The following sections begin with the description of a plasma-grid interaction model. Subsequent sections experimentally investigate the triple-electrode excitation arrangement.

2.2 Glow Discharge Model with Grid

From experimental observations a grid exercised its greatest control over the discharge when the space charge sheaths around the wires were overlapping. A thick sheath produced a uniform anode-grid glow which spread evenly over the grid detached from it by the sheath. The V-I characteristic of such a grid was assumed to be similar to that of a plane Langmuir probe. On this basis formulas of the collisionless theory for a plane probe were used to predict grid behavior [5] [6] [7]. The two most interesting cases were,

(1) an isolated grid at floating potential

(2) a grid more negatively biased than floating potential.

From Chapter 1 it was outlined that the Faraday dark space is a region where the current is primarily by diffusion of the high ionization concentration of the negative glow. Also, the length of the dark space is controlled to a large degree by diffusion losses to the walls. The walls were remote for the transverse discharge laser permitting the Faraday dark space to occupy most of the active medium, of a simple anode-cathode combination. By inserting a wire grid into the Faraday dark space this region was replaced for certain conditions by a uniform positive glow of higher laser gain.

The following paragraphs contain a largely qualitative analysis based on the following assumptions:

(a) the grid acted as a potential barrier to the high concentration of thermal or ultimate electrons of the negative glow thus attenuating the diffusion current to such an extent that additional ionization was required in the grid-anode space.

(b) average electron energy in the grid-anode space was controlled by ambipolar diffusion to the grid and walls and recombination at the edges of the glow.

In view of the importance of sheath development the thickness is first considered. The ion current to the grid is space-charge limited according to the Child-Langmuir equation,

$$j_i = \frac{4\varepsilon_o}{9}\left(\frac{2e}{m_i}\right)^{1/2} \frac{V_G{}^{3/2}}{d^2} \qquad \text{A/m}^2 \qquad \ldots (2.1)$$

ε_o = permittivity of free space

e = electronic charge

m_i = ionic mass

V_G = grid to plasma potential

d = sheath thickness

$$j_i = en_i\left(\frac{kT_i}{2\pi m}\right)^{1/2} \qquad \ldots (2.2)$$

= ion-current/unit area to the grid

= random ion current density in the plasma

n_i = ion number density

T_i = ion temperature

Equating expressions (2.1) and (2.2) shows that d is proportional to $(1/n_i)^{1/2}$. For the conditions

$n_i = n_e = n = 10^{10}/\mathrm{cm}^3$ $\quad$ $m_i = 7 \times 10^{-23}$ gm.

$T_i = 400^{\circ}\mathrm{k}$ $\quad$ $V_G = 10\mathrm{V}$

the calculated sheath thickness was approximately 1.5 mm. Since n_i is proportional to the discharge current, I_D, the sheath thickness varies inversely with I_D. From probe studies, the negative glow ionization density greatly exceeds that of the Faraday dark space [8]. Consequently, the sheath thickness is expected to vary with both the discharge current and the grid position. The large ionization density of the negative glow and the necessary electron diffusion towards the grid are expected to reduce the sheath thickness on the cathode side. This, in fact was observed experimentally.

The sheath thickness is also a function of the electron temperature. For an isolated grid the electron and ion current densities are equal; the ion current is space-charge limited while the electron current is the diffusion of the high energy tail of the electron distribution.

$$j_i = en_i \left(\frac{kT_i}{2\pi m_i}\right)^{1/2}$$

$$j_e = en_e \left(\frac{kT_e}{2\pi m_e}\right)^{1/2} \exp\left(-\frac{V_G e}{kT_e}\right) \qquad \ldots (2.3)$$

The floating potential is therefore given by

$$V_F = \frac{kT_e}{2e} \ \ell n \left(\frac{T_e m_i}{T_i m_e}\right) \qquad . . . (2.4)$$

By comparing equations (2.1) and (2.4), the sheath thickness is roughly proportional to the electron temperature for a constant discharge current.

Next, the electron diffusion current through the grid is considered. The random electron current density, j_{ec}, at the cathode side of the sheath edge is given by

$$j_{ec} = en_{ec} \left(\frac{kT_e}{2\pi m_e}\right)^{1/2} \qquad . . . (2.5)$$

The electrons that pass through the grid do so against a retarding potential, V_G. The current density through the grid is then given by

$$j_e = \zeta en_{ec}\left(\frac{kT_e}{2\pi m_e}\right)^{1/2} \exp\left(-\frac{eV_G}{kT_e}\right) \qquad . . . (2.6)$$

ζ = geometric factor related to the grid open area

Equation (2.6) suggests that a maximum grid to plasma potential of only a few volts may be allowed before ionization occurs through the grid openings. In other words, if the diffusion current is attenuated past a certain critical value ionization occurs through the grid to support the given discharge current . This was consistent with experimental observation. For a certain negative bias the discharge became constricted in the grid region with intense ionization projecting through one or more of the grid openings.

The previous paragraphs outlined the behavior of the grid in reducing the diffusion-dominated low-energy electron current of the Faraday dark space. Now a short discussion is presented on the possible mechanisms controlling the average electron energy of the anode-grid volume. In the anode-grid volume, the "*active*" medium, an average electron energy greater than 0.5 eV is required to optimize the vibrational excitation [9]. The energy gained by the electrons from the electric field is balanced by various losses. For a steady-state discharge the ionization rate is equal to the rate of charged-particle loss, for instance, through ambipolar diffusion and recombination. As the charged-particle loss increases so must the electron energy to increase the ionization rate. As the electron energy is raised towards 0.5eV the energy coupled into vibrations rises rapidly and depresses the high energy tail of the electron distribution. This inelastic process causes the distribution function to become non-Maxwellian [9]. Since the ionization rate is determined by the high energy electrons higher values of E/N are required to maintain a given discharge current in the presence of inelastic losses.

In conventional low pressure tube discharges wall diffusion plays a dominant role in electron energy and produces the well known Bessel-function density profile [10]. For an unconfined transverse discharge, however, wall diffusion becomes less significant. The latter case probably corresponds more to that of a higher pressure tube where the discharge has contracted away from the walls. Although ambipolar diffusion to the side-walls was small, diffusion to the plates in which the electrodes were mounted was expected to be somewhat greater. It was assumed that recombination played a significant role at the column boundary particularly as the pressure was increased. Cross-sections for dissociative recombination are large. For instance, the rate for CO_2^+ has been measured as 3.8×10^{-7} cm^3/sec at room temperature [11]. It was further assumed that the grid served as the major control on the diffusion loss from the active medium. The current loss to the grid sheath from the active medium is given by equations (2.3). For distances greater than the sheath thickness, flow to the grid is diffusion controlled. By varying the grid to plasma potential, the intensity of the visible glow showed a marked variation, indicating a similar effect on the average electron energy. Since the energy loss to vibrational excitation increases rapidly for energies near 0.5eV only small changes in grid potential were expected to produce relatively large changes in E/N. This was reflected in a rise of the anode-grid potential. Variation of the grid bias potential, as regards charged-particle loss from the active medium, appeared to be analogous to variation of the tube diameter in a conventional discharge.

In principle plasma balance equations can be set up for the steady-state discharge, however, the solution even for the low pressure tube is rather complex [12] [13]. For the transverse discharge of this chapter, the solution is further complicated by the electrode geometry and the fact that the positive column is unconfined. Since significant gas heating occurs at the discharge core for useful input power densities, a heat flow equation must be solved simultaneously with the plasma balance equations.

In summary, a grid inserted into the Faraday dark space of a short unconfined discharge, attenuated the low-energy current of the dark space for grid bias more negative than space potential.

The intensity of the resulting positive glow was also a function of grid to space potential primarily through ambipolar current loss from the plasma. To provide a glow uniformly distributed across the grid a thick isolating space-charge sheath was necessary. From the above model it was shown that the sheath thickness is a function of electron energy and density. Since useful average electron energies are in the range 0.5 to 1.5eV, grid bias potentials of only a few volts were permitted. Attenuation of the high energy tail of the electron distribution produced visible ionization through the grid resulting in a constricted positive glow.

2.3 Experimental System

A diagram of the experimental laser is shown in Figure 2.1(a), along with dimensions of the various components. Figure 2.1(b) shows a photograph of the assembled laser.

The aluminum anode plate and the glass (or perspex) cathode plate were readily detachable for ease of electrode testing and grid to cathode adjustments. Glass side-walls permitted visual observation of the discharge. All electrodes were cooled by tap water. Each grid was coupled externally for the fixed bias and self-bias curves of section 2.4. Further details on grid sizes and cathode materials are contained in section 2.4. The anode was consistently a single water-cooled copper channel of 38 cm length. The width of 1 cm was chosen for uniformity of anode glow.

The electrical discharge was powered by a filtered D.C. supply. Each cathode was individually ballasted with approximately 500Ω per electrode for self-biased grids and 2KΩ for isolated grids.

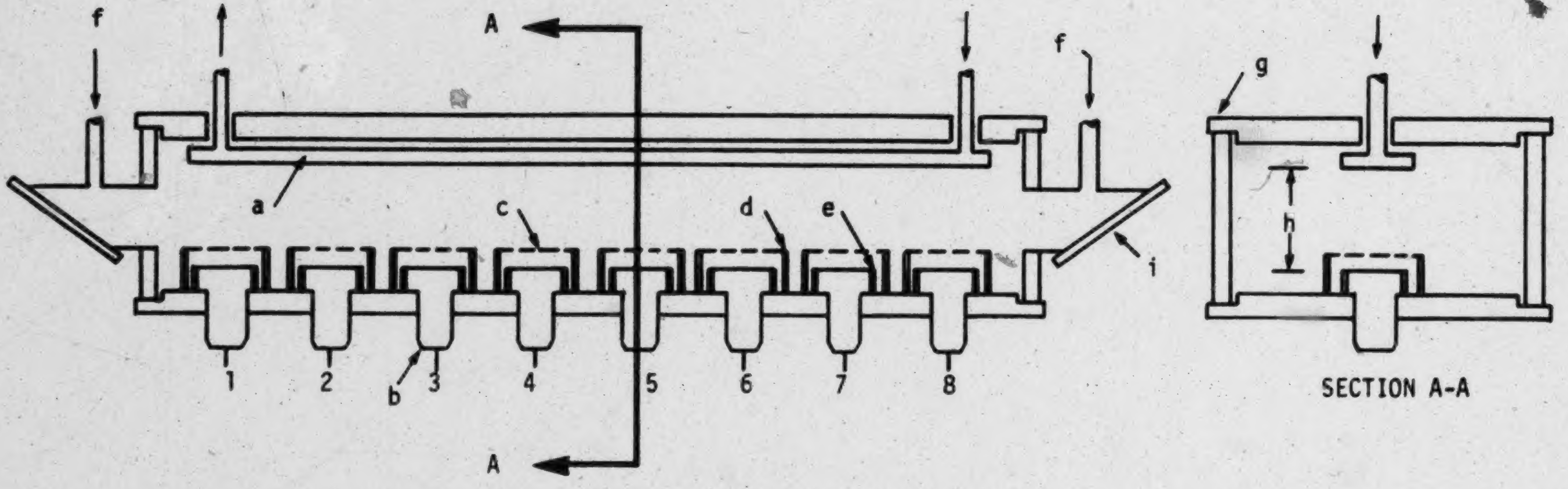

FIGURE 2.1(a). SCHEMATIC DIAGRAM OF EXPERIMENTAL LASER

(a) Water-cooled anode, length 38 cm
(b) Water-cooled cathodes, 2.54 cm diameter
(c) Wire grids
(d) Glass grid support ring, 3 cm diameter
(e) Cathode guard ring
(f) Axial gas flow ports
(g) Plate glass laser cavity, 5 x 8 x 43 cm
(h) Cathode-anode separation, ≈ 2.5 cm
(i) NaCl Brewster-angle windows

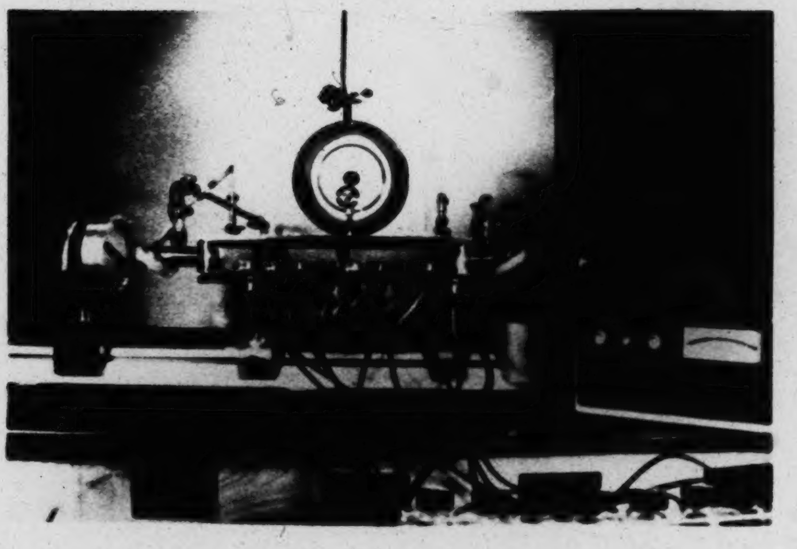

Figure 2.1(b). Transverse Discharge Laser.

Industrial grade gases were flowed axially, that is, along the laser axis by means of a mechanical vacuum pump. Pressure measurements were by a Wallace and Tiernan gauge (0-20mm Hg). Flow rates were measured and calculated using the pressure drop across a tube of known diameter and length.

The external laser resonator was formed by a 3mR gold surfaced spherical mirror and coated NaCl flat of 92% reflectivity [14]. The resonator length was approximately 80 cm. Coupling to the active medium was by means of NaCl windows (thickness of 6.5mm) oriented at the Brewster angle. Power measurements were made with a Coherent Radiation thermopile detector.

2.4 Characteristics of the Glow Discharge

2.4.1 *Action of a grid on the Voltage-Current (V-I) characteristics*

Grids of varying mesh size were inserted into the glow discharge with the most desirable effects occurring when the grid was placed into the Faraday dark space, near the termination of the negative glow. Grid sizes tested varied from 2.8 to 15.8 meshes per linear cm. (7 to 40 per inch) with open areas of 87 to 36% respectively. Aluminum, copper, and stainless steel grids were cut from plain weave wire cloth, all materials giving similar performance. The diameter of the wire was constant at 0.25 mm. This wire size was a compromise between rigidity and shadowing effects.

The V-I characteristics presented here were traced from data displayed on an X-Y recorder. All recordings were made by starting at the highest current and after stabilization, reducing the current in small steps allowing time for equilibration. The grid action is first introduced by examining the characteristics for an isolated grid.

(a) *V-I characteristics for isolated grids*

An isolated grid produced a significant increase in the potential across the active medium, thereby increasing the average electron energy to provide a higher vibrational excitation rate. The position of the grid was governed first by the fact that it was most effective in the Faraday dark space. Secondly, for a given anode-cathode separation the active volume was maximized by placing the grid close to the termination of the negative glow. It has been pointed out in Chapter 1, section 1.2.1, that the negative glow length increases with cathode fall potential, V_c. Since the discharge operated primarily in the abnormal regime (increasing V_c with discharge current, I_D), raising

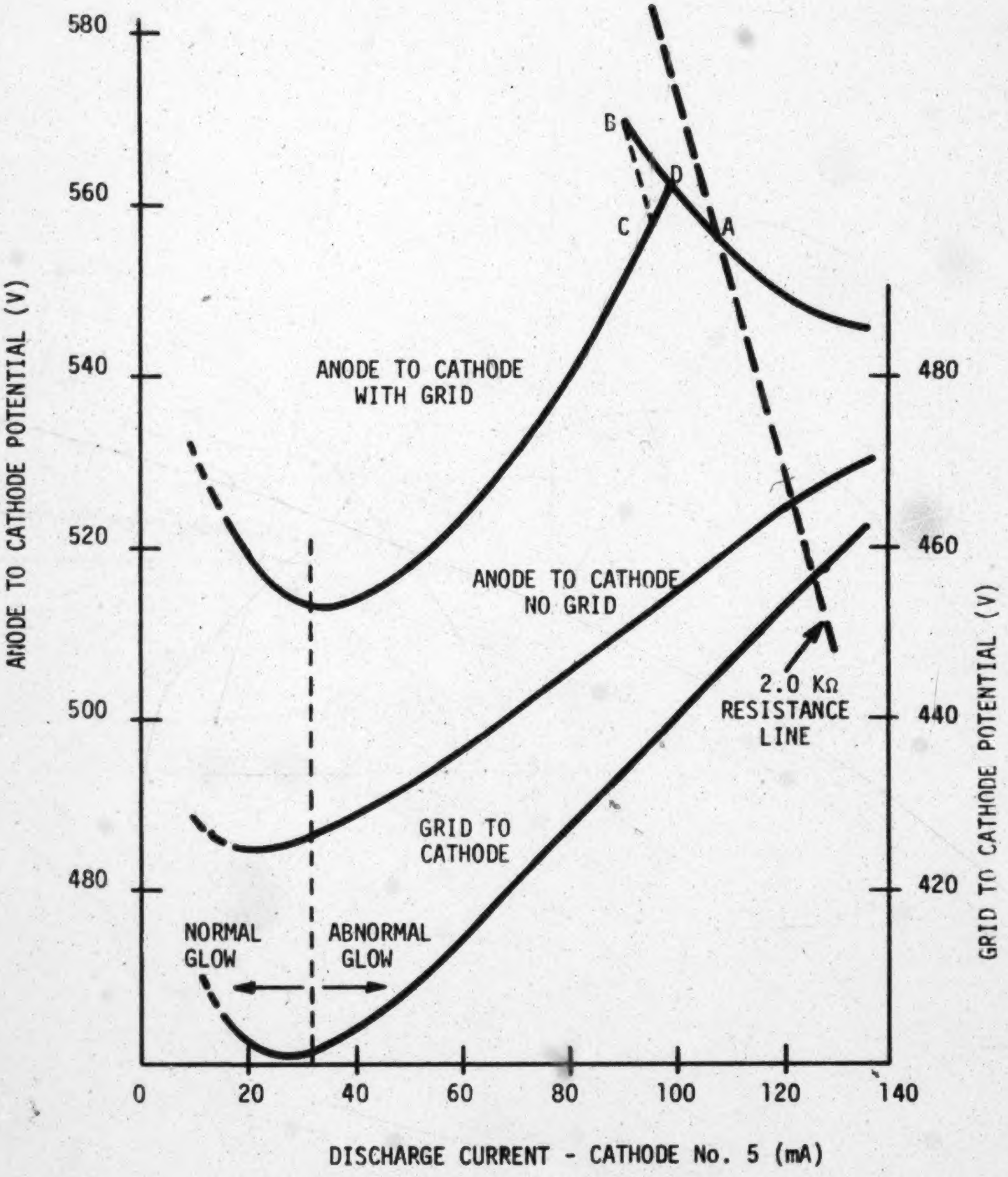

FIGURE 2.2. V-I CHARACTERISTIC FOR ISOLATED GRID.

$CO_2/N_2/He$ - 1.4/1.4/8.3 mm; pumping speed, 6.4 liters/sec; Cu annular groove cathodes; d_{GC}, 4.1 mm; d_{AC}, 2.9 cm; grid size, 16 meshes/inch.

the electrical input power caused the negative glow to expand. As a result, the cathode to grid distance, d_{GC}, was determined by the input power for optimum laser operation.

Observation of Figure 2.2 gives the relationship of the V-I characteristic for a given d_{GC} compared to that obtained in the absence of the grids. The grid produced a local maximum in discharge potential, V_D. This peak was coincident with the maximum visible glow from the positive column formed in what had formerly been the Faraday dark space, Figure 2.3(a). At 100mA (current for a single cathode) V_D was raised approximately 50V above that for no grids, that is, the average positive-glow field intensity increased from 28 V/cm to 48 V/cm. The field was calculated using the lower curve of Figure 2.2, the floating grid to cathode potential. As will be shown later, section 2.7, this change of field intensity corresponded to an increase of electron energy for which Nighan [9] has calculated a rapid variation of vibrational excitation rates.

Hysteresis existed on the low current side of the peak. This was associated with the transition of the grid end of the positive column from an attached *spot* on the grid to a distributed glow separated from the grid by a small dark space as seen in Figure 2.3(c). The positive glow became *attached* to the grid, for instance, by a current reduction from point A to B, Figure 2.2, with a transition or jump along the 2KΩ resistance line to a *spot* at point C. A subsequent current increase traced the characteristic from C to D as the spot was forced from the grid. To reiterate, below the peak the column was attached to the grid on the downstream side while for currents above, the column was separated from the grid by a thin dark space.

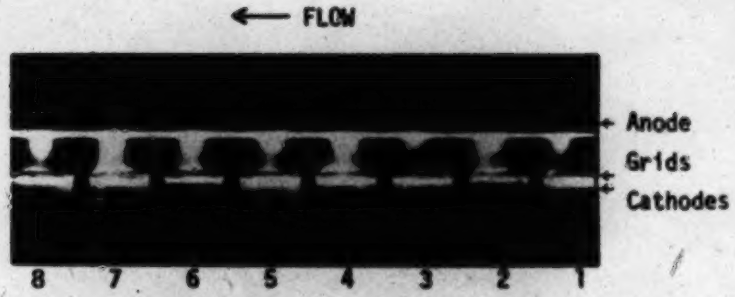
← FLOW
Anode
Grids
Cathodes
8
7
6
5
4
3
2
1

(a) Isolated Grids, $d_{GC}=4mm$.

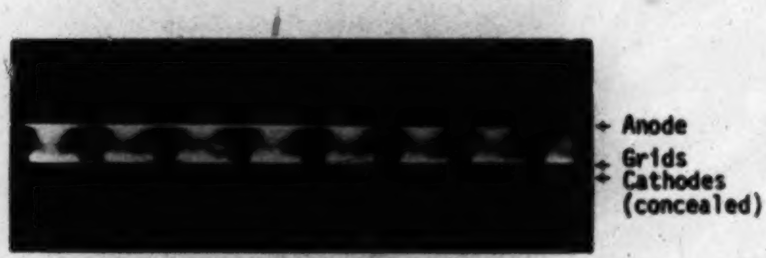
Anode
Grids
Cathodes
(concealed)

(b) Biased Grids (Section 2.4.1 (c)), $d_{GC}=2.4mm$, $R_1=28K$, $R_2=68K\Omega$

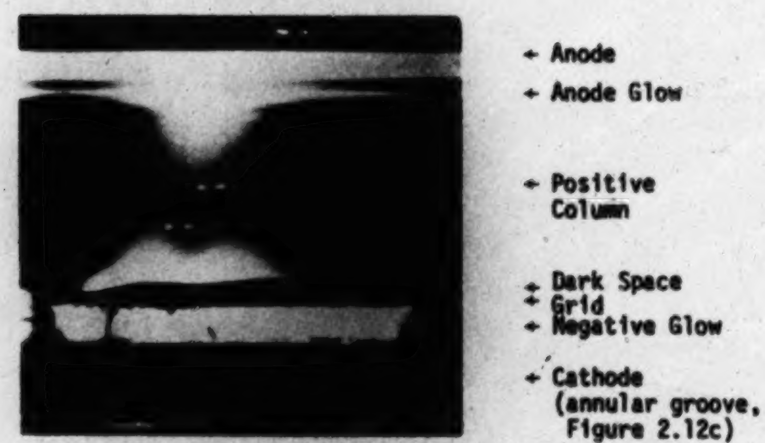
Anode
Anode Glow
Positive Column
Dark Space
Grid
Negative Glow
Cathode (annular groove, Figure 2.12c)

(c) Isolated Grid, $d_{GC}=4mm$.

FIGURE 2.3. TRANSVERSE DISCHARGE WITH 16 MESH GRIDS

$CO_2/N_2/He$-1.4/1.4/8.3mm; I_D, 1.2A; d_{AC}, 2.9 cm; grid, 16 meshes/inch, 68% open area; flow from right to left; NOTE: reflections parallel to laser axis are from scratches in glass side-wall.

Once the most intense glow had been established, further raising of the discharge current caused the glow intensity to fall, with a corresponding reduction in V_D, until finally the negative glow projected through the grid. When this occurred the grid became much less effective.

Both the current at which the peak occurred and the sharpness were a function of the grid to cathode distance, d_{GC}, as seen in Figure 2.4. For d_{GC}<2mm the peak was located on the negative slope with a small current width. To employ this d_{GC} required a relatively high ballast resistance to maintain a stable glow peak. Also, instability was further introduced by the fact that the cathode was no longer completely covered by negative glow. The case d_{GC}=2.4mm was desirable with regard to efficiency since maximum positive glow potential was obtained at minimum cathode drop and therefore minimum power loss in the cathode region. It was found, however, that a peak at higher I_D gave maximum laser power. For d_{GC}=4.1mm gentle slopes required relatively small ballast. This more gentle slope was attributed to a non-linear variation of negative glow length with cathode fall, V_C.

(b) *V-I characteristics for constant grid to cathode potentials*

To test the performance of various mesh sizes characteristics were plotted with constant grid to cathode potentials, V_{GC}, and the following discharge parameters:

$CO_2/N_2/He$ - 1.4/1.4/8.3mm Hg
pumping speed - 6.4 liters/sec
d_{GC} - 2.4mm
d_{AC} - 2.9cm
cathodes - copper, annular groove

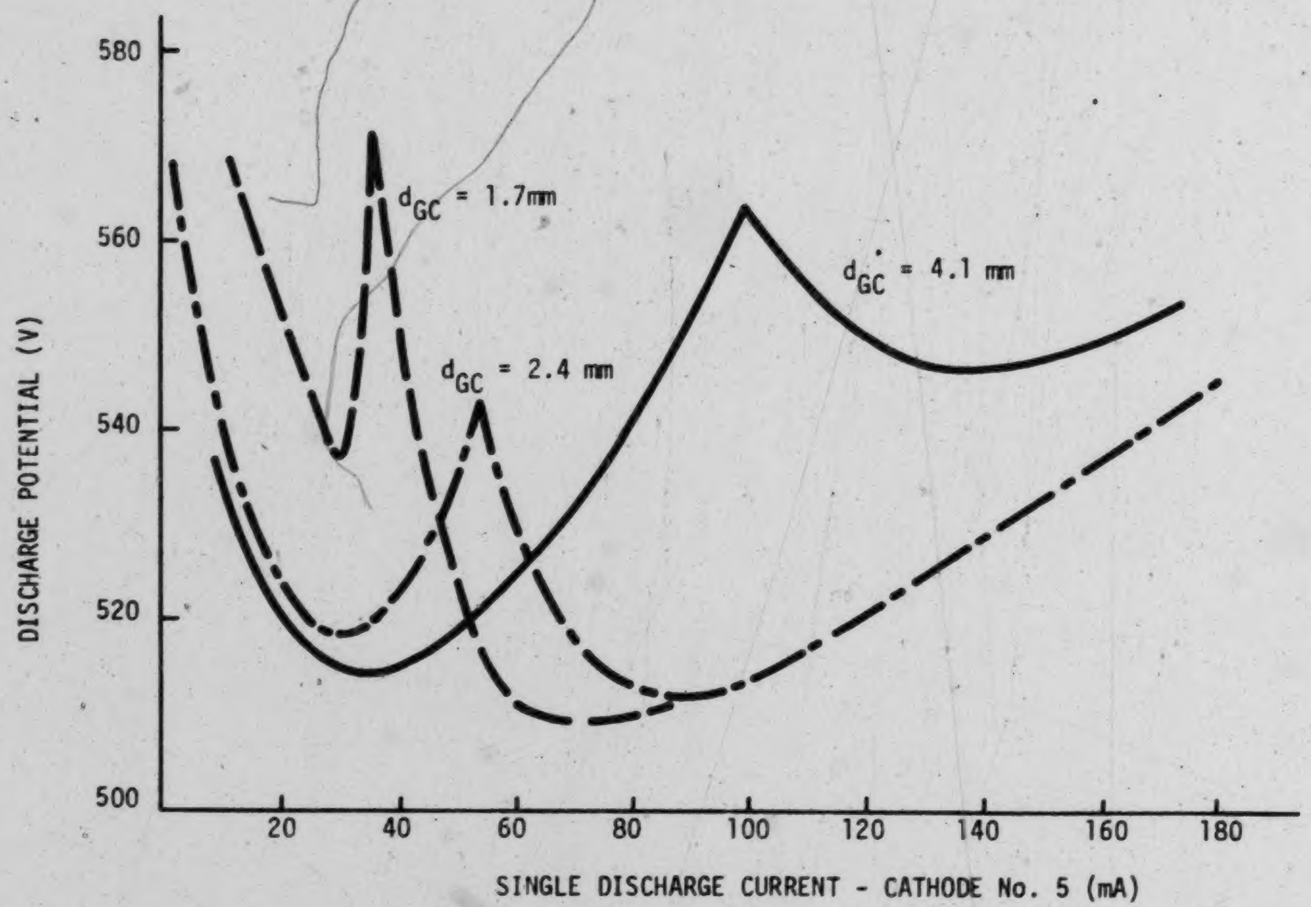

FIGURE 2.4. VARIATION OF V-I CHARACTERISTIC WITH GRID TO CATHODE SEPARATION, d_{GC}. $CO_2/N_2/He$-1.4/1.4/8.3mm; pumping speed, 6.4 liters/sec; d_{AC}, 2.9 cm; grid size, 16 meshes/inch

Grid bias was by a regulated supply (Fluke 210C) referenced to the cathode as shown in Figure 2.5. Since the grid was biased negative to space potential a bypass resistor was required on the supply to permit reverse currents. The V-I curves at floating grid potential acted as a base for those plotted with the parameter V_{GC}. Grid sizes of 6.3, 3.9, 5.5, and 7.9 meshes per cm. (16, 10, 14, 20 meshes per inch, respectively) were used to produce Figure 2.5 through 2.9.

First, a discussion of Figure 2.5 since 16 mesh grids were predominantly used for investigation of the laser gain and power. Curves of the associated grid currents are presented in Figure 2.6. Figure 2.5 has been labelled into various regions. Uniform positive glow was obtained over a rather steep characteristic in region A. In other words, for constant V_{GC} the potential across the active medium showed a large increase over a relatively small change in I_D. The curve, V_{GC}=430V gave a maximum positive glow potential of 130V (50V/cm) as compared to 75V (30V/cm) with the grid removed. The dashed line separating regions A and B gives the upper limit of stable operation. In region B, transition occurred to a grid *spot*. The grid end of the column was then constricted resulting in a higher I_D and reduced V_D. As discussed in section 2.2, the grid bias could only be increased to the point at which ionization occurred through one or more of the mesh openings. The grid current reduced to zero as expected at the intersection with the base curve (floating grid potential, V_F), Figure 2.5, with the ion current rising almost linearly with I_D, Figure 2.6. For the higher V_{GC}, the characteristic slope decreased as in the region D. This corresponded to a region of transition into what has been termed the divided negative glow [15], that is, negative glow both above and

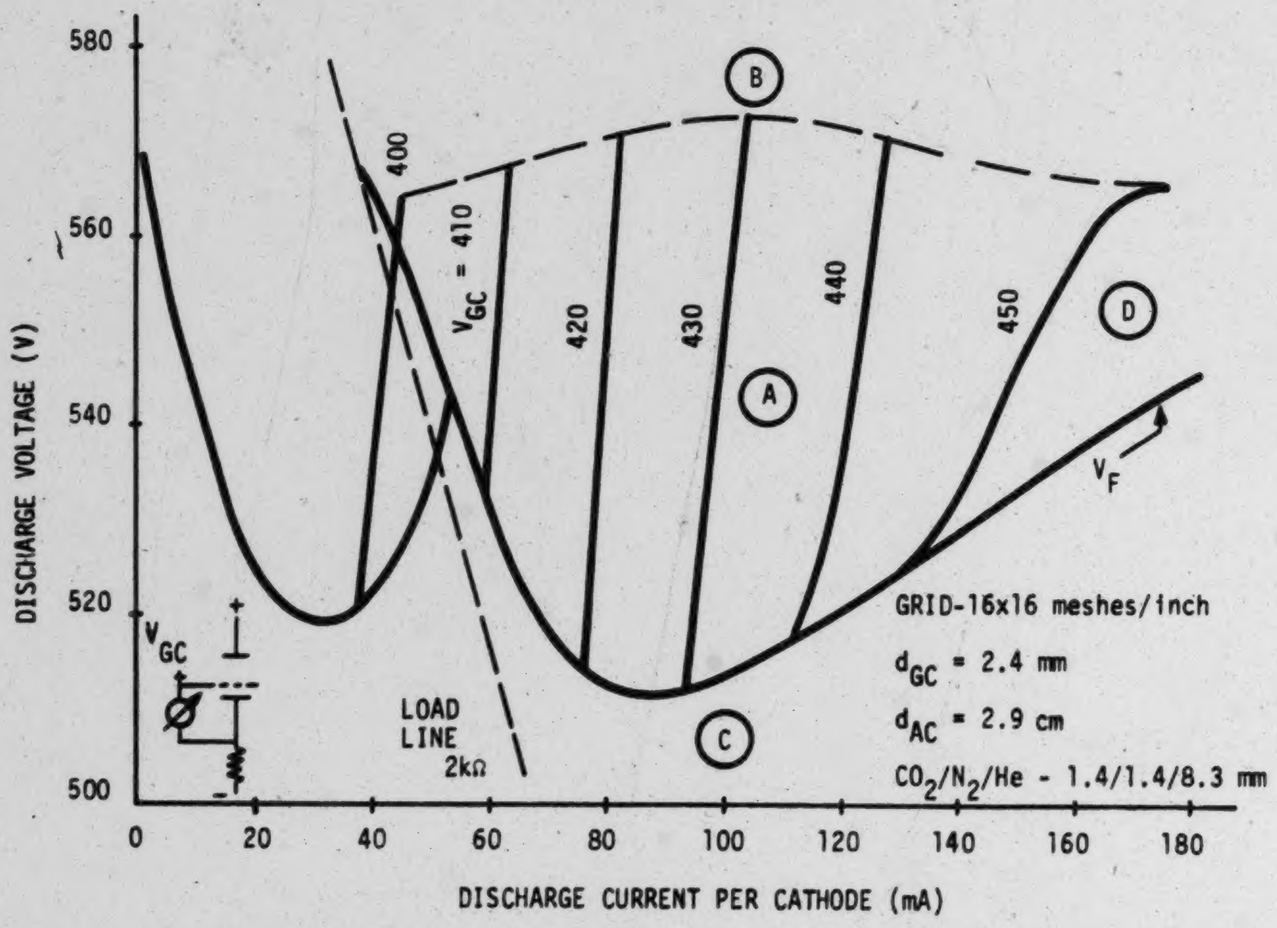

FIGURE 2.5. V-I CHARACTERISTIC CURVES FOR CONSTANT GRID TO CATHODE POTENTIALS AND 16 MESH GRIDS. Data for electrodes in position 5 downstream; pumping speed, 6.4 liters/sec.

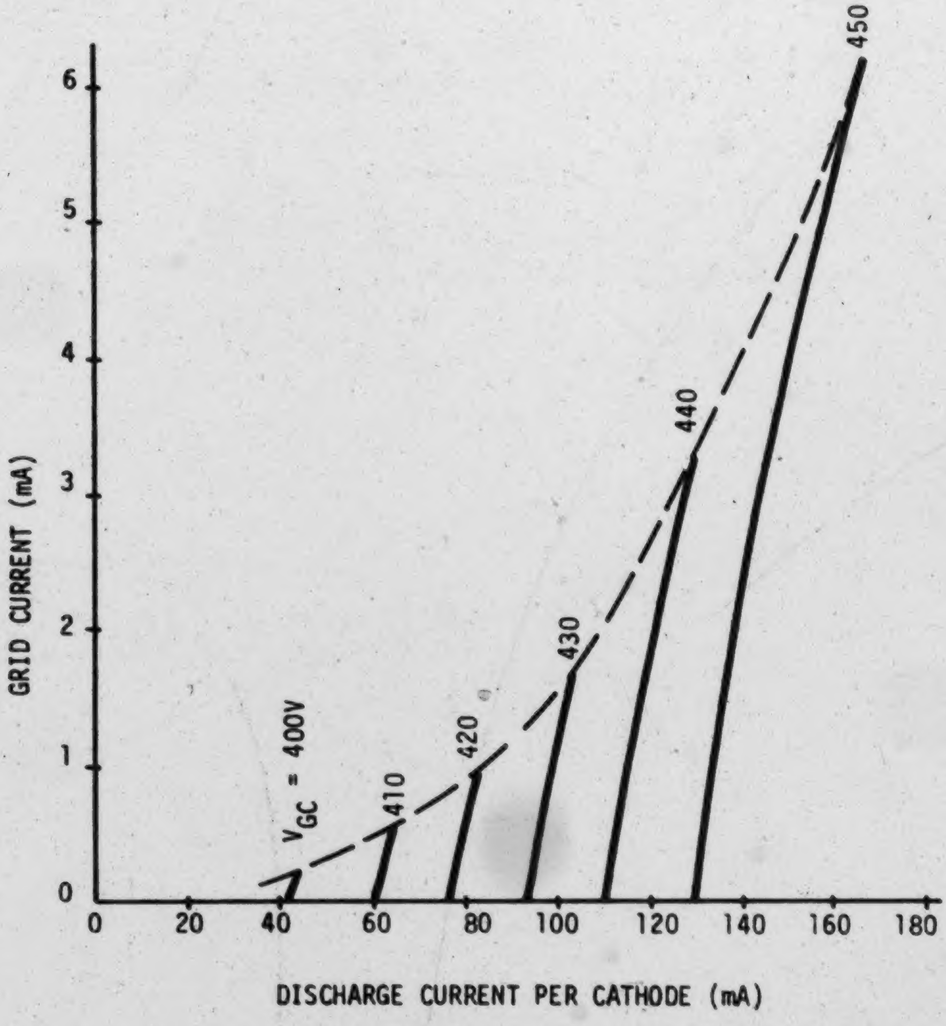

FIGURE 2.6. VARIATION OF GRID CURRENT WITH DISCHARGE CURRENT AND PARAMETER V_{GC}. Curves recorded simultaneously with FIGURE 2.5. Grid biased negative with respect to space potential.

below the grid. Once negative glow appeared above the grid, the grid-anode space was again occupied by the low laser-gain Faraday dark space. Consequently for the 16 mesh grid and this particular pressure, useful operation extended over the range 40 to 170mA per cathode.

For the 10 mesh case (3.9 meshes per cm), Figure 2.7, the curves exhibited broad maximums as compared to the almost linear relationship of Figure 2.5. A stable positive glow occurred on peaks A and B for $V_{GC}>390V$. For $V_{GC}=390V$ a uniform glow existed at point A (V_{GC} approximately 100V below plasma potential) and lesser I_D down to 20mA. In the region A to B the grid and glow interacted via a series of intense spots. Finally at point B and above the negative glow began to project uniformly through the grid. The interpretation of this behavior was that when the grid provided a certain critical loss, transition to intensely ionized spots permitted the discharge to operate more economically to maintain itself. This behavior was similar to the region B of Figure 2.5. On closer inspection of Figures 2.7 and 2.5, the grid bias for the large mesh openings had to be increased substantially (from a few volts to several tens of volts). This was expected since the grid wires were assumed to be effective out to a diameter of the ion sheath which expands for more negative bias.

Figure 2.8, 14 mesh grid (5.5 meshes per cm) was similar to Figure 2.5. The curve for $V_{GC}=V_F$ contained a local peak on the low current negative slope at approximately 20mA. By comparing Figures 2.5 through 2.9 the local maximum of the isolated grid curve moved to higher I_D for decreasing open area. This was expected since a grid of lower

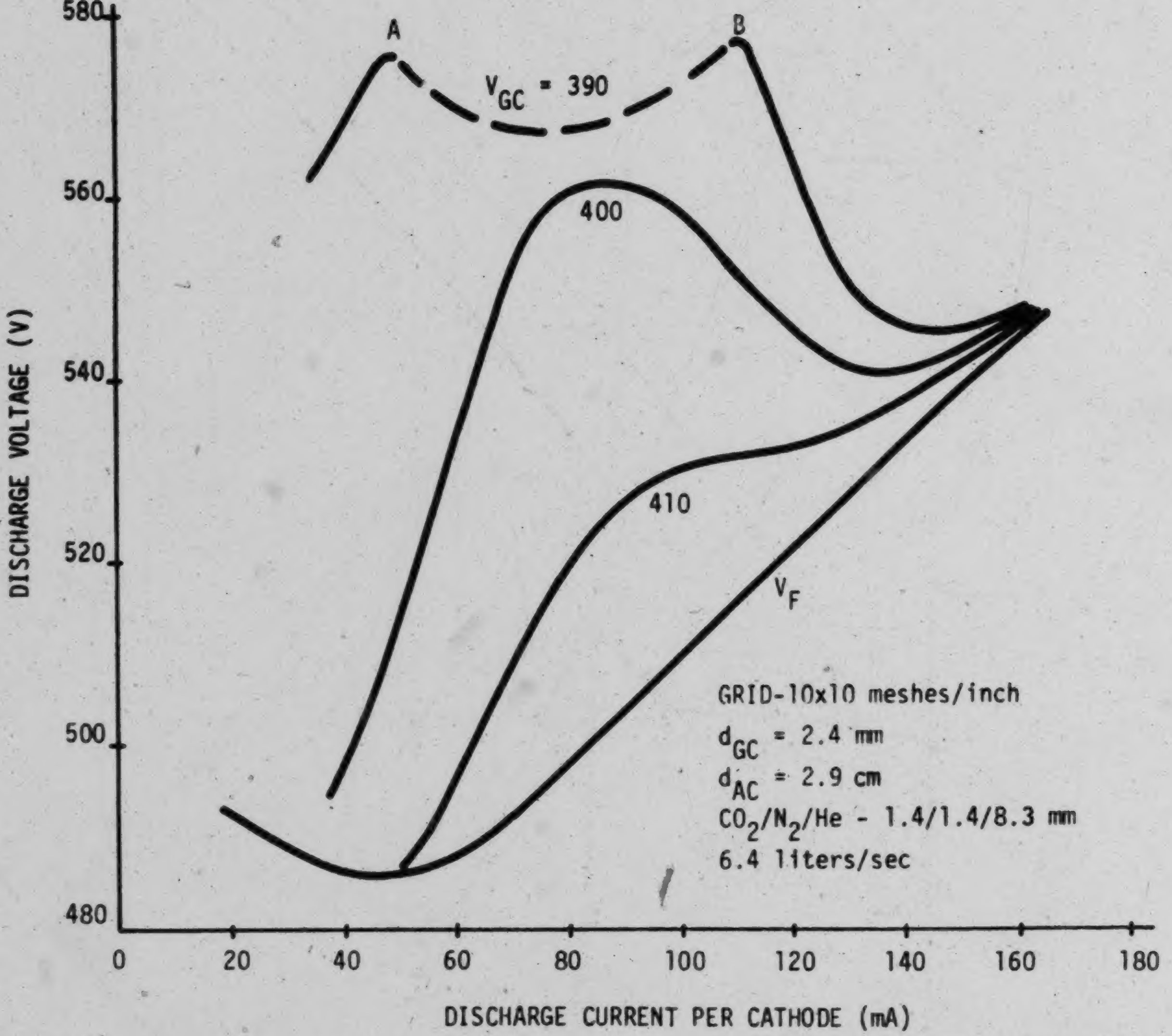

FIGURE 2.7. V-I CHARACTERISTIC CURVES FOR CONSTANT V_{GC} AND 10 MESH GRIDS.

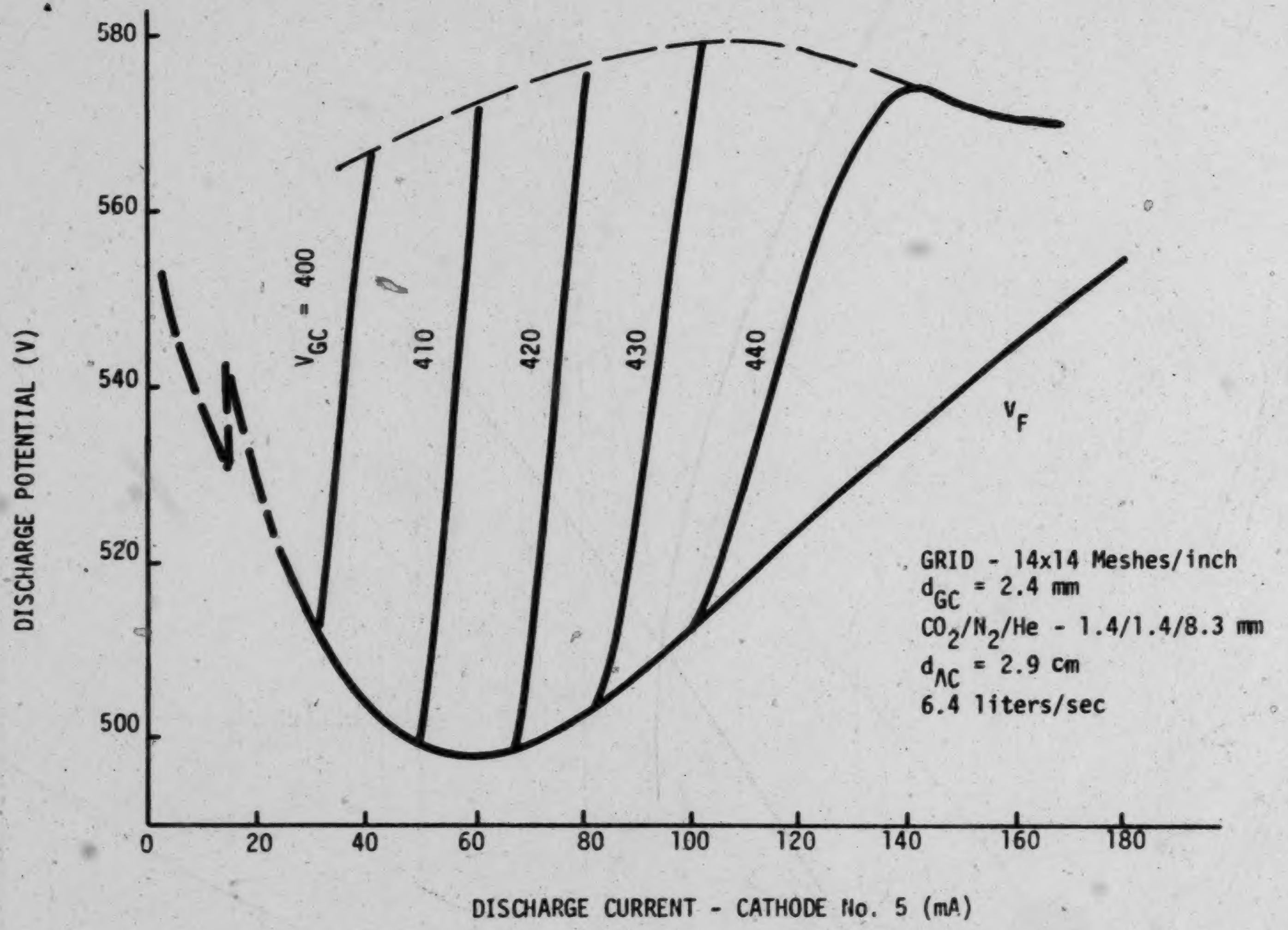

FIGURE 2.8. V-I CHARACTERISTIC WITH PARAMETER V_{GC} FOR 14 MESH GRID

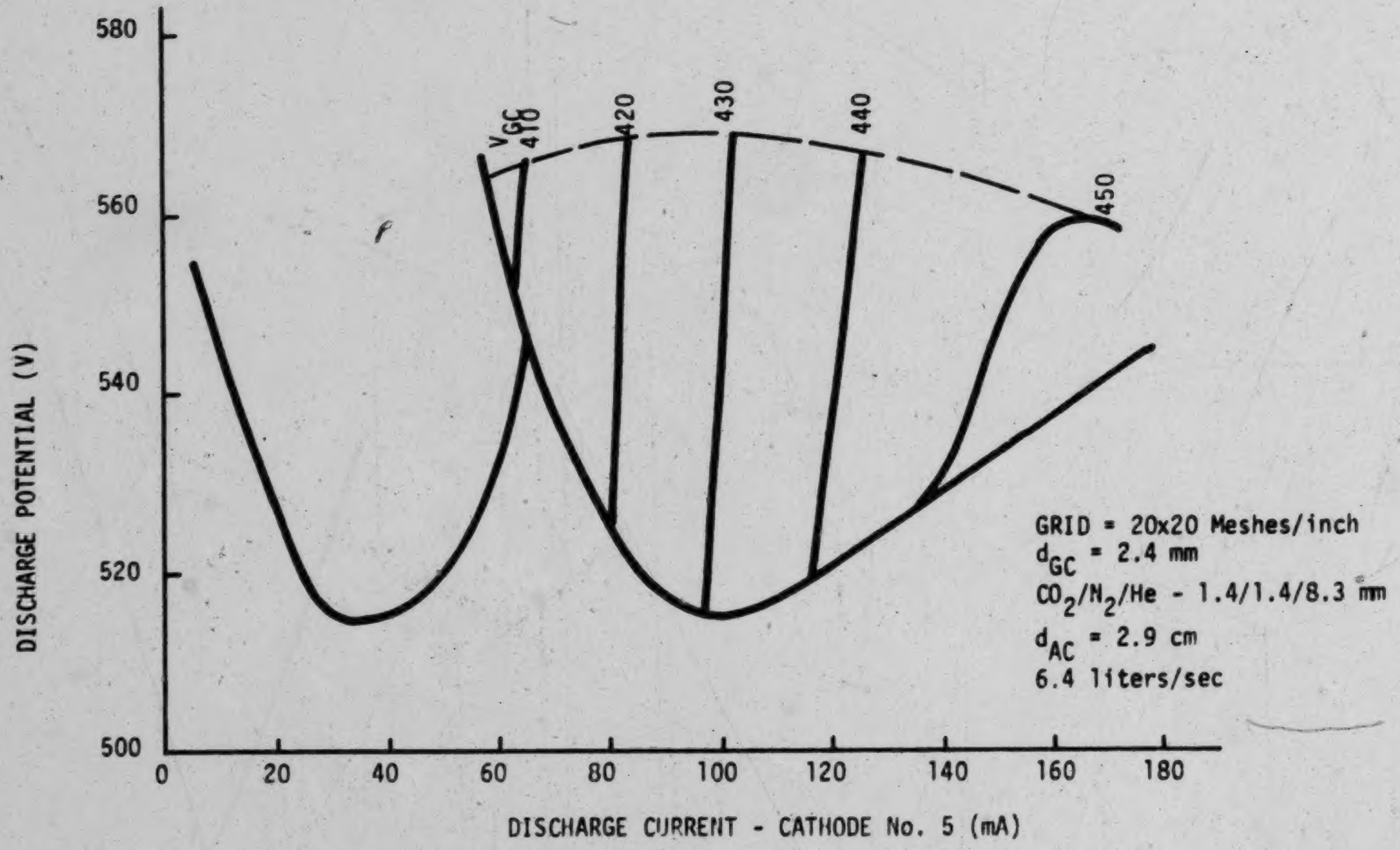

FIGURE 2.9 V-I CHARACTERISTIC WITH PARAMETER V_{GC} FOR 20 MESH GRID.

open area presented a larger collecting surface and a higher degree of sheath overlap. The negative glow expanded more closely to the grid (higher I_D) before projection through the mesh occurred.

Comparison of 16 mesh, with 20 mesh performance, Figure 2.9, indicated that the region of divided glow remained at approximately the same I_D. This coupled with the isolated grid peak moving to higher I_D for the smaller mesh, reduced the useful current width of the uniform glow region.

This rather complex behavior is summarized under the following points:

(1) decreasing the open area shifted the potential peak of an isolated grid to higher I_D.

(2) by applying various constant grid to cathode potentials the useful range of operation of a particular grid was determined as that region to the high current side of the isolated peak, up to the I_D of the divided negative glow.

(3) increasing the negative bias in this region produced a large increase in positive glow potential with a corresponding visible intensification of the positive glow.

(4) maximum grid bias allowed was dictated by the transition from a thin dark space above the grid to one or more spots of ionization through the grid as the discharge reverted to more economical operation.

(5) reduction of the grid open area, lowered the useful current range.

(c) *V-I characteristics for a self-biased grid*

It is recalled from Figure 2.5 that for the 16 mesh grid and constant V_{GC} rather steep characteristics were obtained of limited current range. These characteristics were useful for establishing the most desirable region of operation, however, to extend the operating range a simple self-bias resistance network was designed as shown in Figure 2.10. Using V-I characteristics at constant V_{GC} and the corresponding curves of grid currents, values of R_1 and R_2 were estimated from the following expression:

$$\left(\frac{V_{GC}}{R_2} - I_G\right) R_1 + V_F = V_D \qquad \text{. . . (2.7)}$$

V_{GC} = potential of V-I curve of constant V_{GC} passing through the desired operating point, Figure 2.5.

I_G = grid current at the specified I_D, Figure 2.6.

V_F = floating grid to cathode voltage at I_D, Figure 2.5.

V_D = discharge voltage obtained from V-I curve at intersection of V_{GC} and I_D, Figure 2.5.

From (2.7), V_{GC}/R_2 must be greater than I_G to provide the necessary grid current.

The V-I characteristics for a self-biased 16 mesh grid are contained in Figure 2.10. The curves were produced for R_2 constant at 68KΩ and various values of R_1. The V-I curves for self-bias are shown superimposed on the isolated grid characteristic. Operating range was obviously extended and the lower gradients led to further

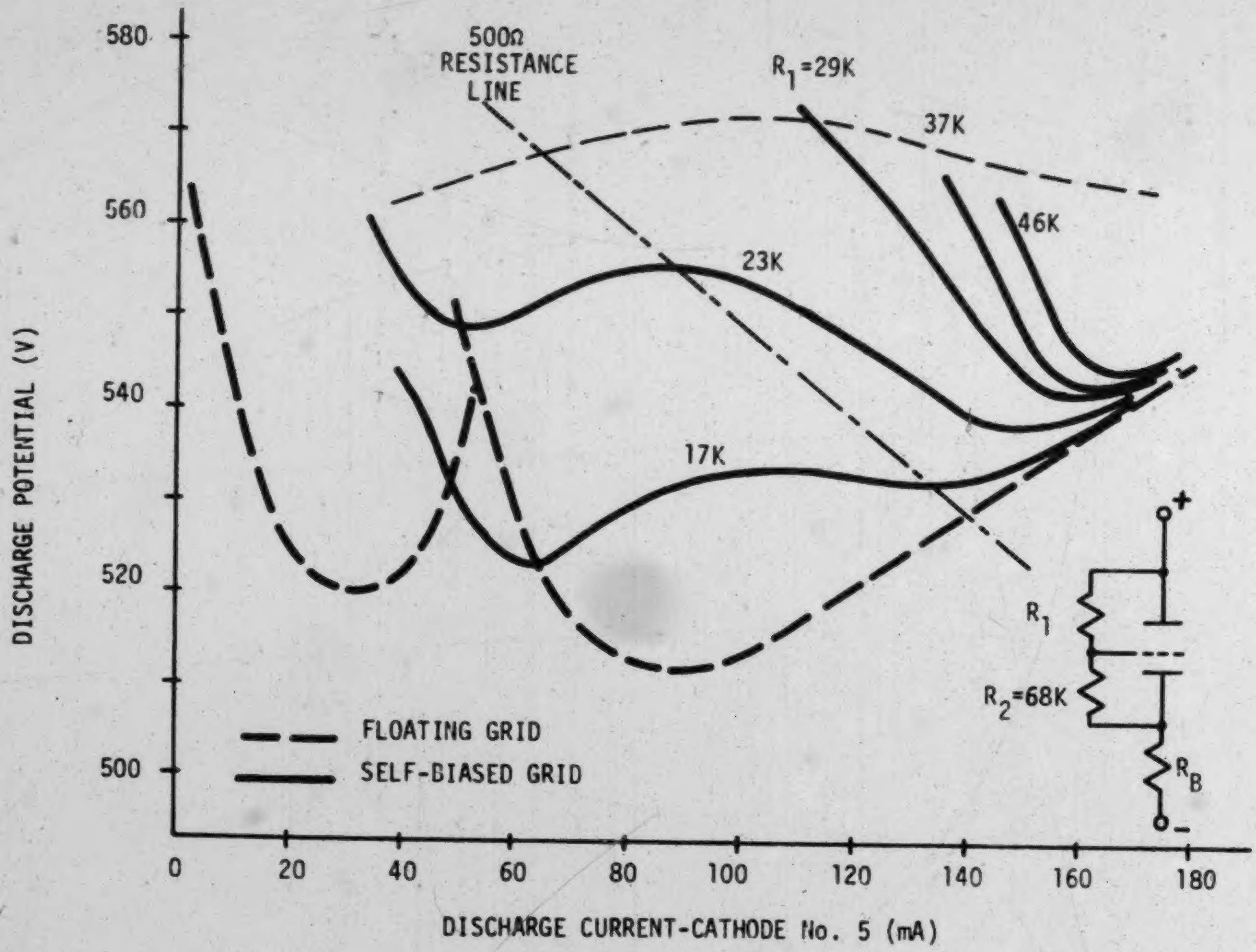

FIGURE 2.10. V-I CHARACTERISTIC FOR SELF-BIASED GRID.
$CO_2/N_2/He$ - 1.4/1.4/8.3 mm; pumping speed, 6.4 liters/sec; Cu annular groove cathodes; d_{GC}, 2.4 mm; d_{AC}, 2.9 cm; grid size, 16 meshes/inch; R_2 constant, 68K

reduction of the cathode ballast. A resistance line of 500Ω is shown. Since V_C was in the order of several hundred volts (V_C=V_F for high current) reduction of the ballast below 500Ω resulted in little economy of power. For instance, a single cathode current of 100mA, and V_C=V_F = 440V, gave a power consumption of approximately 44W in the cathode fall as compared to 5W in the cathode ballast.

2.4.2 *Variation of V-I characteristics with pressure*

To illustrate the effects of density changes the discharge characteristics of Figure 2.11 were generated for a constant ratio of gas constituents. There was an obvious shift of the maximum visible glow to higher current and potential changes became more gradual. These changes were assumed to be associated with the reduction of negative glow length with pressure [16]. In fact the curves of Figure 2.11 were similar to those for changing grid to cathode spacing, Figure 2.4.

The glow column for a pressure of 5.4mm was not uniform along the grid-anode space. It would seem that the grid caused only a local change in the plasma just above the grid. Losses further removed were not sufficient to boost the electron energy and thereby extend the visible positive glow. This phenomena had the appearance of a striation produced in low pressure gas and a more conventional long tube discharge [17].

By inspecting the curves more closely it is observed that each glow peak was superimposed on a curve of diminishing potential variation as the pressure was raised. This was consistent with experiments performed with single component gases [18]. The point

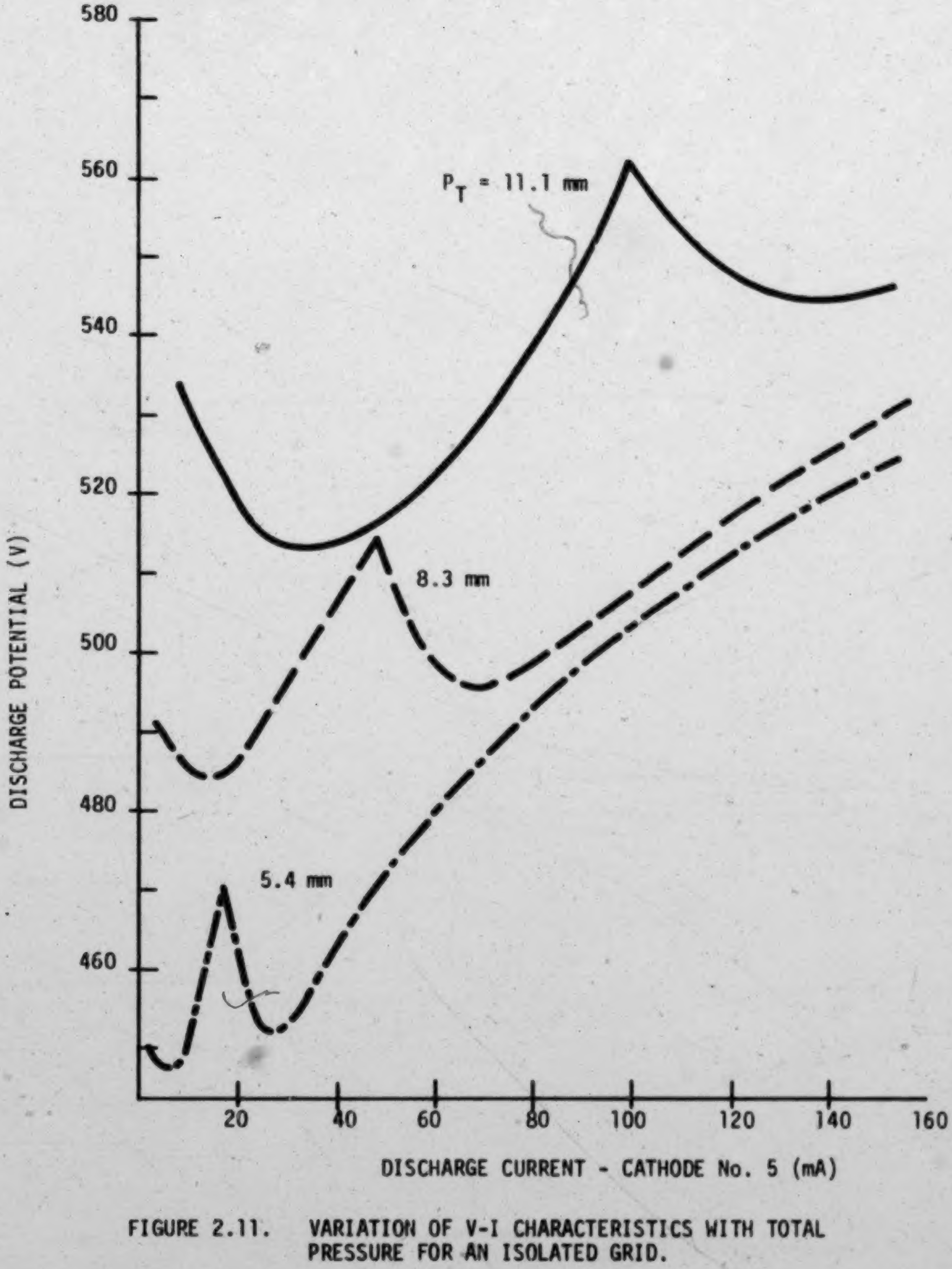

FIGURE 2.11. VARIATION OF V-I CHARACTERISTICS WITH TOTAL PRESSURE FOR AN ISOLATED GRID.

$CO_2/N_2/He$ - 12.6%/12.6%/74.8%; pumping speed, 6.4ℓ/sec; grid size, 16 meshes/inch, d_{GC}, 4.1 mm; d_{AC}, 2.9 cm.

should be emphasized that this behavior was responsible for expanding the region of operation, that is, region A, Figure 2.5. In other words the V_D minimum, corresponding to normal cathode fall, V_n, broadened and the potential of the abnormal region rose less rapidly. From characteristics run at constant V_{GC}, it was established that this was necessary to extend the useful range of operation of a grid.

2.4.3 *Electrode geometries and materials*

The various shapes tried were the flat, the hollow, the inverted brush and the annular groove cathodes shown in Figures 2.12(a) through 2.12(d), respectively.

The flat cathode gave an extended negative glow (approximately 1 cm for 100mA discharge current and total pressure of 11.1mm with partial pressures $CO_2/N_2/He$-1.4/1.4/8.3mm). In order to minimize the electrode separation a reduced negative glow length was desired.

From von Engel [19] one finds that the hollow cathode has properties of reduced external negative glow and lower V_C for a given current density. Since the intense negative glow is confined to the interior of the electrode a reduction in gas heating effects is also expected over and above the reduction due to lower V_C. For the eight-electrode structure tested in these experiments, with 3.8 cm distance between centers, it was found that the hollow cathode confined the positive glow unnecessarily. An obvious experiment is to move the electrodes closer together. This was not done on this structure, however, as will be seen in Chapter 3 a similar structure employing approximately thirty cathodes gave a continuous discharge over the axial length of the laser.

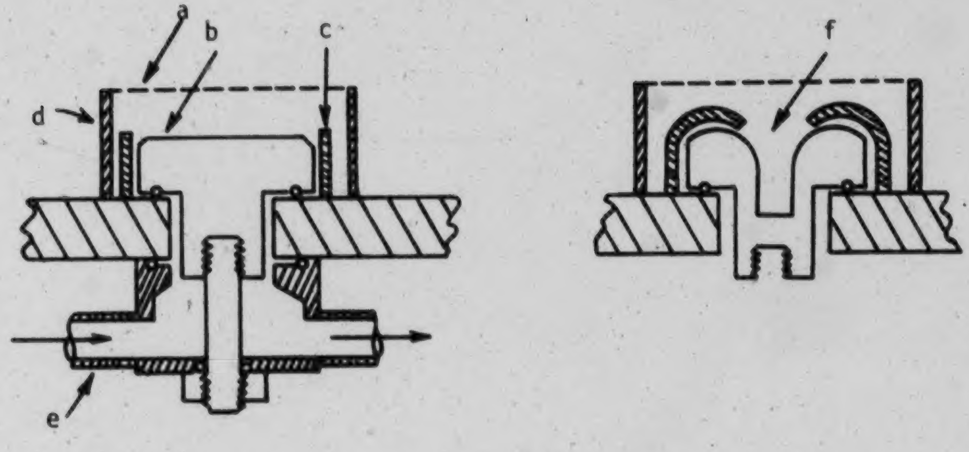

(a) FLAT CATHODE

(b) HOLLOW CATHODE

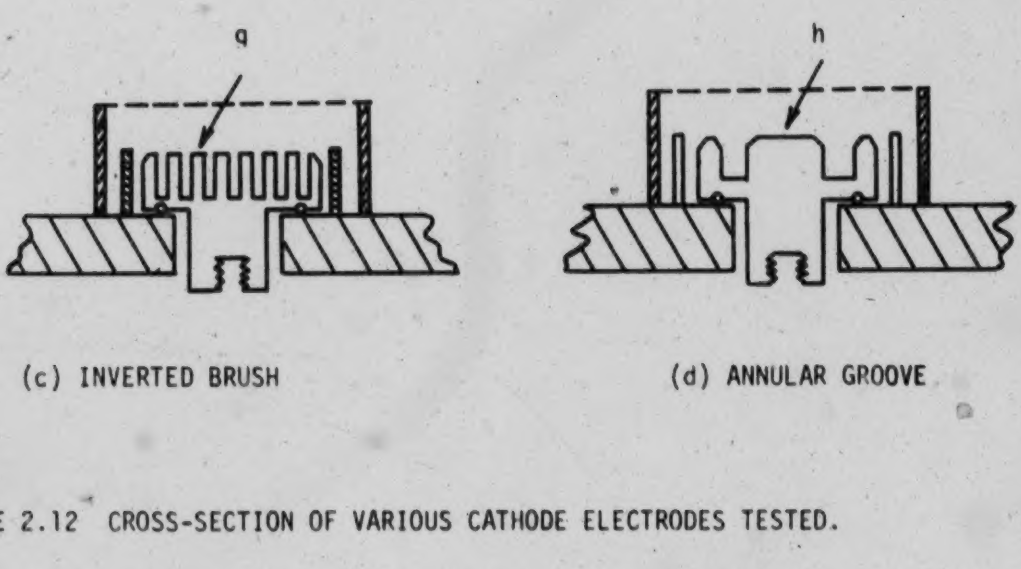

(c) INVERTED BRUSH

(d) ANNULAR GROOVE

FIGURE 2.12 CROSS-SECTION OF VARIOUS CATHODE ELECTRODES TESTED.

a - grid

b - flat cathode surface, 2.5 cm diameter

c - glass guard ring

d - glass grid support, 3.3 cm i.d.

e - coolant assembly

f - hollow cathode

g - inverted brush cathode

h - annular groove cathode

The structure of Figure 2.12(c) again employed the principles of the hollow cathode in that now the complete surface of a 2.5 cm diameter electrode was covered with hollow cathodes creating an "inverted brush" electrode. Since the hollow cathode effect becomes more pronounced for smaller diameters at a given pressure, there existed a certain minimum hole diameter which depended on the number of holes in the surface, the pressure, and the discharge current. If the hole diameter was too small not all the hollow cathodes were required to support the discharge. Also the cathode region became spatially unstable as the glow "danced" over the surface. A copper electrode with 7mm diameter holes was found to be stable for pressures above 10mm with the discharge covering the whole surface. The negative glow projecting from the hollow cathodes was now in the order of one to two mm.

The multi-hollow cathode was modified to the annular groove electrode of Figure 2.12(d). This gave similar performance with some increase in negative glow length, however, difficulties of construction were greatly eased. The glow column did show some structure associated with the cathode surface as seen in section 2.4.1, Figure 2.3.

A study of various materials was conducted particularly after the initial experiments employing commercial aluminum electrodes. After a few hours of operation a highly insulative deposit built up on the cathode surface. This "contamination" took the form of a tenuous grayish-black deposit. A marked increase in discharge potential was observed after the complete surface was covered. While the deposit was forming the discharge showed a stronger tendency to arc presumably due to the insulating inclusion effect discussed by Maskrey and Dugdale [20]. Once the surface was covered small micro-discharges flashed at random over the surface. Another undesirable feature of this build up was the increased negative glow length associated with the increased V_C and attendant increase in power dissipated in the cathode region. In other words once the deposit had built up larger d_{GC} were required.

Copper, stainless steel and nickel cathodes maintained relatively clean surfaces at the expense of sputtering action. This sputtering action did not appear objectionable in the flowing system but would be a highly objectionable situation for a sealed off system where electrode effects manifest themselves in the form of gas clean-up both due to gettering action and chemical reaction with the electrode surfaces.

Briefly, the anode materials tried were again aluminum and copper in the form of single continuous water-cooled rectangular channel. No particular advantage was found of one over the other, but copper was favoured because of higher thermal conductivity. The width of the anode had an effect on the axial continuity of the discharge. By restricting the anode width the positive glow was forced to spread in the axial direction. The minimum useful width was slightly greater than that at which intense "tuffs" of glow formed along the surface.

V-I characteristics for the various cathode materials are contained in Figure 2.13, which it is to be noted were generated in the absence of grids in order to more clearly show the changes in V_C. The curve for aluminum was for a freshly polished surface. Aluminum exhibited the lowest V_D and therefore the least V_C. Once coated by the discharge, V_C for aluminum became much higher even than that for

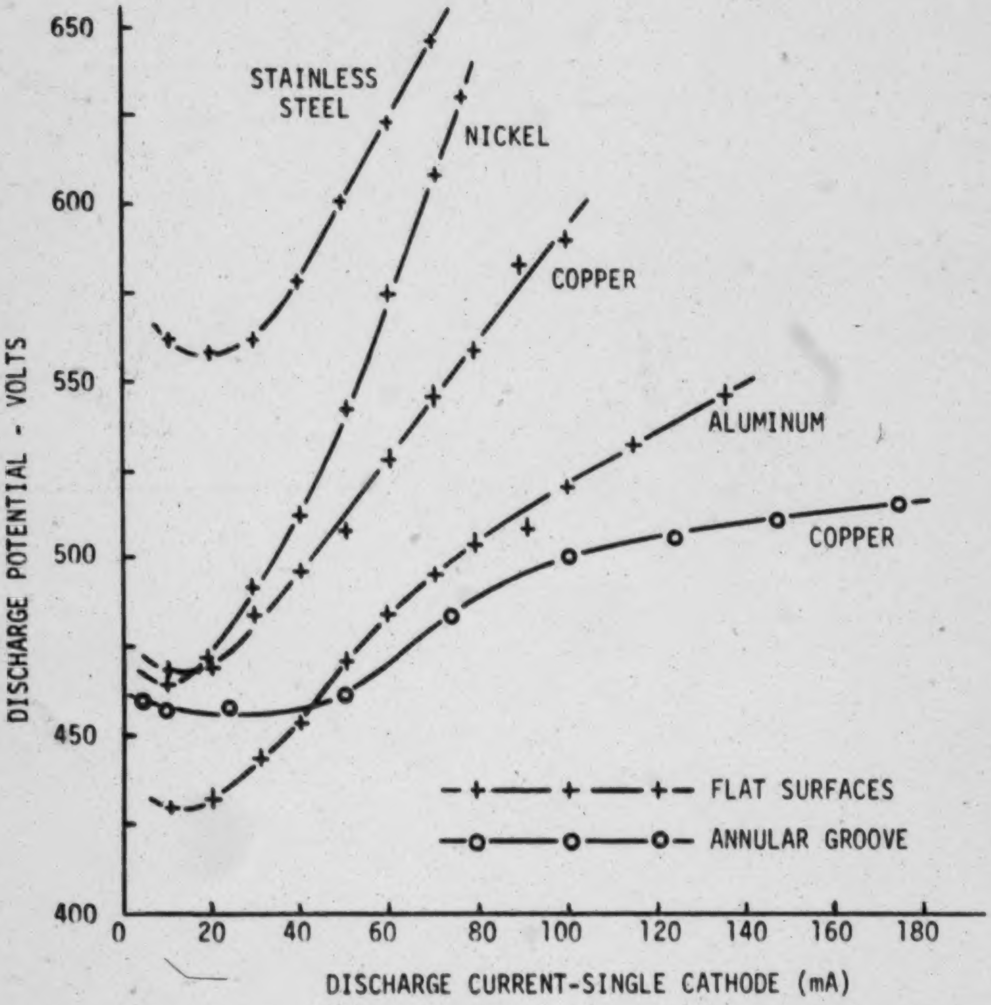

FIGURE 2.13. V-I CHARACTERISTICS OF VARIOUS CATHODE MATERIALS WITHOUT GRIDS. $CO_2/N_2/He$ - 1.5/1.5/8.0 mm; pumping speed, 5 liters/sec; d_{AC}, 2.5 cm; cathode diameter, 2.5 cm; annular groove dimensions, 10 mm i.d. x 17 mm o.d. x 4 mm deep.

stainless steel. As mentioned previously a low V_C minimizes gas heating, negative glow length and increases laser efficiency by reducing the power consumed in the cathode region. The effectiveness of V_C reduction by use of a multi-hollow or annular groove cathode is illustrated in Figure 2.13.

2.5 Small signal amplification

Since high sensitivity was desired for gain measurements, particularly in the Faraday dark space and the negative glow, a differential technique was used, Figure 2.14. A similar version appeared in reference [21].

By chopping two equal amplitude beams alternately and superimposing them at the detector the effects of low frequency noise, particularly amplitude drift of the probe oscillator, were greatly reduced. A lock-in amplifier was tuned to the chopping frequency, with the gain amplitude displayed on an X-Y recorder. Typical oscillator probe powers through the test medium were 100mW on one of the P transitions of the 10.6μ group, the particular transition monitored by a CO_2 laser spectrum analyzer (Optical Engineering INC., model 16-A). An iris in the larger amplitude leg was adjusted for complete cancellation of the chopped signal in the absence of the amplifying discharge.

The variation of the small signal gain with discharge current is shown in Figure 2.15, where the amplification for two different isolated grid positions is compared to that obtained in the absence of the grids. Constant partial pressures were maintained as was the flow rate. As illustrated by Figure 2.15 the gain peak shifted to a higher discharge current with increasing d_{GC}. The magnitude of the gain varied inversely

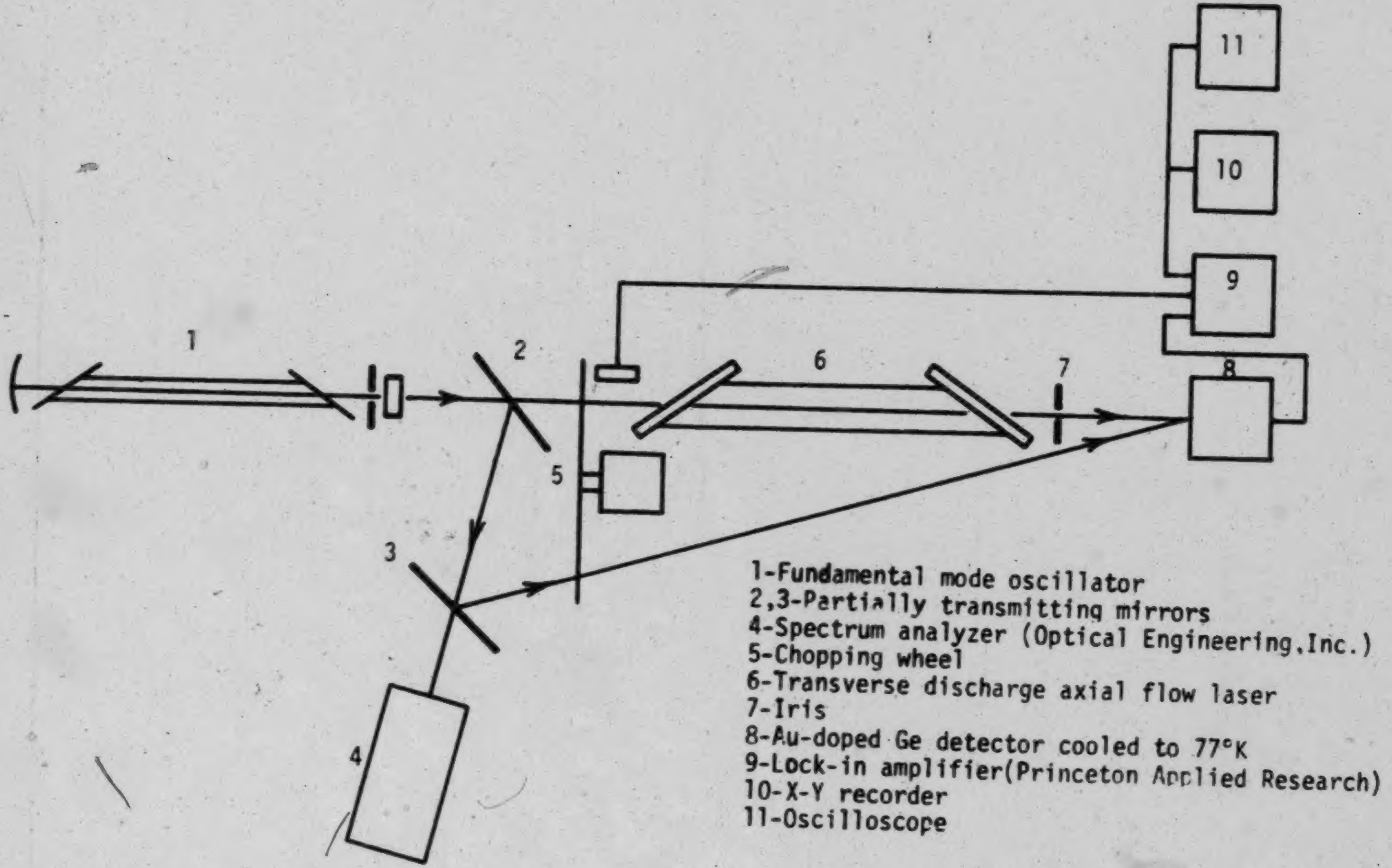
1
2
3
4
5
6
7
8
9
10
11
1-Fundamental mode oscillator
2,3-Partially transmitting mirrors
4-Spectrum analyzer (Optical Engineering,Inc.)
5-Chopping wheel
6-Transverse discharge axial flow laser
7-Iris
8-Au-doped Ge detector cooled to 77°K
9-Lock-in amplifier(Princeton Applied Research)
10-X-Y recorder
11-Oscilloscope

FIGURE 2.14. EXPERIMENTAL SETUP FOR RECORDING SMALL-SIGNAL GAIN OF TRANSVERSE DISCHARGE AXIAL FLOW LASER.

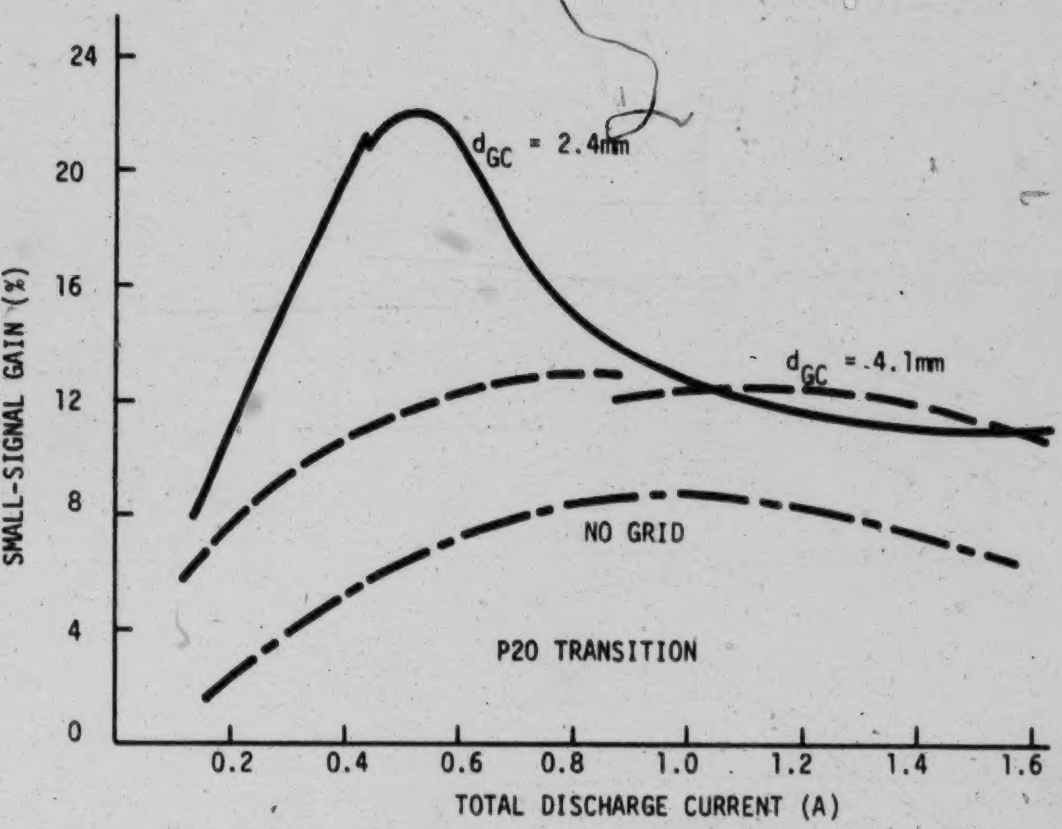

FIGURE 2.15. THE DISCHARGE CURRENT DEPENDENCE OF THE SMALL SIGNAL GAIN FOR VARIOUS ISOLATED GRID POSITIONS. $CO_2/N_2/He$ - 1.4/1.4/8.3mm; GRID SIZE, 16 MESHES/INCH; PROBE BEAM POSITIONED CENTER OF ANODE-GRID SPACE; d_{AC}, 2.9cm; PUMPING SPEED, 6.4 LITERS/SEC. GAIN IS DEFINED AS THE PERCENTAGE INCREASE IN PROBE POWER.

with d_{GC}. Compared to the case without grids, a factor of two improvement in gain was produced at low d_{GC}. As will be seen in the next section the larger d_{GC} (and I_D) gave the maximum laser power. This behavior was similar to a conventional tube laser, in that the output power maximized at a higher current than the gain [22]. The lower gain peaks for large d_{GC} were attributed to the gas heating caused by higher I_D. Both experimental and theoretical investigations have shown that the gain is a strong function of the translational temperature [23] [24] [26] [25].

The break in the gain curves occurred at the point where glow attachment took place to the downstream edge of the grid. Consequently, for some grid settings, (d_{GC}=4.1mm, Figure 2.15) the gain after attachment was higher due to a slight contraction of the positive glow column.

In regard to errors involved in the gain measurements, scans were repeatable to $\Delta G = \pm 2\%$ for copper electrodes. Since small changes in d_{GC} resulted in significant shifting of the gain-current characteristic, care had to be taken in adjustments of d_{GC}. Changes in the electrode surfaces also detracted from the long-term repeatability. This was particularly true of the aluminum cathodes, as discussed in section 2.4.3. Copper cathodes, however, showed only a slight shift of the gain maximum to lower I_D, presumably due to a small increase in the cathode fall potential.

Gas pressure and constituent variation produced similar effects to the changes of d_{GC}. Figure 2.16 displays the gain characteristic for several gas pressures at constant d_{GC}. Again, maximum amplification occurred at low I_D. The output power maximized,

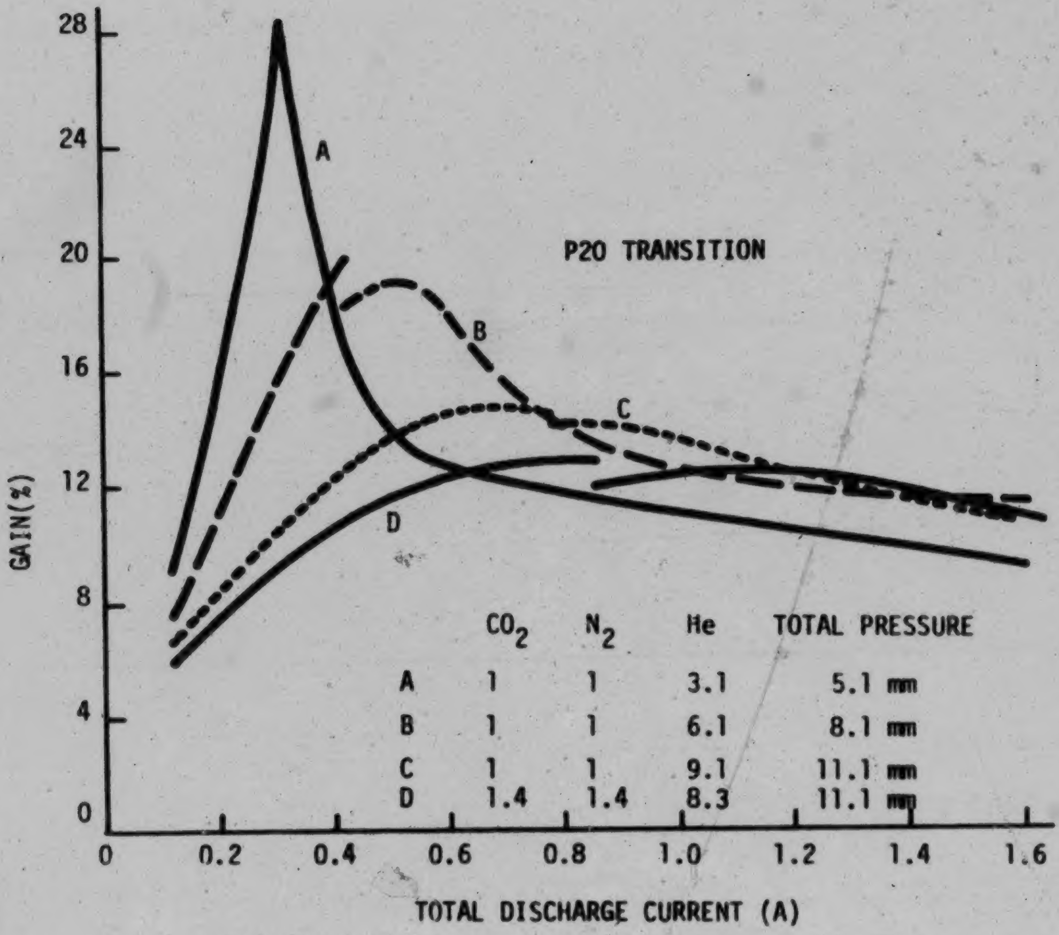

FIGURE 2.16. CURRENT VARIATION OF THE SMALL SIGNAL GAIN WITH GAS PRESSURE FOR AN ISOLATED GRID AT CONSTANT d_{GC}. GRID SIZE, 16 MESHES/INCH; d_{GC}, 4.1 mm; d_{AC}, 2.9 cm; PROBE BEAM, CENTER OF ANODE GRID SPACE; PUMPING SPEED 6.4 LITERS/SEC.

however, for the gas density of curve D.

Horizontal scans showed that at the edges of the 2.2 cm window aperture (cathode diameter, 2.5 cm) the gain had declined to approximately 50% of the center-line value. Vertical variations also occurred. The highest gains occurred in the vicinity of the anode and decreased toward the grid. As the grid was approached, the gain maximum moved to lower discharge current, direct evidence of the heating effects of the cathode fall potential.

2.6 Laser Output Power

The resonator was formed between a 3 m R gold-surfaced mirror and a coated NaCl flat of 92% reflectivity [27]. The resonator length was approximately 80 cm. The mirrors were located externally, the resonator coupled to the cavity by means of 6.5mm thick salt flats oriented at the Brewster angle. The aperture of the system was limited by the Brewster window mounts to a height of 15mm and a width of 22mm, thus restricting the mode volume to less than one-half the excited volume.

As expected from the V-I characteristics of section 2.4.1, maximum laser power was produced in the region of maximum positive glow potential. Figure 2.17 compares the current variation of output power for three isolated grid positions to that in the absence of the grids. As mentioned previously, maximum power occurred for the larger d_{GC} with an increase of at least a factor of two over that obtained with the grids removed. The output mode without the grids suggested that most of the power came from the vicinity of the anode, the anode glow.

Since the low current side of the peaks in the V-I characteristics of section 2.4.1 corresponded to glow attachment to the grid, it was desirable to operate above this region of instability. As the curves of Figure 2.17 indicate, and as will be shown in more detail later, the power maximum occurred on the high current slope of the V-I peak. Consequently, the maximum power occurred in a stable region where the positive column was uniformly spread over the grid with an intervening thin dark space. As indicated in Figure 2.17 a multimode output power in excess of 3W was obtained at a discharge current of 1A.

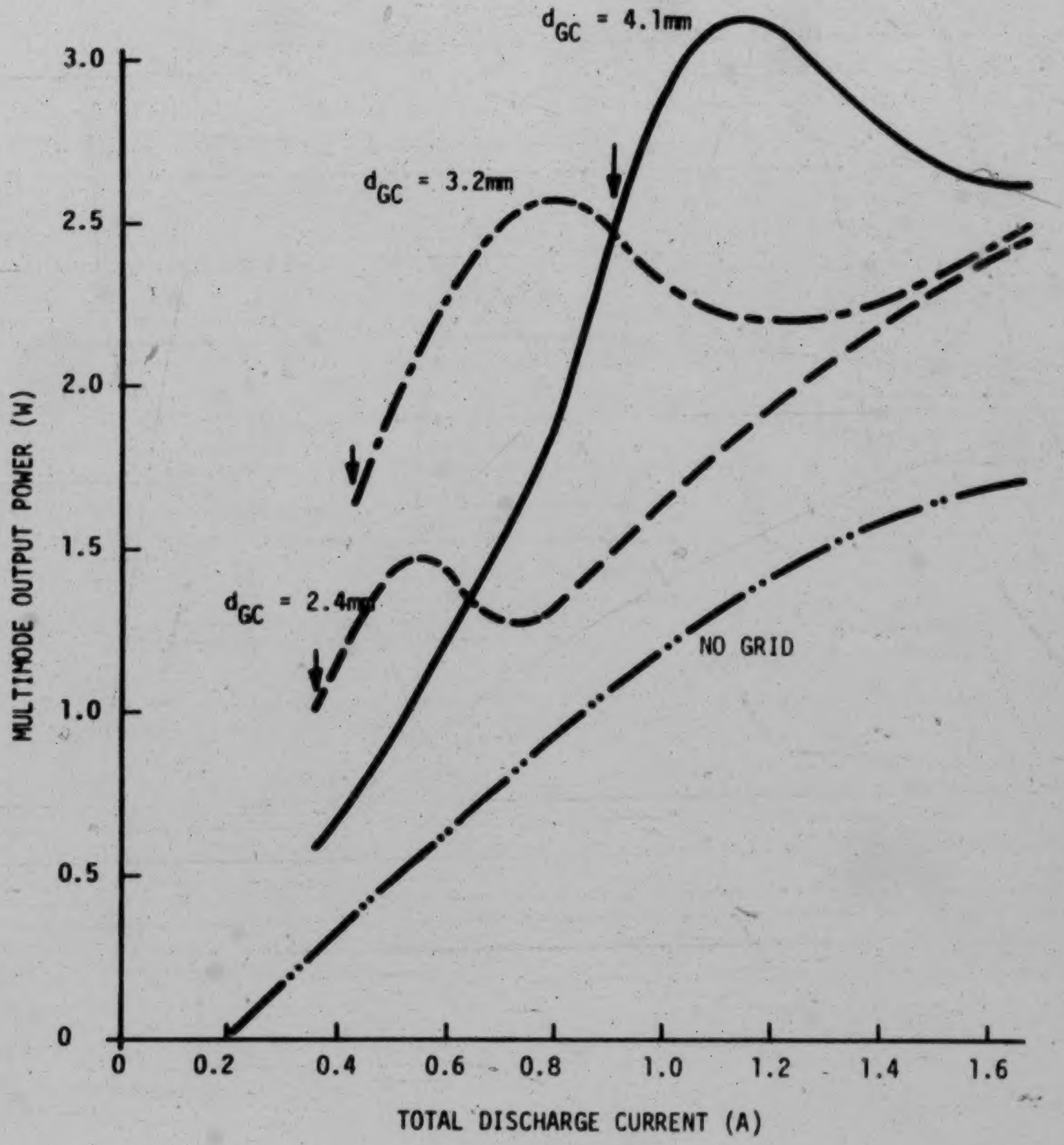

FIGURE 2.17. MULTIMODE OUTPUT POWER VERSUS TOTAL DISCHARGE CURRENT FOR VARIOUS ISOLATED GRID POSITIONS. $CO_2/N_2/He$ - 1.4/1.4/8.3mm; grid size, 16 meshes/inch; d_{AC}=2.9cm; flow rate, 6.4 liters/sec; arrows mark point of glow attachment to grid.

To extend the operating range and provide further ballast reduction, the self-biased grid was introduced. As explained in section 2.4.1 the positive glow column was stabilized over a larger current range. Figure 2.18 gives the power-current curves for varying bias resistance. R_2 (Figure 2.10) was maintained at 68KΩ while R_1 was varied from 20 to 32KΩ. The curve for a floating grid at the same d_{GC} is also shown. The corresponding V-I curves were presented in Figure 2.10, section 2.4.1(c). Essentially the same maximum power was obtainable with the biased as with the unbiased grid, however, lower ballast resistance was permitted; down to 500Ω in each cathode. This ballast resistance was sufficiently low that the power dissipated by the cathode fall potential was the major source of inefficiency. A certain amount of ballast was required for equalization of the cathode currents. A ballast of 500Ω seemed rather low for this purpose since the potential drop across the ballast was only a small fraction of that across the cathode fall. The explanation probably lies in the fact that the glow columns were more or less discrete entities. It was found later, Chapter 3, that placing the electrodes more closely, where all electrodes supplied a single diffuse positive glow, required increased ballast for current balance.

Efficiencies of the order of 0.5% were typical of the particular arrangement used to produce Figure 2.17 and 2.18. Note, however, that the resonator was coupled to approximately half the excited volume. A figure of 20% is typical of the more conventional tube laser. The main reason for the greatly reduced efficiency was the large cathode fall potential. In addition, the excited volume was small since the separation between adjacent glow columns was unnecessarily large.

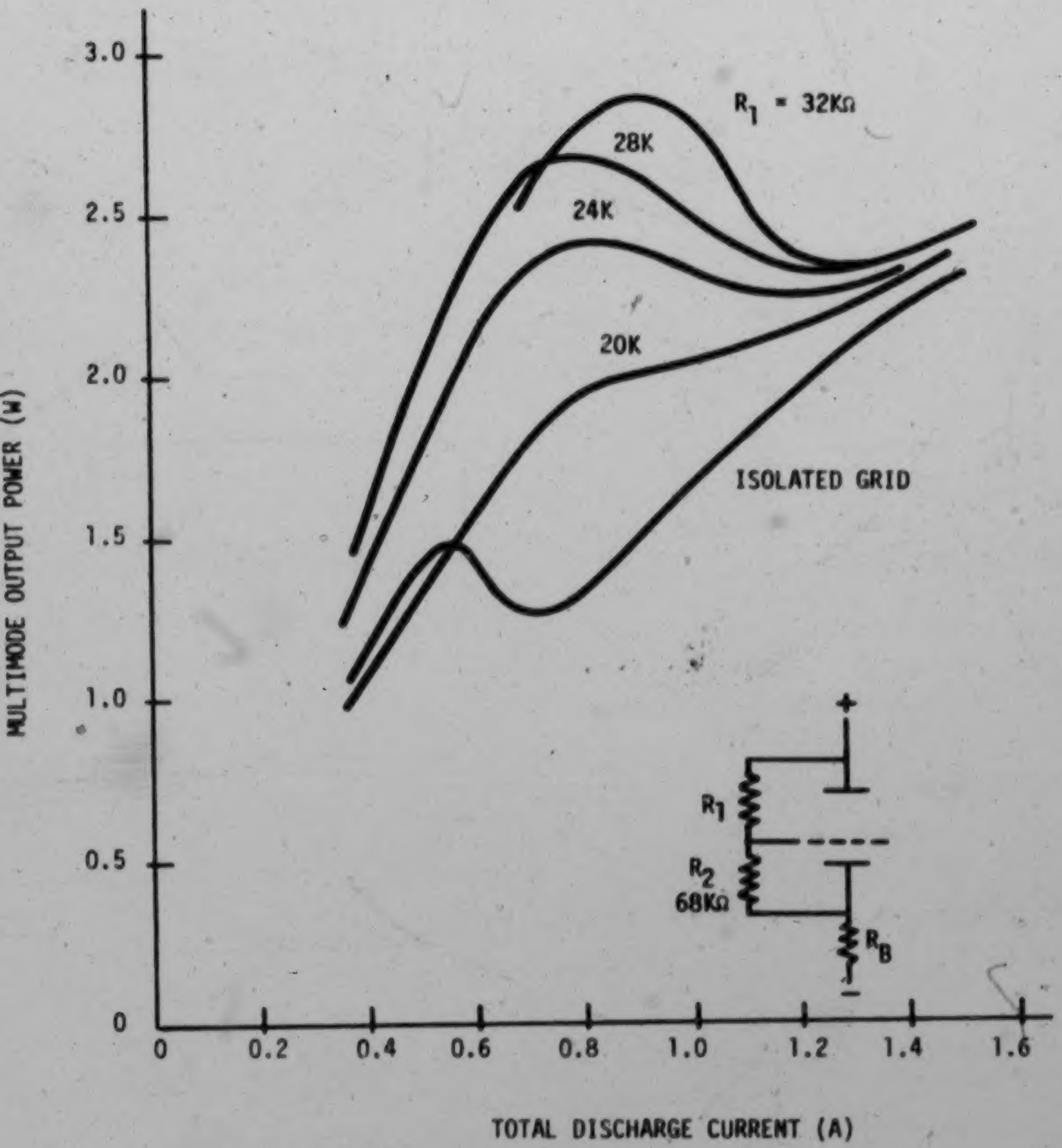

FIG. 2.18. MULTIMODE OUTPUT POWER FOR SELF-BIASED GRIDS. $CO_2/N_2/He$ - 1.4/1.4/8.3; BIASED GRIDS, 16 MESHES/INCH; d_{GC}, 2.4 mm; R_2, 68KΩ; FLOW RATE, 6.4 LITERS/SEC.

2.7 The Variation of Output Intensity with Flow Rate.

As mentioned previously considerable power is dissipated by the cathode fall. The resultant gas heating as expected varies with flow rate. Also, since the CO concentration is proportional to gas residence time [28][29], a change in gas constituents follows any change in the flow rate. The CO build-up has a visible manifestation in that the discharge takes on a bluish tint. In fact for discharge currents, say, at peak laser output, gas heating and CO build-up resulted in a gradual change of colour from an upstream pink to bluish pink at the exit. It is not surprising therefore to find that the discharge impedance decreased in the direction of gas flow. Any impedance increase due to CO [29] was overshadowed by the reduction of gas density due to heating.

Flow effects on output power are presented in Figure 2.19 for self-biased grids. Other than an obvious increase in power, Figure 2.19(a) shows that the power peak shifted, to higher discharge current with flow rate. Since all curves were run at constant d_{GC}, this was assumed to be caused by a change in the negative glow and cathode fall distances, as a result of gas density changes. As the flow rate increased convective cooling resulted in higher local gas density with an associated decrease in negative glow length. From Figure 2.19(b), which was constructed from the peak powers, a change of flow from 0.6 liters/sec. (0.5 volume changes/sec.) to 6.4 liters/sec (4 changes/sec) produced a factor of five increase in laser output. The above curves were taken at constant entrance-partial pressures, the particular fill corresponding to that for maximum output in the 5 to 6 liters/sec flow range. As pointed out by Smith [30] the optimum gas fill could

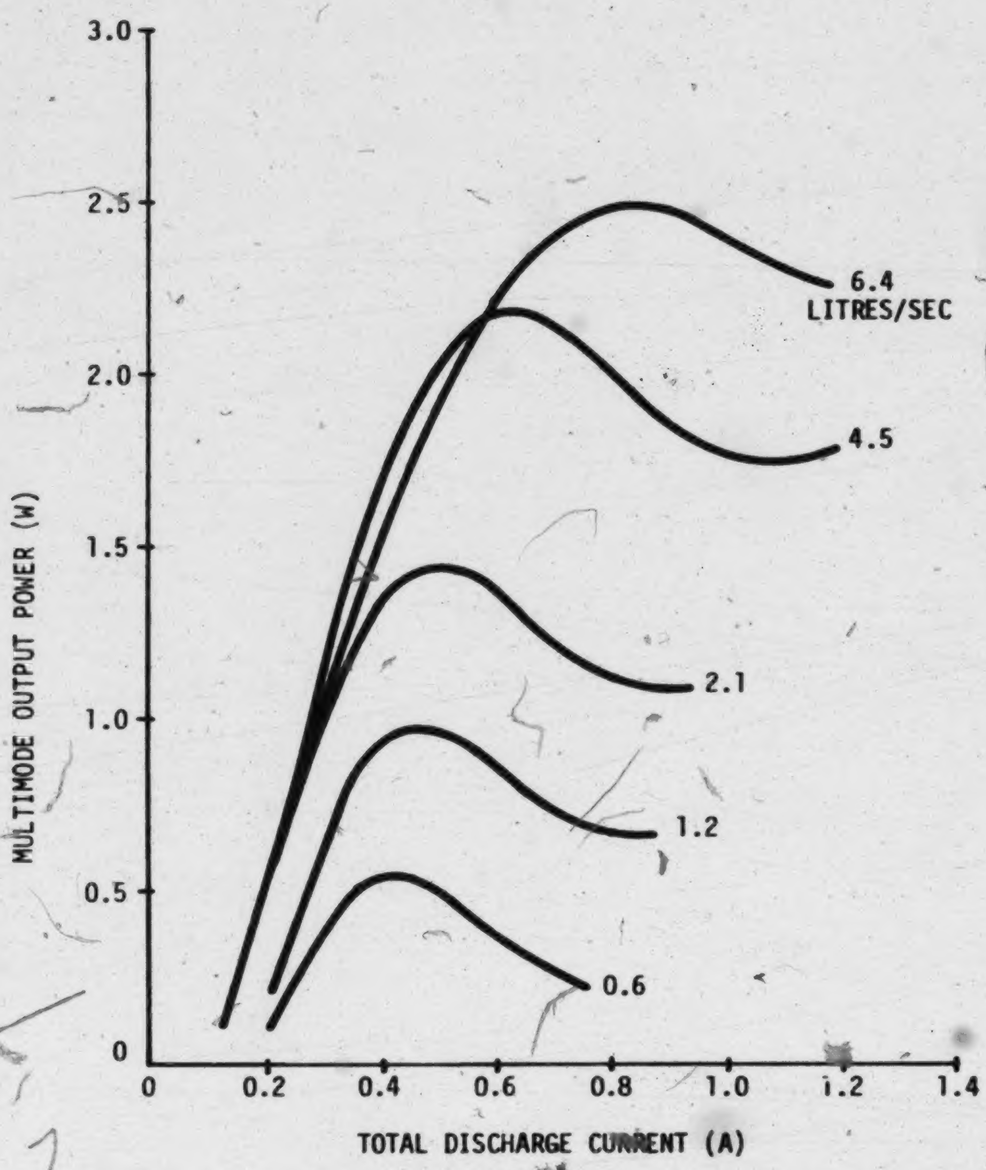

FIGURE 2.19(a). THE VARIATION OF OUTPUT POWER WITH TOTAL DISCHARGE CURRENT FOR VARIOUS FLOW RATES. $CO_2/N_2/He$ 1.4/1.4/8.3mm self-biased grids, R_1=28KΩ and R_2=68KΩ; grid size, 16 meshes/inch; d_{GC},2.4mm; d_{AC},2.9cm.

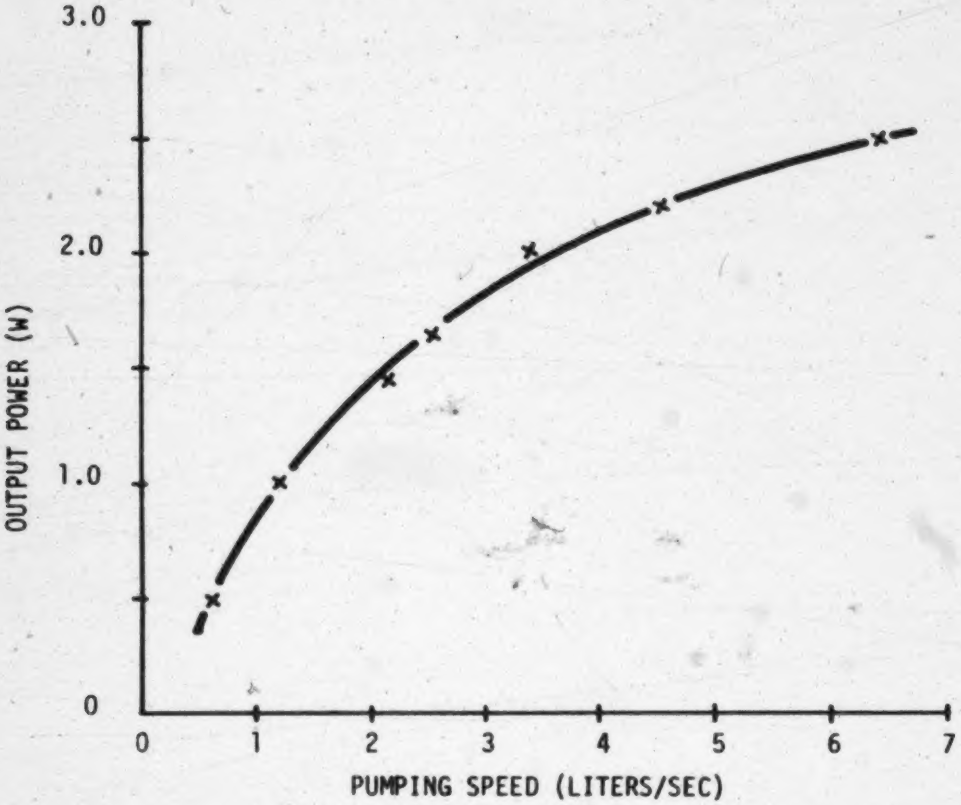

FIGURE 2.19(b). THE VARIATION OF OUTPUT POWER WITH FLOW RATE. The output power corresponds to the peak power for each flow rate. $CO_2/N_2/He$-1.4/1.4/8.3mm; grid size,16 meshes/inch; self-biased grids, R_1=28KΩ and R_2=68KΩ; d_{GC} = 2.4mm; d_{AC} = 2.9cm.

change with flow rate, because of a change in CO_2 dissociation. In the present experiments this seemed to be overshadowed by gas heating.

2.8 Measurements of Gas Temperature and Ion Saturation Current,

Spatial temperature and electron density scans were made by sweeping thermocouple and electrostatic probes through the positive column of one electrode pair as shown in Figure 2.20(a).

Since the (01^10) level of the CO_2 vibrational bending mode is only a few kT above the ground state (3.3kT at 17^oC), thermocouple scans gave an indication of the degree of thermal population of the lower laser level. As will be seen in the following section, 2.7, a monitor of the gas temperature with discharge current was also a fairly sensitive means of determining the maximum input power to the positive glow. In addition, for computations of E/N and thereby the average electron energy gas temperature was required for calculation of the neutral number density, N.

An electrostatic probe replaced the thermocouple for spatial scans of the ionization. The ion saturation current was collected at a probe bias of approximately 25V negative with respect to space potential. These radial scans gave an indication of the effective width of the positive columns and ambipolar diffusion gradients.

Typical spatial sweeps of gas temperature and ion saturation current are presented in Figure 2.20(b), for maximum input power to the positive glow for the experimental conditions of Table 2-1.

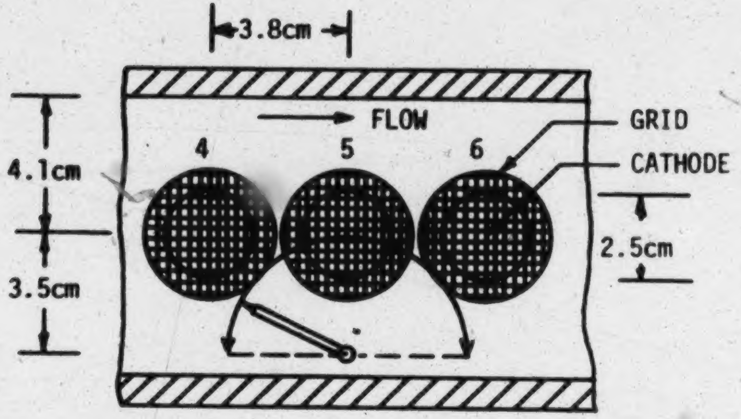
3.8cm
FLOW
4
5
6
GRID
CATHODE
4.1cm
3.5cm
2.5cm

FIGURE 2.20(a). SCHEMATIC OF THERMOCOUPLE AND ELECTROSTATIC PROBE SCANNING ARRANGEMENT. Radius of probe rotation 3.5cm; view from anode to cathode.

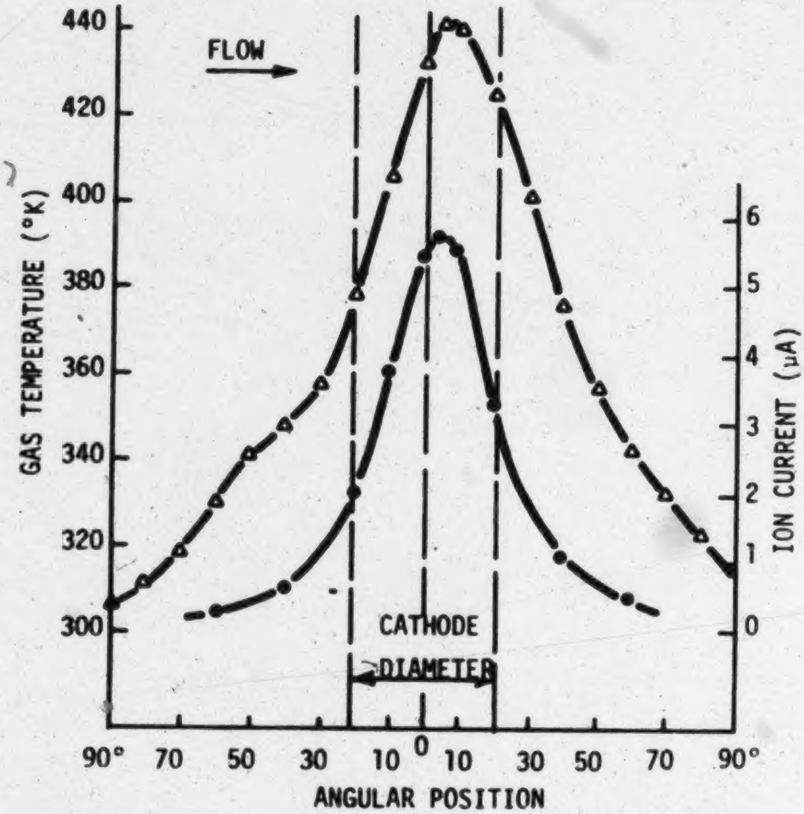

FIGURE 2.20(b). SPATIAL VARIATION OF GAS TEMPERATURE AND ELECTROSTATIC PROBE CURRENT OPERATING IN THE ION-SATURATION REGIME. Experimental conditions outlined in TABLE 2-1.

Table 2-1

Experimental Parameters for Typical

Thermocouple and Electrostatic Probe Scans of Figure 2.20

Single discharge current	-	90 mA, cathode no. 5, ≈ 20 cm from upstream edge of discharge.
Anode to cathode distance	-	d_{AC} = 2.9 cm.
Grid to cathode distance	-	d_{GC} = 2.4 mm.
Self-biased grid	-	R_1 = 28K; R_2 = 68K.
	-	16 meshes/inch
Gas Pressure	-	$CO_2/N_2/He$; 1.4/1.4/8.3 mm.
Gas Flow	-	6.4 liters/sec.
Anode width	-	1 cm.
Electrostatic probe	-	diameter, 0.1 mm.
	-	length of sensing tip, 3.2 mm.
	-	material, tungsten
	-	insulation, glass except for tip.
	-	radius of swing, 3.5 cm.
	-	plane of sweep midway between grid and anode.
	-	probe bias relative to floating potential, negative 25 V
Thermocouple probe	-	material, iron-constantan
	-	wire size, 0.25 mm.
	-	insulation, glass except for tip.
	-	radius of sweep, 3.5 cm.
	-	plane of sweep midway between grid and anode

From Figure 2.20(b) a slight downstream shift in the temperature and density profiles was introduced by the flow. The asymmetry in the temperature profile was also attributed to this shift. A temperature of approximately 440°K was obtained midway between the anode and grid with higher temperatures closer to the grid and lower closer to the anode. Severe thermal blockading is expected to occur in the 600 to 700°K range and temperatures of this order have been measured in conventional tube lasers [12] [29] [31] [32]. The calculations of Fowler show that even at 440°K and $N_e = 3 \times 10^{10}/cm^3$ the gain has dropped by a factor of 3 from that at room temperature [26]. The above temperature was measured approximately two-thirds the distance along the laser axis, therefore, just from temperature considerations alone, glow columns at the beginning of the axial flow were expected to contribute substantially more to the laser gain. This temperature gradient plus the composition changes discussed earlier clearly indicate the advantages of cross-flow as compared to axial flow.

A scan of ion saturation current indicated that significant ionization existed beyond the edge of the electrodes with a shallow gradient once the probe had passed beyond the edge of the visible glow. This low gradient supported the assumption that the lateral ambipolar diffusion loss was relatively low compared to that of a confined column. The electrons, however, thermalized in a few micro-seconds once out of the glow, so although significant ionization density existed beyond the electrodes its effective vibrational excitation was low [9].

The average electron density was estimated from a measured value of E/N, section 2.9, and a drift velocity, V_D, calculated in reference [12].

Electron density, N_e, at I_D = 90mA was calculated as follows:

$$E/N = 2 \times 10^{-16}\ \text{cm}^2\ \text{volt}$$

$$V_D \approx 5 \times 10^6\ \text{cm/sec.}$$

$$A = 4.9\ \text{cm}^2$$

$$N_e \approx \frac{I_D}{eV_DA} = 3.5 \times 10^{10}/\text{cm}^3$$

From the ion current profile a peak electron density of approximately $6 \times 10^{10}/\text{cm}^3$ was estimated. This calculation does not take into account the radial variation of both electron energy and drift velocity [12].

2.9 The Relationship of Maximum Laser Power to the V-I Characteristic

In this section the laser power maximum is related to the potential gradient across the positive column. From the positive glow potential and thermocouple temperatures E/N was calculated and an average electron energy estimated from the curves of Nighan [9] for the purpose of evaluating where the discharge may have been operating with respect to optimum vibrational excitation rates.

The experimental conditions are contained in Table 2-1 of the previous section. The corresponding V-I characteristic curve was presented previously in Figure 2.10 section 2.4. Upon comparing the V-I characteristic with Figure 2.21, the peak in laser power occurred on the stable high current side of the local V-I peak. This was verified by monitoring the gas temperature, also shown in

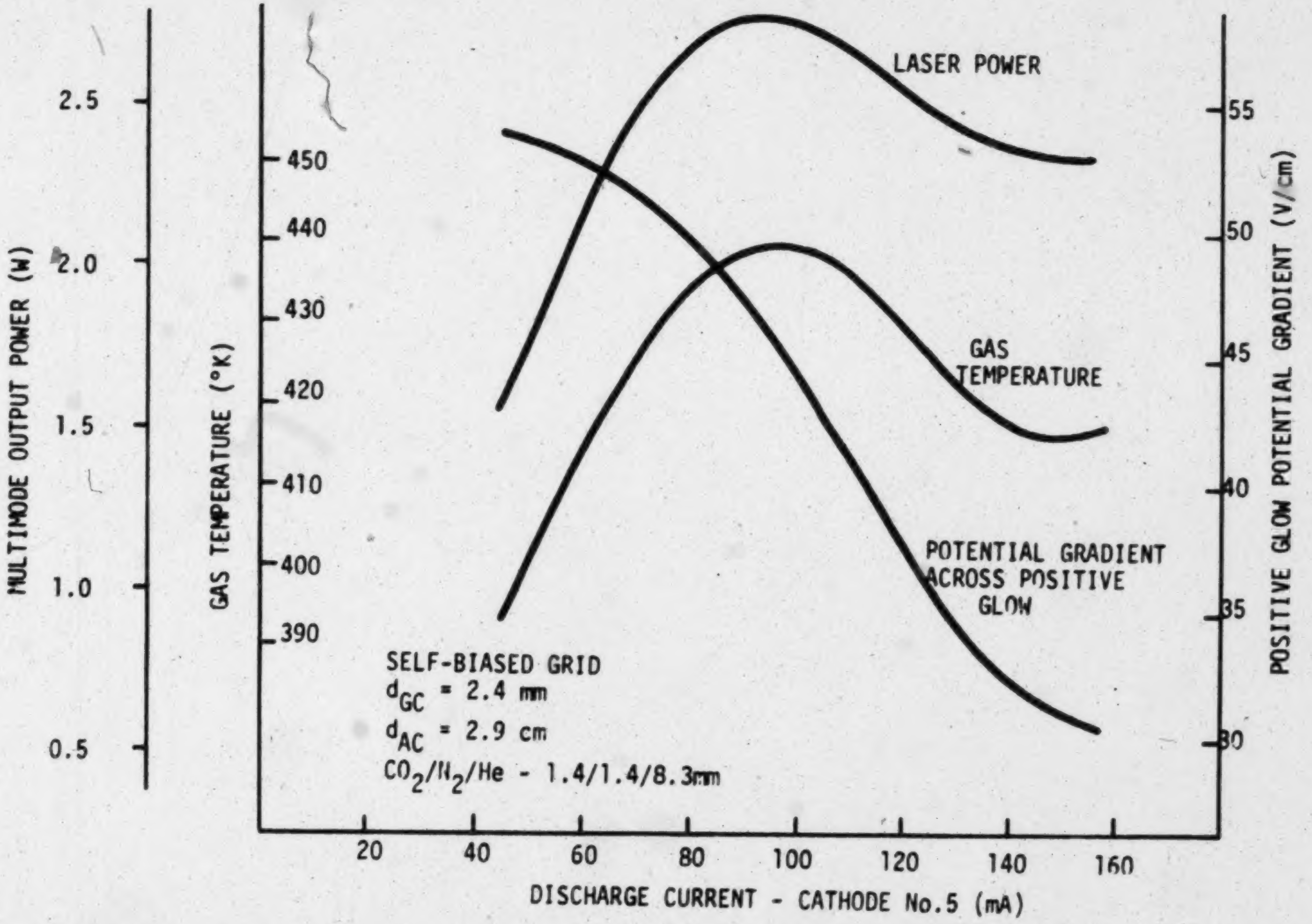

FIGURE 2.21. THE RELATIONSHIP OF LASER POWER, GAS TEMPERATURE, AND POSITIVE GLOW POTENTIAL WITH SINGLE ELECTRODE DISCHARGE CURRENT. THE EXPERIMENTAL CONDITIONS ARE THOSE OF TABLE 2-1, SECTION 2.8

Figure 2.21. The peak temperature coincided with peak laser power. Note that temperature was recorded under non-lasing conditions.

The reduced field E/N is presented for the above case, in Figure 2.22 from which E/N decreased from a value of 2.14×10^{-16} cm^2 volt at 60mA down to 1.25×10^{-16} cm^2 volt at 160mA. Below 60mA glow attachment to the grid had occurred while above 160mA the negative glow projected through the grid. In other words the grid had little control over the positive column potential once immersed in negative glow. A reduced average electron energy (2/3 of the average energy) was estimated from the curves of Nighan [9] and plotted as well on Figure 2.22. It appears that the grid was successful in raising the electron energy up to 1eV or greater with a subsequent significant increase in the vibrational excitation rate as verified by the laser output power.

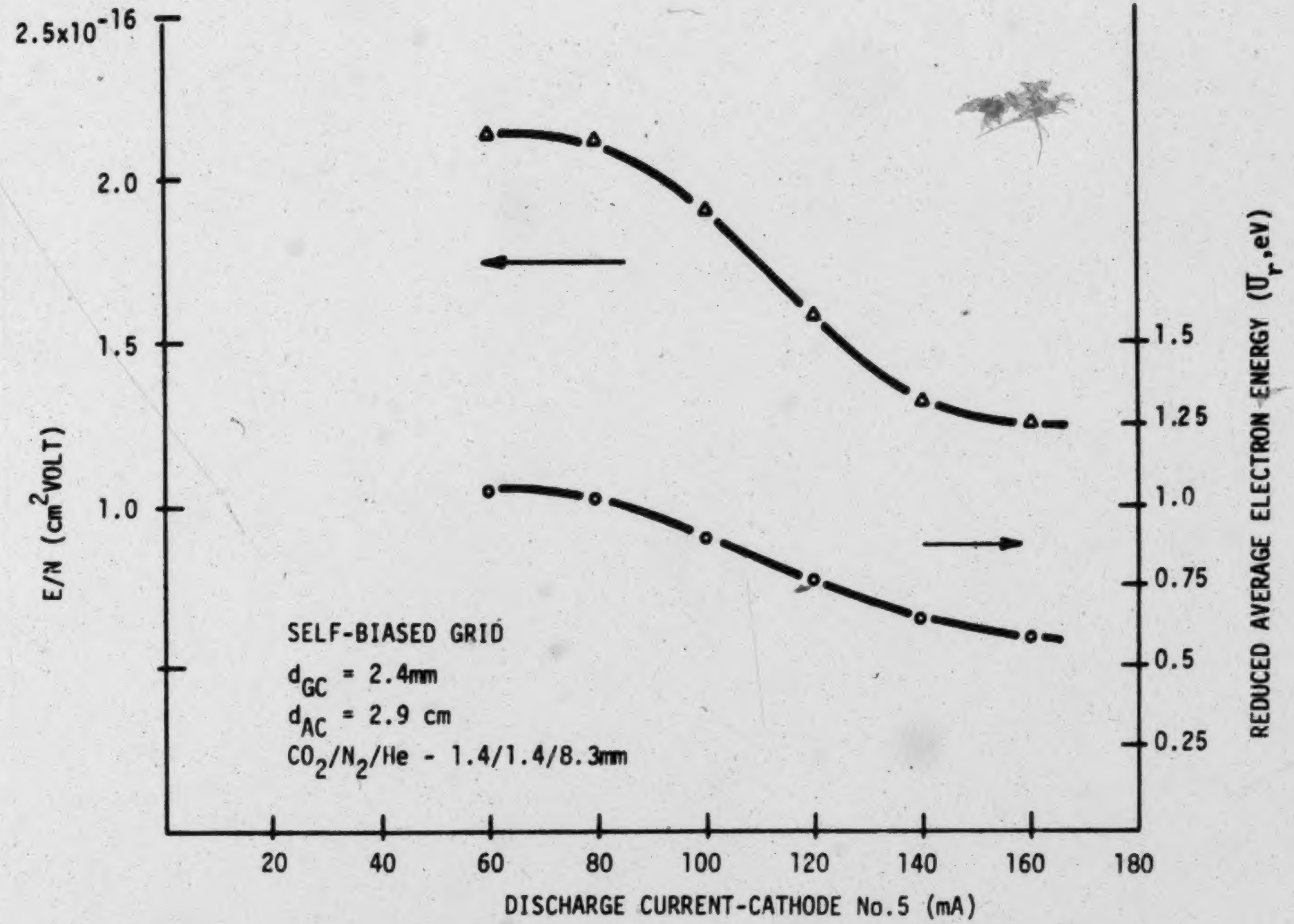

FIGURE 2.22. THE VARIATION OF THE REDUCED FIELD (E/N) AND REDUCED AVERAGE ELECTRON ENERGY ($\overline{U}_r$) WITH DISCHARGE CURRENT FOR CONSTANT d_{GC}. PUMPING SPEED, 6.4 LITERS/SEC; R_1 = 28K AND R_2 = 68KΩ; GRID SIZE, 16 MESHES/INCH.

2.10 Transverse Discharge with Low Velocity Cross-Flow

Since the obvious visible changes that occurred along an axial flow reflected changes in plasma impedance caused by CO generation and gas heating, axial flow was replaced by a low velocity transverse flow. This arrangement as reported by Sedgwick and Seguin [4] increased the column to column uniformity and even the low cross-flow velocities used here (<0.5m/sec) were effective in convecting the thermal energy from the laser region. This experimental arrangement led quite naturally to the high velocity cross-flow of Chapter 3. In view of this and the fact that electrode details were essentially those of previous sections of this chapter this arrangement is discussed only briefly. Figure 2.23 serves to illustrate the effectiveness of the cross-flow in raising the laser power. All curves were for discharges with isolated grids, with a grid to cathode separation of approximately 4mm. A significant increase in output power was observed, however, the discharge became unstable for the higher velocities (still less than 0.5m/sec) in that the positive glow was swept along to the edge of the grids. New electrode structures and higher velocity transverse flow are discussed in detail in Chapter 3.

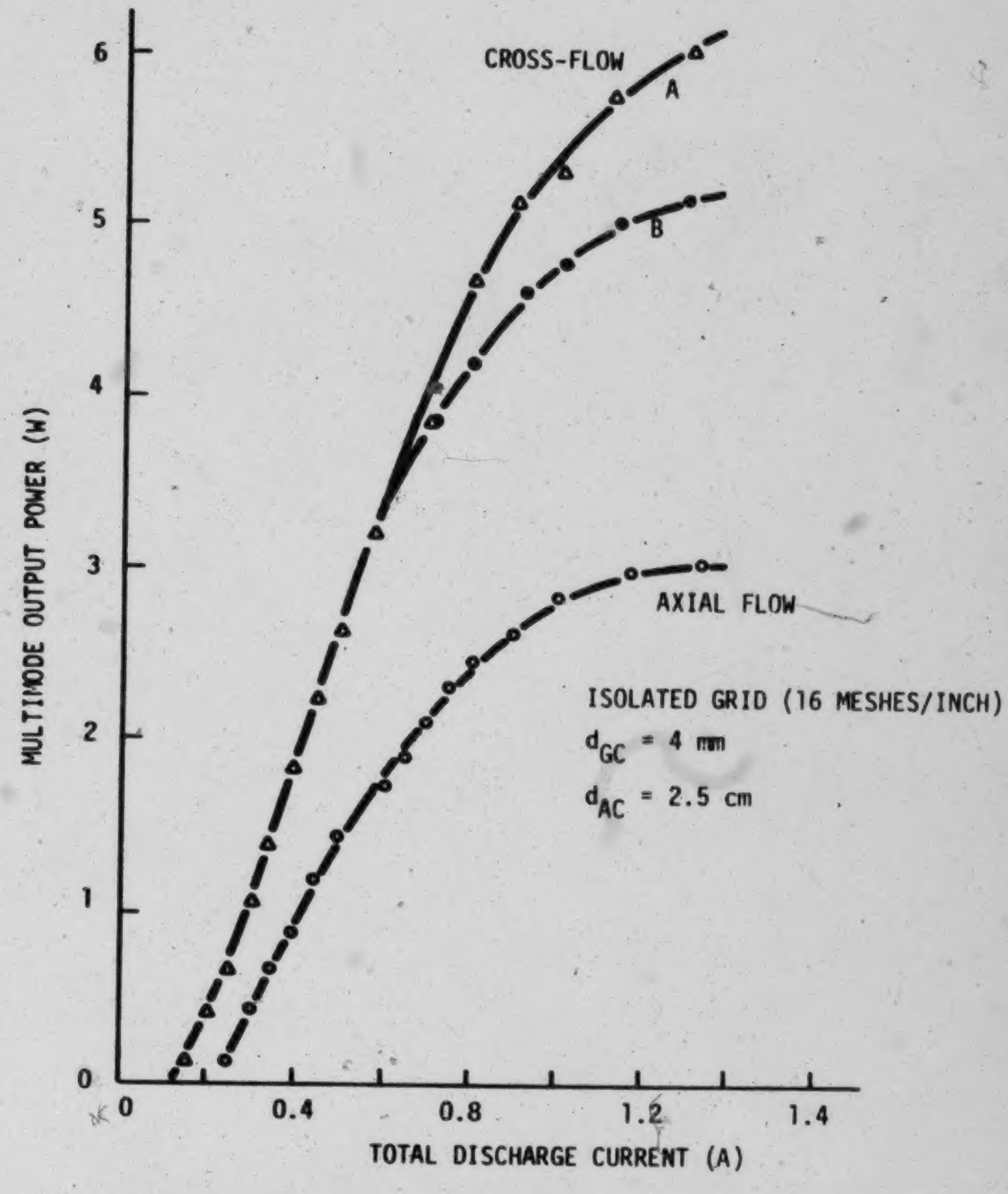

FIGURE 2.23. COMPARISON OF OUTPUT POWER VERSUS DISCHARGE CURRENT FOR AXIAL AND CROSS FLOWS.

AXIAL GAS FLOW: $CO_2/N_2/He$ - 1.2/1.3/8.4 mm;

8 LITERS/SEC.

CROSS FLOW: A, $CO_2/N_2/He$ - 1.6/1.5/7.9 mm;

11 LITERS/SEC.

B, 8 LITERS/SEC.

2.11 Summary

A transverse cold-cathode excitation geometry was examined as a means of reducing the high running potentials of the tube discharge. Excitation was established across the smallest dimension of a box laser, with the view that the active medium could be extended laterally without significant changes in discharge potential. Ideally large area electrodes are desired with uniform excitation along the full length of the laser. Experiments showed, however, that the large cathode fall potential and localized gas heating caused the discharge to degenerate into highly contracted arcs. Consequently, a segmented cathode structure was used with a continuous strip anode. By insertion of wire-mesh grids just above the cathodes, the low gain Faraday dark space was converted to a higher gain positive glow, section 2.4. The pumping density was more uniformly distributed across the anode-cathode volume providing at least double the output power, section 2.5. A summary of the characteristics of the box laser are given in Table 2.2 for low axial gas flow.

Table 2.2

Summary of Axial-Flow Box Laser

Anode dimension	- 1 x 38 cm, water cooled copper channel
Cathode	- 8 segments; 2.5 cm diameter, 3.8 cm between centers; water-cooled annular groove copper electrodes.
Grid	- 8 elements; 16 meshes/inch, 3.3 cm diameter; 68% open area.
Electrode to side-wall distance	- 4 cm from electrode center
Anode to cathode separation	- 2.9 cm.
Grid to cathode separation	= 2.5mm biased grid = 4mm isolated grid
Partial pressure	- CO_2/N_2/He-1.4/1.4/8.3 mm
Flow rate	- 6.4 liters/sec.
Discharge current and potential at maximum power	- typically 1A at 550V
Ballast resistance	- 2KΩ unbiased grid - 500Ω biased grid
Output power	- approximately 3W multi-mode (mode diameter approximately equal to one-half the excited height)
Efficiency	- approximately 0.5% for biased grid operation

A plasma-grid interaction model was set up in section 2.2 which qualitatively explained the operation of the triple electrode system. This model also seemed to be consistent with the experiments of Herceg and Miley [2] using a grid and thermionic cathode in a gas mixture of He and Ne. Briefly, the grid attenuated the diffusion dominated current of the Faraday dark space to such an extent that a higher electron energy, section 2.8, was required to maintain the discharge in the presence of ambipolar diffusion losses. As a consequence the Faraday dark space was replaced by a positive column of much higher power density.

The effects of changes of cathode to grid distances, mesh sizes, and biasing arrangements were examined in section 2.4. Both isolated and biased grids were effective in raising the gain. The biased grid (negative with respect to plasma space potential) extended the current range of stable positive columns. By virtue of a more gently sloping V-I characteristic the biased grid permitted a minimum of cathode ballast.

The discharge length was sufficiently short that the cathode fall potential was much larger than the drop across the positive column. This was the single most important factor responsible for the low efficiency. To reduce the fall potential, various cathode materials and geometries were studied, section 2.4.3. Of the materials tested aluminum provided the least cathode fall, however, this was offset by a relatively strong chemical reaction of the surface with the gas constituents. Copper was used to avoid this problem. By employing principles of the hollow cathode, geometries were designed and tested providing a reduction in V_C over the flat surface case.

The power dissipated in the cathode region still remained high, however.

The use of a thermionically emitting cathode may be one solution to cathode fall reduction. The potential drop expected from a thermionic cathode is approximately one-tenth that of a cold cathode. MacNair has given details of a thermionic electrode used in the oxidizing atmosphere of the CO_2 laser [33]. An emission current density of 1.8 A/cm^2 was obtained for a $BaZrO_3$ coated platinum filament at a temperature of $850^{\circ}C$. The emission efficiency was not given but it is assumed, from the performance of other oxide coated emitters, that the filament power required to replace the segmented structure of the box laser would be a small fraction of that dissipated in the potential fall of the cold cathode.

Finally the box laser was subjected to a low velocity cross-flow, section 2.10, with a factor of two increase in power. Thermal effects and CO_2 decomposition were reduced over the axial case, and column to column uniformity was greatly improved. For higher flow rates, however, the glow columns were swept to the edge of the grids. The improvement in power output by using convective flow led to a high velocity cross-flow structure which is discussed in Chapter 3.

REFERENCES

1. P.K. Tien, D. MacNair, and H. L. Hodges, "Electron Beam Excitation of Gas Laser Transitions and Measurements of Cross Sections of Excitation", Phys. Rev. Lett., Vol. 12, No. 1, p 30, January 1964.

2. J.E. Herceg and G. H. Miley, "A Laser Utilizing a Low-Voltage Arc Discharge in Helium-Neon", J. Appl. Phys., Vol. 39, No. 4, p. 2147, March 1968.

3. R.J. Freiberg and P.O. Clark, "CO_2 Transverse-Discharge Lasers", IEEE J. Quantum Electronics, Vol. QE-6, No. 2, p. 105, February 1970.

4. G. Sedgwick and H. Seguin, "Low Voltage CO_2 Laser Excitation", Appl. Optics, Vol. 9, No. 12, p. 2737, December 1970.

5. J.D. Cobine, "Gaseous Conductors", (Dover Publications, Inc., 1958), p. 134.

6. F.F.Chen, "Electric Probes", Plasma Diagnositic Techniques, edited by R.H. Huddlestone and S.L. Leonard (Academic Press, 1965) p. 113.

7. J.H. de Leeuw, "Electrostatic Plasma Probes", Physico-Chemical Diagnostics of Plasmas, Proc. Fifth Biennial Symposium on Gas Dynamics, p. 65.

8. G. Francis, "The Glow Discharge at Low Pressure," Handbuch der Physik, Vol. XX11, edited by S. Flugge (Springer-Verlag, 1956) p. 110.

9. W.L. Nighan, "Electron Energy Distributions and Collision Rates in Electrically Excited N_2, CO, and CO_2", Phys. Rev. A, Vol. 2, No. 5, p. 1989, November 1970.

10. A. von Engel, "Ionized Gases", (Oxford University Press, 1965), p.240.

11. C.S. Weller and M.A. Biondi, "Measurements of Dissociative Recombination of CO_2^+ Ions with Electrons", Phys. Rev. Lett., Vol. 19, No. 2, p. 59, July 1967.

12. A.J. Laderman and S.R. Byron, "Temperature Rise and Radial Profiles in CO_2 Lasers", J. Appl. Phys., Vol. 42, No. 8, p. 3138, July 1971.

13 R.H. Bullis, W.L. Nighan, M. C. Fowler, and W.J. Wiegand, "Physics of CO_2 Electric Discharge Lasers", AIAA Journal, Vol. 10, No. 4, p. 407, April 1972.

14. R.L. Gaver and H.J. Seguin, "High Quality Sputtered Multilayer Coatings for Infrared Laser Applications", Rev. Sci. Instruments, Vol. 41, No. 3, p. 427, March 1970.

15. Reference 8, p. 112.

16. A.K. Brewer and J.W. Westhaver, "The Cathode Region in the Glow Discharge", J. Appl. Phys., Vol. 8, No. 11, p. 779, November 1937.

17. Reference 8, p. 137.

18. Reference 8, p. 90

19. Reference 10, p.236

20. J.T. Maskrey and R.A. Dugdale, "The Role of Inclusions and Surface Contamination in Arc Initiation at Low Pressures", J.Appl. Phys., Vol. 17, No. 8, p. 1025, August 1966.

21. M.E. Fein, J.T. Verdeyen, and B.E. Cherrington, "A Thermally Pumped CO_2 Laser", Appl. Phys. Lett., Vol. 14, No. 11, p. 337, June 1969.

22. P.K. Cheo, "CO_2 Lasers", Lasers, Vol. 3 edited by A. K. Levine and A.J. DeMaria (Marcel Dekker, 1971), p. 209.

23. P.K. Cheo and H.G. Cooper, "Gain Characteristics of CO_2 Laser Amplifiers at 10.6 Microns", IEEE J. Quantum Electronics, Vol. QE-3, No. 2, p. 79, February 1967.

24. D.L. Franzen and R.J. Collins, "Radial Gain Profiles in CO_2 Laser Discharges", IEEE J. Quantum Electronics, Vol. QE-8, No. 4, April 1972.

25. M.C. Fowler, "Quantitative Analysis of the Dependence of CO_2 Laser Performance on Electric Discharge Properties", Appl. Phys. Lett., Vol. 18, No. 5, p. 175, March 1971.

26. W.J. Wiegand, M.C.Fowler, and J.A. Benda, "Influence of Discharge Properties on CO_2 Laser Gain", Appl. Phys. Lett., Vol. 18, No. 9, p. 365, May 1971.

27. R.L. Gaver and H.J. Seguin, "High Quality Sputtered Multilayer Coatings for Infrared Laser Applications", Rev. of Sci. Instr., Vol. 41, No. 3, p. 427, March 1970.

28. E.S. Gasilevich, V.A. Ivanov, E.N. Lotkova, V.N. Ochkin, N.N. Sobolev, and N.G. Yaroslavskii, "Carbon Dioxide Dissociation in a CO_2 Laser", Soviet Phys. - Technical Phys., Vol. 14, No. 1, p. 86, July, 1969.

29 W.J. Wiegand, M.C. Fowler, and J.A. Benda, "Carbon Monoxide Formation in CO_2 Lasers", Appl. Phys. Letts., Vol. 16, No. 6, p. 237, March 1970.

30. A.L.S. Smith, "Molecular Composition Changes in a Flowing CO_2-N_2-He-H_2O Laser", Brit. J. Appl. Phys. (J. Phys.D), Vol. 2, No. 2, p. 1129, 1969.

31. A.G. Sviridov, N.N. Sobolev, and G.G. Tselikov, "Plasma Gas Temperatures in the Discharges Used for CO_2 Lasers", JETP Lett., Vol.6, No. 3, p. 62, August 1967.

32 J.H. Waszink and J.A.J.M. van Vliet, "Measurements of the Gas Temperature in CO_2-N_2-He and CO_2-N_2-H_2O-He Discharges", J. Appl. Phys., Vol. 42, No. 9, p. 3374, August 1971.

33. D. MacNair, "Study of Electron Emitters for Use in Gas Lasers", IEEE J. Quantum Electronics, Vol. QE-5, No. 9, p. 460, September 1969.

CHAPTER 3

TRANSVERSE EXCITATION WITH HIGH VELOCITY CROSS-FLOW

3.1 Introduction

For slowly flowing axial systems, laser gain and output power are limited by the conduction of heat to the walls [1] [2] [3]. Center-line translational temperatures at maximum laser power can reach from 600 to 800°K [4] [5] [6] [7]. At this temperature the laser process is seriously blockaded. For axial flow systems additions of He are particularly effective for gas cooling [4] since the thermal conductivity of He is much greater than either CO_2 or N_2 [6].

Laderman and Byron [6] presented an analytical model for slow axial flow in a cylindrical discharge tube. For an input power of approximately 4.5W per cm of length, a center-line to wall temperature difference of 400°C was calculated for a gas composition of 5% CO_2, 15% N_2 and 80% He. This compared favourably with experiment. For a wall surface maintained near room temperature this corresponds to maximum output power from the laser.

The stagnation temperature differential, ΔTo, due to convective cross-flow can be estimated from the following relation for heat addition to an insulated channel.

$$\Delta T_o = \frac{QW}{c_p \rho UA} = \frac{Q}{c_p \rho UH} \qquad . . . (3.1)$$

Q = input power per unit width of channel, W.

c_p = specific heat of gas mixture

ρ = density of gas mixture

U = flow velocity

A = cross-sectional area of channel

= H x W

H = height of channel

From the above equation it is seen that for purely convective heat removal, the temperature rise is inversely proportional to the mass flow rate, ρUA. The center-line temperature, for a slow-flow cylindrical tube, however, is independent of the flow rate. In addition, as shown in reference [6] the centerline temperature is independent of diameter for a fixed input power per unit length of axial flow.

From equation (3.1), for an insulated channel (H=3.8 cm as used experimentally in this chapter) with the above gas mixture and input power, and assuming a gas pressure of 20mm, ΔT_o across the zone of heat addition is less than 400°C for cross-flow velocities, $U \geq 1$m/sec. Consequently even for low cross-flow, convection becomes the dominant mechanism of heat removal. This low velocity is consistent with Chapter 2, section 2.9 where transverse velocities less than 0.5m/sec produced a significant increase in output power.

Assuming a velocity of 40m/sec, typical of those used experimentally, and ΔT_o = 400°C, Q becomes 160W/cm. In other words, the input power has been increased by a factor of approximately 35 to produce the same temperature differential as the axial case. This represents a rather large increase in volumetric efficiency.

For the sake of comparison, even a relatively short longitudinal discharge, say 25 cm, cooled by convection requires high flow velocities. For instance a tube of diameter 3.8 cm (equal to the above channel height) and an input power of 160W/cm of length, requires U>335m/sec (near sonic speed) for $\Delta T_o < 400^oC$.

The first use of transverse gas flow for removing laser waste energy was by Wilson [8]. In this case a lower laser level with long life-time, was removed by supersonic cross-flow in a pulsed N_2 laser. Initial publication of cross-flow applied to the CO_2-N_2-He laser was made by Tiffany, Targ and Foster [9]. By employing a flow rate of 30m/sec and a discharge length of one meter, CW output powers in the range of one kilowatt were obtained. This represented an order of magnitude improvement in volumetric efficiency over low flow axial systems. Another advantage was the use of closed cycle flow offering considerable gas economy.

The effectiveness of high mass flow in a short longitudinal system was demonstrated by Cool and Shirley [10] and Deutsch et al [11]. Note that in these experiments flow velocities of several hundred meters per second were employed as compared to 30m/sec for the cross-flow system.

Several schemes have been employed to couple the electrical energy to the gas. A long positive column subjected to a cross-flow is swept or bowed downstream out of the resonator. Buczek et al [12] stabilized the discharge with a small magnetic field. A short transverse electrode geometry was demonstrated by Sedgwick and Seguin [13] which was stable against the viscous force of the flowing gas. This multiple pin arrangement did not require auxiliary stabilization.

An electric discharge mixing laser with convective heat removal was demonstrated by Brown [14]. An electric discharge in N_2-He was formed upstream of the zone of cold CO_2 addition. After a short mixing distance the mixture flowed through the resonator.

Hill [15] applied high velocity flow to a large volume discharge, a 426 cm^2 area channel extending 100 cm in the flow direction. The electrical discharge was formed in the direction of near sonic flow using aerodynamic techniques for stabilization. Used as an amplifier with 17 traversals of the active medium an output power of 20KW was obtained.

A similar high power amplifier constructed by Brown and Davis [16] gave up to 30KW of output power. The channel in this case was a 1550 cm^2 area extending 53 cm in the direction of flow. By using this much larger cross-sectional area than that of reference [15] above, the flow velocities were correspondingly reduced for a given mass flow.

This chapter is largely concerned with the coupling of high power densities to the gas flow to form a stable uniform active medium. Excitation schemes investigated, were consistently of the transverse type, orthogonal to both the gas flow and the resonator axes. This approach creates a short low voltage, high current discharge.

As was discussed in Chapter 2 the effects of cathode fall potential assume a much more dominant role for transverse as compared to longitudinal excitation. This was in fact the main cause of low efficiency in the previously discussed slow-flow experiments. It is shown in section 3.9 that subjecting the electrical discharge to higher, cross-flow, velocities increased the electrical conversion efficiency by an order of magnitude. The goal is a uniformly excited active medium of high electrical conversion efficiency coupled with high output power per unit volume.

3.2 Theoretical Analysis of the Cross-Flow Laser System

3.2.1 *Introduction*

Energy balance equations similar to those of Gordietz et al [17] were coupled with gas dynamic equations [18] to calculate the small-signal gain and output power of an electric discharge cross-flow laser system. Reference [17] found good qualitative agreement with experimental results. Since then, this approach has been used by Witteman [19], Tulip [20] and Fowler [21] among others, giving much closer agreement with experiment. Compared to the usual rate equations, this approach employs a reduced number of equations coupling vibrational modes rather than vibrational levels.

The model is based on the Landau-Teller equation, derived using a harmonic oscillator approximation to the levels of a vibrational mode [22].

$$\frac{de}{dt} = \frac{e^{*}(T) - e}{\tau(T,p)} \qquad \ldots (3.2)$$

The instantaneous specific energy of the vibrational mode, e, relaxes toward e^{*}, the equilibrium energy at translational temperature, T. The relaxation time, τ, is in general a function of time since the translational temperature and pressure vary through the electrical discharge. The parameter, τ, is then referred to as the local relaxation time. Theoretical relationships for times in CO_2, derived by Schwartz et al [23] and Witteman [24], have been combined with experimentally measured relaxation and transfer data for the $CO_2/N_2/He$ gas mixture. Equation (3.2) does not specify the non-equilibrium distribution of oscillators [22]. In reference [17], however, a Boltzmann distribution was assumed during the relaxation process. This requires that the vibrational exchange among the levels of a mode is more rapid than the excitation rate, and the transfer to other vibrational modes and translation. Experiments suggest that the thermalizing time is rapid [25]. Consequently, a Boltzmann distribution was assumed for the levels of each vibrational mode in the present analysis.

3.2.2 *Energy balance equations*

Energy transfer processes were previously discussed in Chapter 1, section 1.3. The following energy balance equations incorporate the significant processes for a $CO_2/CO/O_2/N_2/He$ mixture where CO and O_2 appear by way of dissociation of CO_2. These equations are similar to those used by Tulip [20] with terms added to account for deactivation by electrons.

CO_2 Bending mode

$$u\frac{de_2}{dz} = EXC_2 - \frac{e_1^*(T_2) - e_1}{\tau_{12}} + \frac{e_2^*(T) - e_2}{\tau_{20}} - \frac{hf_2}{hf_3}\,\frac{e_3^*(T,T_1,T_2) - e_3}{\tau_3} \qquad \ldots (3.3)$$

CO_2 Symmetric stretch mode

$$u\frac{de_1}{dz} = EXC_1 + \frac{e_1^*(T_2) - e_1}{\tau_{12}} - \frac{hf_1}{hf_3}\,\frac{e_3^*(T,T_1,T_2) - e_3}{\tau_3} + \frac{hf_1}{hf_L}\,\Delta NX_R I_c \qquad \ldots (3.4)$$

CO_2 Asymmetric stretch mode

$$u\frac{de_3}{dz} = EXC_3 + \frac{e_3^*(T,T_1,T_2) - e_3}{\tau_3} - \frac{e_4^*(T_3) - e_4}{\tau_{43}} - \frac{hf_3}{hf_L}\,\Delta NX_R I_c \qquad \ldots (3.5)$$

N_2 Vibrational mode

$$u\frac{de_4}{dz} = EXC_4 + \frac{e_4^*(T_3) - e_4}{\tau_{43}} \qquad \ldots (3.6)$$

CO Vibrational mode

$$u\frac{de_5}{dz} = EXC_5 + \frac{e_5^*(T_3) - e_5}{\tau_{53}} \qquad \ldots (3.7)$$

The following list explains the various terms used in equations (3.3) to (3.7)

e_i = instantaneous specific energy (joules/unit mass) where $i = 1\text{-}5$

i = 1-CO_2 symmetric stretch vibrational mode; 2-CO_2 bending mode; 3-CO_2 asymmetric stretch mode; 4-N_2 vibrations; 5-CO vibrations

z = distance in direction of flow

hf_i = energy quantum of each mode

hf_L = energy quantum of the laser radiation

T_i = vibrational temperature associated with each mode

θ_i = hf_i/k, characteristic temperature of each mode

k = Boltzmann's constant

T = translational temperature

N_s = neutral number density (per unit mass) where s refers to the gas constituents

u = gas flow velocity

N_e = electron number density per cm^3

EXC_i = $N_e hf_i(N_s K_{oi} - N_i K_{io})$, electron energy transfer to and from the vibrational modes

K_{oi} = effective electron vibrational excitation rate (cm^3/sec)

K_{io} = effective electron vibrational deactivation rate (cm^3/sec)

$N_{i\neq 2} = hf_i N_s \exp(-\theta_i/T_i)$, number density (per unit mass) of each vibrational mode

$N_2 = 2hf_2 N_{CO_2} \exp(-\theta_2/T_2)$

$$e_{i\neq 2} = \frac{N_s hf_i}{\exp(\theta_i/T_i) - 1},$$ instantaneous specific energy of each vibrational mode

$$e_2 = \frac{2N_{CO_2} hf_2}{\exp(\theta_2/T_2) - 1},$$ instantaneous specific of CO_2 bending mode

$$e_2^*(T) = \frac{2N_{CO_2} hf_2}{\exp(\theta_2/T) - 1},$$ equilibrium value of e_2 at translational temperature ,T

$$e_1^*(T_2) = \frac{N_{CO_2} hf_1}{\exp(\theta_1/T_2) - 1},$$ equilibrium e_1 at vibrational temperature of bending mode, T_2

$$e_3^*(T,T_1,T_2) = \frac{N_{CO_2} hf_3}{\exp\left(\frac{\theta_1}{T_1} + \frac{\theta_2}{T_2} + \frac{\theta_3 - \theta_2 - \theta_1}{T}\right) - 1},$$ equilibrium e_3 at vibrational temperatures T_1 and T_2 and translational temperature ,T

$$e_4^*(T_3) = \frac{N_{N_2} hf_4}{\exp(\theta_4/T_3) - 1},$$ equilibrium e_4 at temperature of CO_2 asymmetric mode, T_3

$e_5^*(T_3) = \dfrac{N_{CO}hf_5}{\exp(\theta_5/T_3) - 1}$, equilibrium e_5 at T_3.

$\tau_{20}^{-1}(s) = k_{20s}\,(1 - \exp(-\theta_2/T))$, the inverse of the local relaxation time coupling the bending mode to translation where k_{20s} is the downward rate (number per sec) from the (01'0) level of the bending mode, for each collision partner, s [22].

$\tau_{20}^{-1} = \sum_s \psi_s \tau_{20}^{-1}(s)$, inverse of the total relaxation time where ψ_s are the mole fractions of the various collision partners.

$\tau_{12}^{-1}(s) = \dfrac{N_s P_{12}(\exp(\theta_2/T_2) + 1)}{\exp(\theta_2/T_2) - 1)}$, inverse relaxation time coupling bending and symmetric modes where P_{12} contains the transition probabilities [24].

$\tau_3^{-1}(s) = \dfrac{N_s P_3 \left(\exp \dfrac{\theta_1}{T_1} + \dfrac{\theta_2}{T_2} + \dfrac{\theta_3 - \theta_2 - \theta_1}{T}\right) - 1}{(\exp(\theta_1/T_1) - 1)(\exp(\theta_2/T_2) - 1)}$, inverse relaxation time coupling asymmetric to symmetric and bending modes [24].

τ_{43} = resonant transfer time between the CO_2 asymmetric mode and the vibrational mode of N_2 [26].

τ_{53} = resonant transfer time between CO and CO_2 [26].

ΔN = population inversion density (per unit mass)

X_R = stimulated emission cross-section (cm^2)

I_c = intensity of intra-cavity radiation field (W/cm^2)

The energy balance equations (3.3) to (3.7) were simplified by the following assumptions:

(1) The N_2 and CO vibrations were in equilibrium with the CO_2 asymmetric mode and therefore, describable by a common vibrational temperature, T_3. This is based on fast resonant transfer times τ_{43} and τ_{53} as discussed in Chapter 1, section 1.3.1.

(2) The relaxation time τ_{12} was rapid due to Fermi-resonance as discussed in Chapter 1, section 1.3.2. Consequently, the symmetric stretch and bending modes were assumed in equilibrium at vibrational temperature T_2. This may not be valid for high stimulated emission rates. Recent experiments raise some doubt as to the rate determining process in the relaxation of the lower laser level to translation [27].

(3) The relaxation time of the asymmetric mode, τ_3, was based on experimental data and as such corresponded to the case of $T_2=T_1=T$. This implies condition (2) plus fast relaxation of the bending mode to translation, maintaining T_2 near the gas temperature, T. Here again, the approximation may be justified only for computations of small-signal gain, that is, low radiation intensities. The error introduced is, however, offset by the fact that collisional relaxation becomes less significant in the presence of a high stimulated emission rate.

Incorporating the above approximations leads to the following equations for vibrational non-equilibrium.

(a) Equations (3.3) and (3.4), for the bending and symmetric stretch modes reduce to

$$u \frac{de_{12}}{dz} = EXC_{12} + \frac{e_2^*(T) - e_2}{\tau_{20}} - \left[\left(1 - \frac{hf_1 + hf_2}{hf_3}\right) \frac{e_3^*(T,T_2) - e_3}{\tau_3}\right] + \frac{hf_1}{hf_L} \Delta N \, X_R \, I_c \qquad \ldots (3.8)$$

$$e_{12} = e_1 + e_2$$

$$EXC_{12} = EXC_1 + EXC_2$$

(b) Equations (3.5), (3.6), and (3.7) combine to form the following energy balance equation for the CO_2 asymmetric, the N_2, and the CO vibrational modes.

$$u \frac{de_{345}}{dz} = EXC_{345} + \frac{e_3^*(T,T_2) - e_3}{\tau_3} - \frac{hf_3}{hf_L} \Delta N \, X_R \, I_c \qquad ...(3.9)$$

$$e_{345} = e_3 + e_4 + e_5$$

$$EXC_{345} = EXC_3 + EXC_4 + EXC_5$$

Experimental data were used to compute the relaxation times as a function of gas pressure and temperature. Rate data are extensively reviewed by Taylor and Bitterman [28] and Cheo [26]. The time, τ_{20}, for relaxation of the CO_2 bending mode to translation was calculated by incorporating the exothermic rates of reference [28] into the following expression [22],

$$\tau_{20}^{-1} = (1 - \exp(-\theta_2/T)) \sum_s N \rho \, \psi_s \, k_{2f}^s(T) \qquad ...(3.10)$$

where ρ is the mass density of the gas mixture; N, the total neutral number density per unit mass; $k_{2f}^s(T)$, the normalized rate (cm^3/sec) for the (01^10) level of the bending mode to translation; and the other symbols as previously defined. The temperature dependence of $k_{2f}^s(T)$

was taken from reference [28] and represented in functional form by

$$k_{2f}^{s}(T) = k_{2f}^{s}(T_o) \exp\left(2.3\xi_s \Delta(T^{-1/3})\right) \qquad \ldots (3.11)$$

$k_{2f}^{s}(T_o)$ = exothermic rate at temperature $T_0 = 300^\circ K$

ξ_s = slope of log k_{2f}^{s} versus $T^{-1/3}$

$\Delta(T^{-1/3}) = T^{-1/3} - T_o^{-1/3}$

In the computations, equation (3.11) was simplified by assigning a single temperature dependence, that of the most effective rate, since most of the curves have similar slope.

The relaxation time, τ_3, of the CO_2 asymmetric mode was also calculated from experimental data. The temperature dependence was again simplified to that of the most effective species. For the temperature variation a curve was fitted to the data of Rosser et al [29] for CO_2 - CO_2 collisions [30]. The analytical form of the relaxation time was given by

$$\tau_3^{-1} = 1.47 \times 10^{-27} \frac{N_o \rho}{M} T^{4.75} \exp(748/T) \sum_s \psi_s \frac{k_{s-CO_2}}{k_{CO_2-CO_2}} \qquad \ldots (3.12)$$

N_0 = Avogadro's number

M = molecular weight of gas mixture

The rates used in the calculations of this chapter are presented in Table 3.1 along with the source of the data.

Table 3.1

CO_2 Vibrational Relaxation Rate Coefficients

T = 300°K

Collision partner, M_s	Rate coefficient (cm^3/sec)			
	Process 1	Reference	Process 2	Reference
CO_2	6×10^{-15}	[28]	10.3×10^{-15}	[31],[32],[29]
N_2	1	[28]	3.4	[31],[32],[29]
CO	775	[26]	7.6	[33]
O_2	1	[28]	3.4	[34]
He	100	[28]	2.6	[31],[32],[34]

Process 1: $CO_2(01^10) + M_s \rightarrow CO_2(00^00) + M_s + 667cm^{-1}$

2: $CO_2(\nu_3) + M_s \rightarrow CO_2(\nu_1\nu_2) + M_s + \Delta E$

Calculated effective electron excitation rates are listed in Table 3.2 [35]. An experimental estimate of electron deactivation is also given [36].

Table 3.2

Effective Electron Excitation Rates [35] at 2ev.

K_{012}; indirect $CO_2(n00\text{-}0m0)$ = 3×10^{-8} cm^3/sec

K_{02} ; direct $CO_2(01^10)$ = 5×10^{-9}

K_{03} ; $CO_2(00^0n)$ = 6×10^{-9}

K_{04} ; $N_2(\nu=1\text{-}8)$ = 2×10^{-8}

K_{05} ; $CO(\nu=1\text{-}8)$ = 3×10^{-8}

Effective electron deactivation rates [36]

K_{30} ≃ 1×10^{-6} cm^3/sec

K_{10} ≃ 3×10^{-6}

The previous paragraphs outlined the energy balance equations and various simplifying approximations. The rate coefficients for vibrational relaxation via collisions with neutrals and rates for electron excitation and deactivation are listed in Tables 3.1 and 3.2 respectively. An equation relating the radiation field to the population inversion is now presented.

3.2.3 *Cavity radiation intensity equations*

An equation describing the build-up of the radiation field, I_c, with time is given by [37],

$$\frac{dI_c}{dt} + \frac{I_c}{\tau_c} = c\chi_R I_c \frac{\Delta N_T}{V} \qquad \ldots (3.13)$$

where τ_c is the cavity photon lifetime; ΔN_T, the total population inversion contained within the resonator mode volume, V; and X_R, the stimulated emission cross-section. It was assumed that each elemental pumping volume coupled to the whole field and that the cavity intensity was uniform over the mode volume. This was approximated by the high-order mode structures observed for the cross-flow laser equipped with a stable resonator.

The total population inversion is represented by the integral of the specific inversion over the mode dimension, d, in the direction of flow.

$$\Delta N_T = L_a \int_0^d \Delta N(z)\ \rho(z)\ dz \qquad \ldots (3.14)$$

ΔN is the specific inversion density (per unit mass); ρ, the mass density; and L_a, the length of active medium parallel to the resonator axis.

Considering the steady-state, equation (3.13) reduces to

$$\frac{1}{\tau_c} = cX_R \frac{\Delta N_T}{V} \qquad \ldots (3.15)$$

The threshold gain, $X_R \Delta N_T/V$, is dictated by the photon lifetime, τ_c,

$$\tau_c \simeq -\frac{2L}{c\ell nR} \qquad \ldots (3.16)$$

where R is the reflectivity of the output mirror and L, the resonator length.

The specific inversion density, ΔN, is defined by

$$\Delta N = N_{00^01} - \frac{\theta_J P(J+1)}{\theta_{J+1} P(J)} N_{10^00} \qquad \ldots (3.17)$$

where N_{00^01} and N_{10^00} are the population densities of the (00^01) and (10^00) levels of the CO_2 asymmetric and symmetric stretch modes respectively; P(J) and P(J+1) the rotational distribution functions of the asymmetric and symmetric modes [38]; and θ_J and θ_{J+1}, the multiplicity of the upper and lower rotational levels.

$$N_{00^01} = \frac{N_{CO_2} \exp(-\theta_3/T_3)}{Q_1 Q_2^2 Q_3}$$

$$N_{10^00} = \frac{N_{CO_2} \exp(-\theta_1/T_1)}{Q_1 Q_2^2 Q_3}$$

$Q_{i=123} = (1 - \exp(-\theta_i/T_i))^{-1}$, partition functions associated with the CO_2 symmetric, bending, and asymmetric modes respectively.

$P(J) = \frac{2hcB}{kT} \theta_J \exp\left(- \frac{hcBJ(J+1)}{kT}\right)$, where J is the rotational quantum number of the upper laser level.

$\theta_J = 2J + 1$

$B_{00^01} = 0.3866\ cm^{-1}$, [38]

$B_{10^00} = 0.3897 \text{ cm}^{-1}$

The stimulated emission cross-section, X_R, is defined by [21],

$$X_R = \frac{\lambda_L{}^2 P(J)}{8\pi\tau_s} g(f,f_o) \qquad . . . (3.18)$$

where λ_L is the radiation wavelength; τ_s, the spontaneous emission lifetime of the (00^01) level (τ_s = 5sec, [39]); and $g(f,f_o)$, the normalized response function of the upper level where f_o is the frequency at line center. For pressures less than approximately 30mm $g(f,f_o)$ is determined by both Doppler and collision broadening. At line center $g(f_o)$ is given by [40]

$$g(f_o) = \frac{2(\ell n2)^{1/2}}{\pi^{1/2}\Delta f_D} S(\xi) \qquad . . . (3.19)$$

where Δf_D is the Doppler linewidth (FWHM) and $S(\xi)$ is given by

$$S(\xi) = \exp(\xi^2)\left[1 - \text{Erf}(\xi)\right]$$

Erf is the error function and at zero field intensity ξ reduces to

$$\xi = (\ell n2)^{1/2} \Delta f_N/\Delta f_D$$

where Δf_N is the homogeneous or Lorentzian linewidth. The doppler width, Δf_D, at 10.6μ is a function of the translational temperature, T, [41]

$$\Delta f_D = 3.05 \times 10^6 \, T^{1/2}$$

The homogeneous linewidth, Δf_N, is pressure and temperature dependent [41],

$$\Delta f_N = \sum_s \frac{n_s Q_{s\text{-}CO_2}}{\pi} \left[\frac{8kT}{\pi} \left(\frac{1}{M_{CO_2}} + \frac{1}{M_s} \right) \right]^{\frac{1}{2}}$$

where n_s is the number density (per unit volume)of gas constituent s; $Q_{s\text{-}CO_2}$, the cross-section for optical broadening of CO_2 by species s; M_s, the atomic or molecular masses; and k, Boltzmann's constant. Cross-sections are given in references [37] and [41] for T near 300°K. The temperature dependence of $Q_{s\text{-}CO_2}$ was calculated in reference [21].

The above paragraphs discuss the stimulated emission terms in the energy balance equations. Attention is now focussed on gas dynamic equations which relate various thermodynamic properties through the electrical discharge or zone of heat addition.

3.2.4 *Gas Dynamic Equations*

Since considerable power was transferred to the flowing gas, translational temperature, gas density, and flow velocity variations were introduced into the computations. The main heating effect was assumed to be the collisional relaxation of vibrations to translation, whether it be collisions with heavy neutrals or collisions of the second kind involving electrons. Other translational energy transfer mechanisms, such as elastic electron-molecule collisions, were assumed to be relatively small [7].

In terms of gas dynamics the problem was treated as a diabatic or Rayleigh process [42] involving heat transfer in a channel of constant cross-sectional area. For subsonic flow, both the upstream and downstream conditions changed once the discharge was struck. Consequently, steady-flow equations cannot be used to relate the flow conditions before the discharge was turned on to conditions after, since this involved a non-steady problem requiring integration with time. For that reason computations were based on experimentally determined flow parameters.

Since momentum is conserved throughout the zone of heat addition, the momentum equation applies,

$$\frac{dp}{dz} + u\rho \frac{du}{dz} = 0 \qquad \text{. . . (3.20)}$$

p = free-stream pressure

ρ = mass density

u = flow velocity

The mass flow is assumed constant and therefore, the continuity equation applies, which for a constant area duct becomes

$$\rho \frac{du}{dz} + u \frac{d\rho}{dz} = 0 \qquad \text{. . . (3.21)}$$

The energy equation couples the gas dynamic and the vibrational excitation equations of section 3.2.1,

$$\frac{d(e_E - e_L)}{dz} = u \frac{du}{dz} + \frac{dh}{dz} \qquad \text{. . . (3.22)}$$

e_E = specific electrical input energy (per unit mass)

e_L = specific energy given up to laser radiation

$h = e_i + p/\rho$ = specific free-stream enthalpy

$e_i = e_T + e_r + e_v + e_e$ = specific internal energy

$e_T = \frac{3}{2}RT$ = translational energy

$e_r = RT$ = rotational energy

e_v = vibrational energy as given by equations of section 3.2.1

e_e = energy of electronic excitation. This term was omitted from the computations; likewise, the electrical input power did not include electronic excitation. For calculations of electrical conversion efficiency these considerations would have to be included in the equations.

R = ordinary gas constant

T = translational temperature

A fourth equation is provided by the equation of state which in differential form becomes

$$\frac{1}{p}\frac{dp}{dz} - \frac{1}{\rho}\frac{d\rho}{dz} - \frac{1}{T}\frac{dT}{dz} = 0 \qquad . . . (3.23)$$

A few general statements can be made about the expected changes of the flow parameters with heat addition [42]. For subsonic flow the stagnation temperature, T_o, increases as does the free-stream or static temperature, T, and Mach number, M. Consequently a velocity increase takes place through the flow while both p_o and p decrease along with the density, ρ.

The gas dynamic and vibrational excitation equations were incorporated into an APL computer program and solved numerically by the Hamming predictor-corrector method [43]. Output included small signal gain, translational and vibrational temperatures, and velocity, pressure, and density of the flowing gas. The results and comparisons with experiment are deferred to section 3.8. The intervening sections are devoted to a description of the laser system and a discussion of various experimental observations.

3.3 Experimental System

The experimental laser system is illustrated in Figures 3.1 (a),(b),(c). Figure 3.1(a) is a side elevation diagram showing the major components. Figure 3.1(b) and (c) are side evelation and top view photographs respectively of the complete laser system. As illustrated, a gas mixture initially of CO_2, N_2 and He, was circulated through a closed cycle by means of a centrifugal compressor driven by a 5 hp D.C. motor for variable flow rates. Cooling of the gas was provided by external water jackets on the flow ducts and a fiber-glass shell enclosing the top half of the centrifugal compressor. The electrodes for establishing the glow discharge within the laser cavity were installed in demountable plates. Pressure, temperature and electrostatic probes were also mounted in the detachable plates to analyze the flow through the discharge. Initially NaCl windows at the Brewster angle enclosed the ends of the laser cavity to permit spatial measurements of gain and visual observations of the interaction of the flow and the electrical discharge. The probe oscillator and scanner are shown in Figure 3.1(c). This arrangement will be discussed further in section 3.7. Later both stable and unstable resonators were mounted internally, Figures 3.1(b) and (c). A discussion of resonator details is likewise deferred to section 3.9.

3.3.1 *Glow Discharge Excitation*

All structures tested were arranged on opposite sides of the flow channel with anode to cathode separation equal to the channel height, H = 3.8cm. The excited length along the laser axis was 38cm, essentially the channel width. Excitation in the direction of flow was dependent on the number of electrode rows.

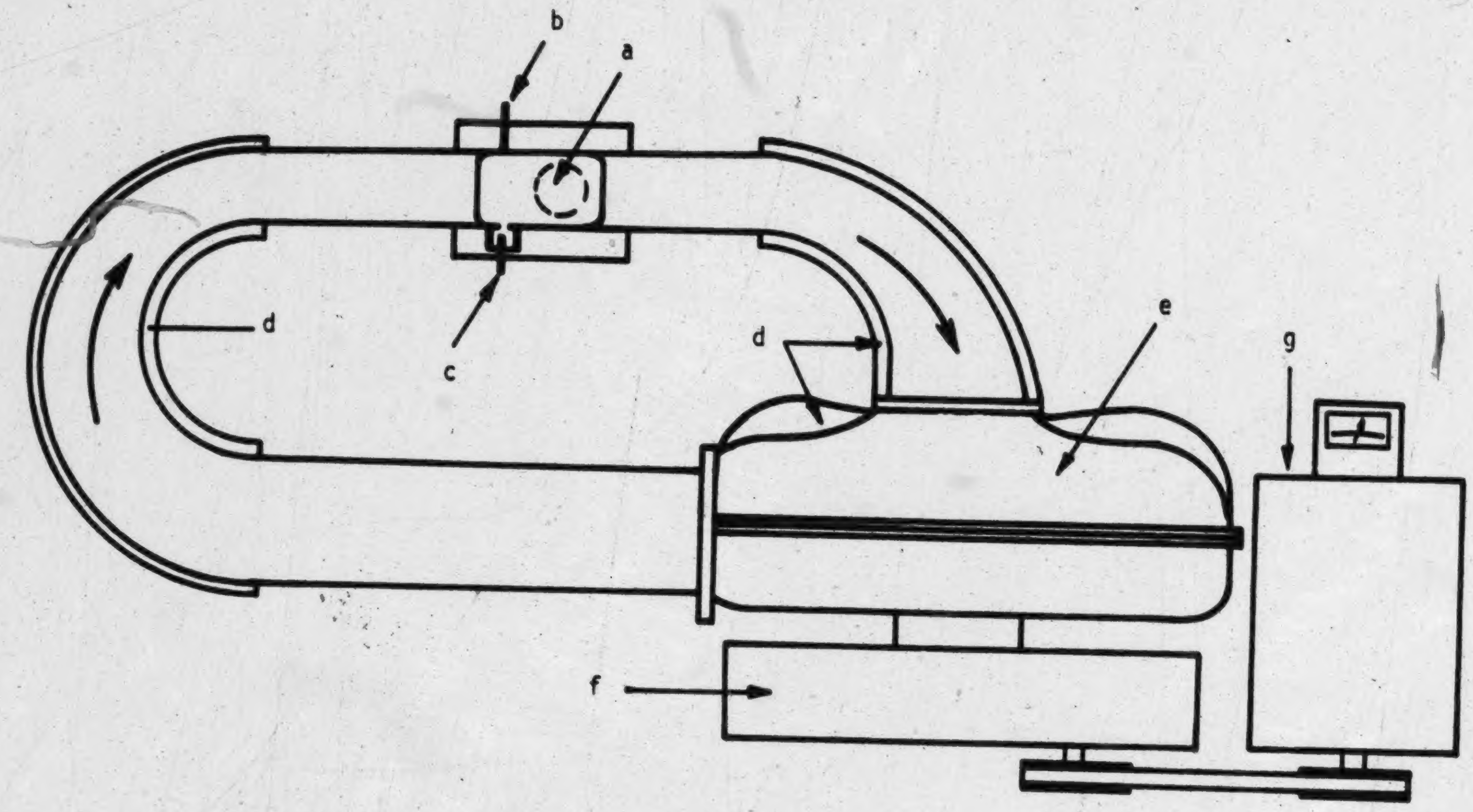

FIGURE 3.1(a). DIAGRAM OF HIGH-VELOCITY CROSS FLOW LASER.

a. Laser cavity (3.8 x 8.3 x 41 cm).
b. Individually ballasted anode pins.
c. Individually ballasted hollow cathodes.
d. Heat exchangers.
e. Centrifugal compressor.
f. 10:1 step-up drive box.
g. D.C. motor.

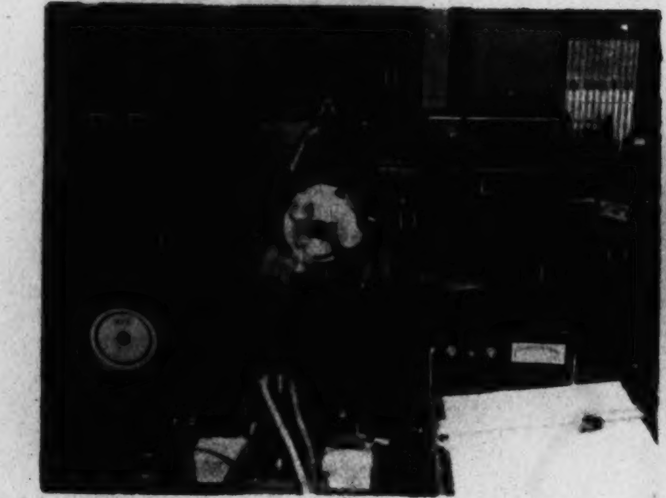

FIGURE 3.1(b). SIDE ELEVATION OF EXPERIMENTAL LASER

A. anode pins.
B. anode ballast.
C. water-cooled Ge output flat.
D. one of three discharge view-ports.
E. externally cooled flow ducts.
F. fiber-glass cooling shroud covering top half of centrifugal compressor.
H. 5 h.p. D.C. motor with tachometer.
J. mount for stainless-steel mirror adapted to previous NaCl Brewster-angle mount.

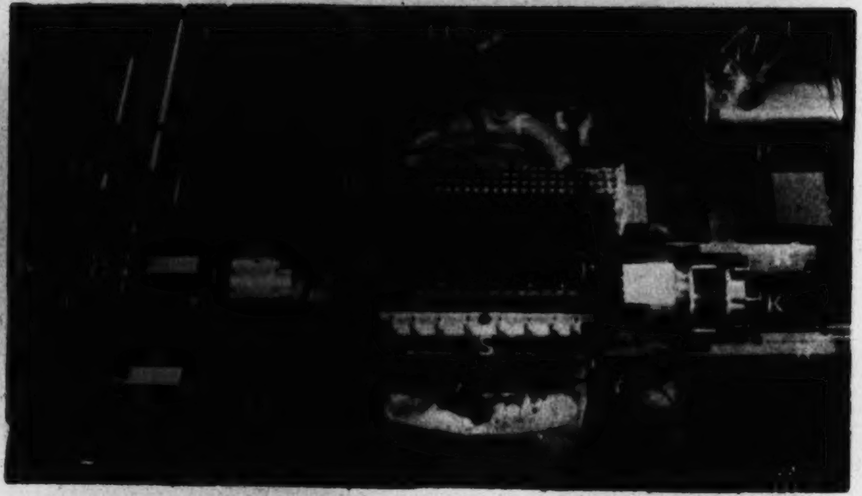

FIGURE 3.1(c). TOP VIEW. Scale shown in inches. Inset shows unstable resonator mount.

K. output mount containing water-cooled Ge flat and stainless-steel flat for two-path stable resonator.
L. two-mirror X-Y motion scanner for spatial gain profiles.
M. probe oscillator.
N. cathode ballast (concealed).
P. unstable resonator mount containing output coupler, convex mirror, and NaCl output window (T).
R. support beams for internal unstable resonator.
S. spark plugs for pre-ionization experiments.

Electrode elements were anchored in plates of perspex to provide electrical isolation from the channel walls. This was not sufficient, however, and further isolation was arranged by "floating" the power supply and dielectrically coating the interior of the flow channel some distance upstream and downstream of the electrodes. Several coats of Alkenex polyester resin (General Electric) were applied with baking to 150°C for several hours after each coat.

(a) *Anode electrodes*

The anode structures were consistently one to five rows of copper rods mounted flush with the flow, Figure 3.2(a),(b), and Figure 3.3. Due to the low melting point of perspex the anode pins were immersed in castable ceramic (Ceramacast 505, Aremco Products, Inc.) to a depth of 1cm. To permit electrode cooling by ordinary tap water inter-electrode isolation in the coolant channel was provided, again, by a thin coat of Alkenex polyester resin. Although a ballast resistance of 10KΩ was used for each anode pin, tests indicated that 1KΩ was sufficient for inter-electrode current balance. Further details of the anode structure are summarized in Table 3-3.

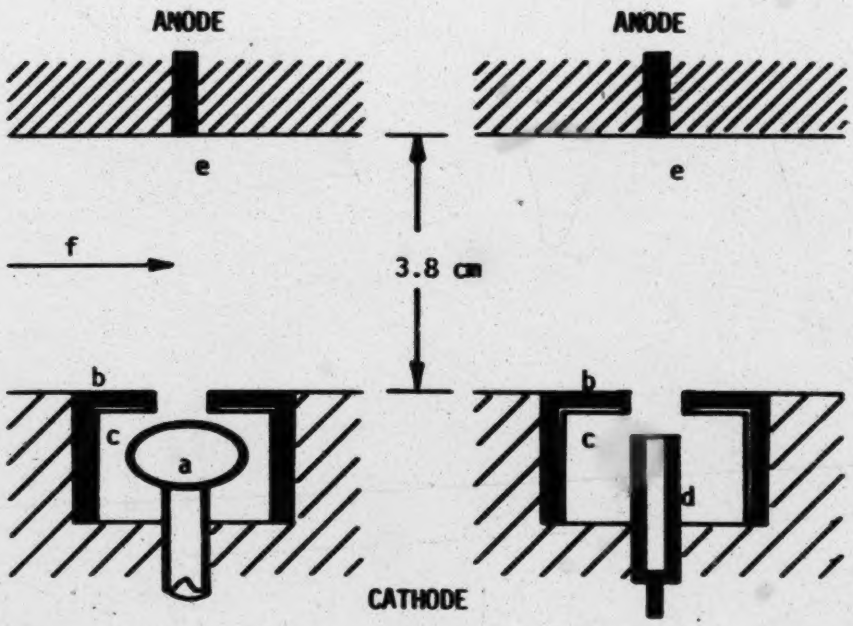

a - continuous convex cathode; copper; water-cooled; length,37cm; width,1.5cm

b - slotted shroud; electrically isolated; water-cooled; dimensions of opening, 9mm x 36cm

c - ceramic insulation on interior of shroud

d - single row of hollow cathodes; copper; water-cooled; 3mm o.d. x 1.5mm i.d.

e - anode pins; copper; water-cooled; 3mm diameter

f - gas flow direction

FIGURE 3.2. CROSS-SECTIONS OF ELECTRODE STRUCTURES EMPLOYING A CONTINUOUS CONVEX CATHODE AND A SINGLE ROW OF HOLLOW CATHODES

Table 3-3

Details of Anode Assembly for Cross-flow System

Configuration - multiple pin; up to five rows, staggered
Dimensions - 3mm diameter
- 12.5mm center to center within each row
- 9.5mm between rows
Material - copper
Ballast - approximately 10K ohms per pin
Coolant - tap water

(b) *Cathode electrodes*

As illustrated in Chapter 2, section 2.10 gas heating is greatly reduced by convection at low cross-flow velocities. Having observed in the low axial-flow experiments that gas heating contributed to failure of large surface electrodes by localized plasma contractions, single cathode elements were tested initially. Glow to arc transitions, however, continued to be a problem and a multiple electrode arrangement was again adopted.

Convex cathode

Figure 3.2(a) shows the cross-section of a single element convex cathode of copper. An electrically isolated shroud with a full-length slot reduced the Faraday dark space and anchored the discharge. Since much higher cross-flow was used insertion of a screen, as in the low-axial flow experiments of Chapter 2, only resulted in the discharge being swept downstream to the leeward edge of the mesh. The single element cathodes operated uniformly at low pressures and current densities <25mA/cm^2. With an increase in pressure and/or current the glow degenerated into several contracted columns or more often a single arc discharge fanning out near the anode, the anode consisting of individually ballasted pins. The boundary layer of stagnant gas appeared to play a role in this transition. Calculation plus observations of glow curvature near the electrodes indicated a boundary layer of 2 to 3mm on each side of the channel. Consequently, discharge heating was accentuated through this layer and it was obvious that before "break-up" the positive glow became filamentary along the leeward edge of the confining slot. Non-uniformities in the flow probably contributed to the glow to arc transition. That aerodynamic forces are significant was demonstrated by Hill [15] and Eckbreth and Owen [44].

Multiple hollow-cathode A

A linear array of 30 copper tubes (1.5mm i.d. x 3mm O.d.) replaced the single large surface structures, Figure 3.2(b). The tubes were used to confine the negative glow internally, reduce gas heating, and reduce the cathode fall potential as discussed in Chapter 1, section 1.2.3. Each hollow cathode was ballasted by 10K ohms. Stable operation to much higher gas pressures and current densities was achieved with this configuration.

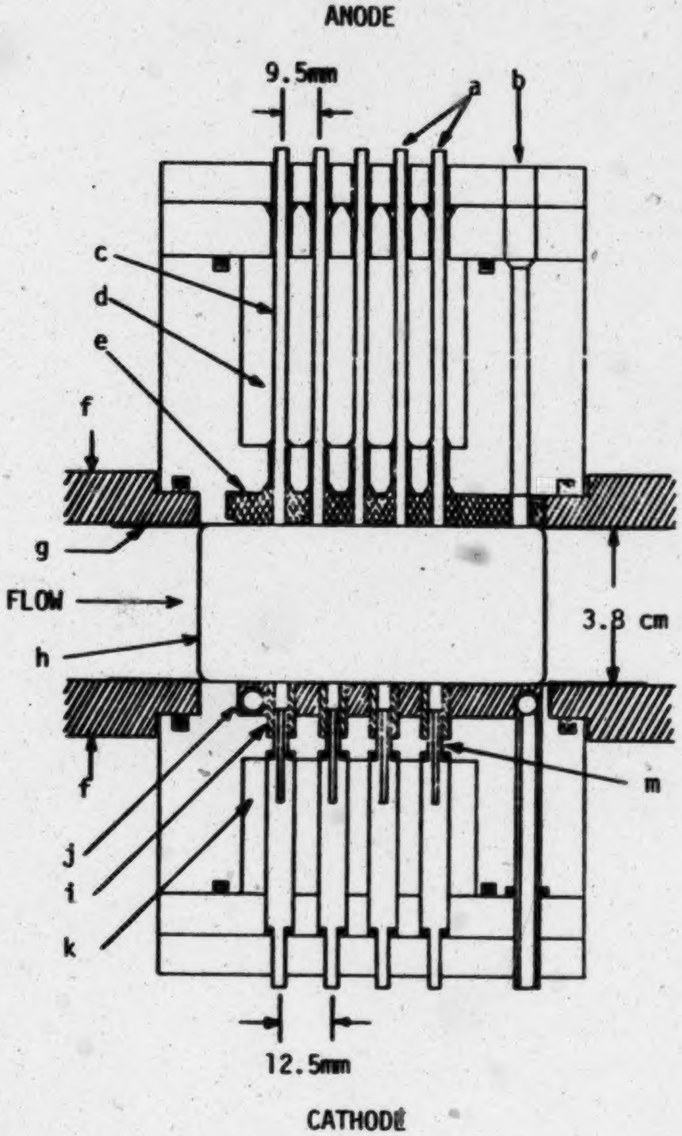
ANODE
9.5mm
a
b
c
d
e
f
g
FLOW
h
3.8 cm
f
m
j
i
k
12.5mm
CATHODE

a - copper anode pins (3mm diameter)
b - probe port
c - coating of Alkenex resin
d - water channel
e - castable ceramic
f - aluminum flow channel
g - Alkenex insulation
h - 3.8x8.3cm laser aperture
i - ceramic tubes, 3mm i.d.
j - water cooled copper plate
k - oil channel
m - hollow cathodes, 1.5mm i.d.x 3mm o.d.

FIGURE 3.3. DIAGRAM OF MULTIPLE ROW ELECTRODE ASSEMBLY.

Multiple hollow-cathode B

The single array of hollow cathodes was increased to a four row structure, Figure 3.3. The slotted shroud was replaced by a water-cooled copper plate into which a ceramic tube was inserted for each hollow cathode. The electrodes were recessed into the ceramic tubes approximately 10mm. This was to ensure that due to local wall losses the Faraday dark spaces were short and confined to the interiors of the ceramic tubes.

Table 3-4

Details of Multiple Hollow-Cathode Assembly for Cross-flow System

Configuration - multiple hollow cathode, up to four rows
Dimension - each electrode, 1.5mm i.d. x 3mm o.d.
- 12.5mm between centers within each row
- 11mm between rows
- electrodes recessed 10mm into 6mm o.d. by 3mm i.d. ceramic tubes.
Material - copper
Ballast - approximately 10K ohms per electrode
Coolant - refrigerated high-voltage transformer oil

3.3.2 *Gas Flow*

Gas flow was maintained by a centrifugal compressor. The particular unit used in the experiments of this thesis was taken from a General Electric turbo-supercharger used on World War Two vintage aircraft engines [45]. A centrifugal compressor by virtue of its high speed of rotation provides a high capacity (volume/unit time) in a small physical size. In addition, a much higher pressure ratio can be obtained over that of a centrifugal fan, for instance. Further details of compressor performance are extensively covered by Stepanoff [46].

Since the laser cavity was coupled directly to the impeller, a high speed vacuum seal was required between the drive and the flow ducts. The solution taken here was to provide an evacuated step-up drive, the seal now being made on the low speed shaft. Polyurethane belts ("Polyflex" - Gates Rubber Company) were used for the high-speed step-up. The drive was designed for speeds in excess of 20,000 rpm, the maximum normal operating speed of this particular compressor. Vacuum-pump oil was used for lubrication, with isolation from the flow ducts by a labyrinthseal between the drive box and the impeller. The intention was to flow any "make-up" or replacement gas through the labyrinth seal. The close tolerances, however, permitted only low replacements rates; less than 1% of the mass flow through the laser region. The effects of higher rates were observed by pumping gas from one of the flow ducts.

The center-line flow velocity was linearly proportional to compressor RPM as determined by pitot and static pressure measurements. The maximum gas velocity recorded was approximately 150m/sec. Most experiments, however, were confined to velocities of 80 m/sec or less.

3.3.3 *Temperature, pressure, electron density, and neutral species measurements*

(1) Translational temperature scans

Temperature scans were made by sweeping a copper-constantin probe through the discharge on a radial arm as illustrated in Figure 3.4, with the exposed lead wires and sensing tip orthogonal to the flow. Ideally, a stationary probe reads the local stagnation temperature, T_0.

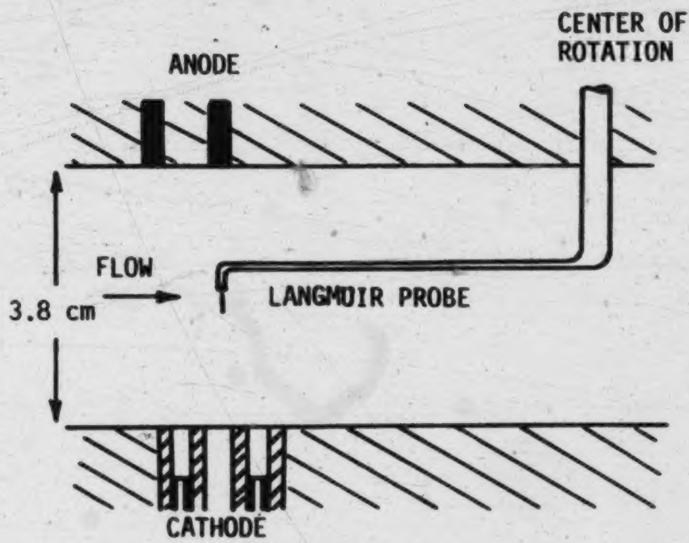
CENTER OF ROTATION
ANODE
FLOW
3.8 cm
LANGMUIR PROBE
CATHODE

FIGURE 3.4(a). PROBE CONFIGURATION AS VIEWED ALONG THE LASER AXIS.

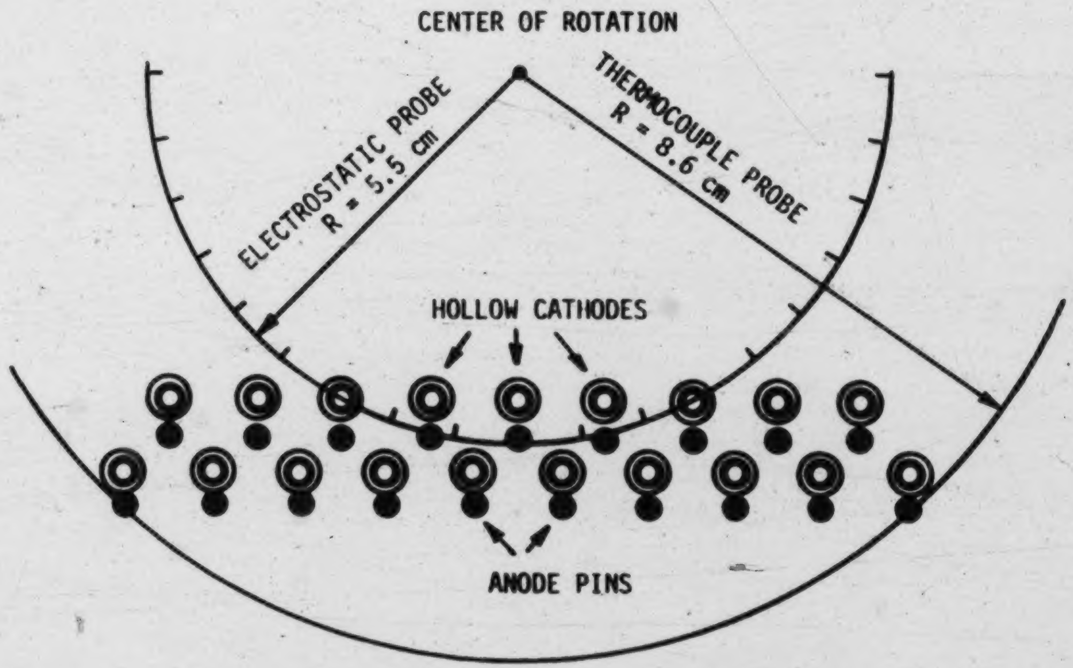
CENTER OF ROTATION
ELECTROSTATIC PROBE
R = 5.5 cm
THERMOCOUPLE PROBE
R = 8.6 cm
HOLLOW CATHODES
ANODE PINS

FIGURE 3.4(b). DIAGRAM OF RADIAL SWEEP OF LANGMUIR AND THERMOCOUPLE PROBES. VIEW FROM ANODE TO CATHODE.

Practically, however, a quite different temperature may be obtained. For the velocities encountered in the present experiments the static or free-stream temperature, T, is nearly equal to the stagnation temperature. The probe equilibrates at a temperature governed by the balance of heat transferred by convection to and from the gas, heat transferred by radiation and conduction to and from the external surroundings, and heat delivered to the probe by electrical currents flowing from the discharge. Heat loss by conduction was minimized by using small gauge wires sealed into a glass support. Exposure of a small length of the lead wires to the gas flow also reduces conduction losses from the sensing tip [47]. Conduction heat losses were assumed to be small. To reduce electrical interaction with the plasma, the probe was maintained at "floating" or isolated potential.

The importance of probe heating due to radiation from the plasma was deduced from measured translational temperature profiles through the discharge, as presented later in section 3.5. It was reasoned that if heat transfer by radiation and electrical currents was comparable to that by convection, a pronounced local temperature maximum would have been recorded by the probe as it passed through the core of the discharge. Only a small peak was observed. This corresponded to a local electron density peak as recorded by the electrostatic probe. It was assumed, therefore, that for the velocities employed, heat transfer to and from the probe by convection was dominant and that temperatures recorded were close to the actual free-stream values.

The response time was another consideration when the probe

Table 3-5

Thermocouple, Pitot-static, and Electrostatic Probes

Thermocouple probe	- 2mm twisted wire configuration with 3mm length of exposed leads
	- 0.25mm diameter Cu - constantin wire (30 gauge)
	- estimated response time, $\tau=3$ sec
	- glass support stem
Pitot and static pressures	- pitot tube extended 2.5 cm in direction of flow; 1.5mm i.d.
	- static pressure from 0.5mm hole in channel wall located opposite pitot tube
	- absolute pressures by Wallace-Ternan gauge
	- differential pressures by MKS-Baratron-Type 77 capacitance manometer
Electrostatic probe	- 0.1mm diameter tungsten
	- 2mm length
	- glass insulation except for sensing tip
	- bias supply, Fluke 210C
	- current sensing resistance 100 ohms

was scanned through the flow. A recovery time constant of 3 to 4 seconds was estimated for the pressures of the present experiments [48]. It was observed experimentally that a few seconds were required at each station for thermal equilibration.

Further details on probe swing and construction details are contained in Figure 3.4 and Table 3-5.

(2) Pitot and static pressures for flow velocity calculations

A pitot tube measured the stagnation pressure, p_o, and a small diameter hole in the channel wall gave the static pressure, p. Construction details are contained in Table 3-5. Differential measurements were made using, initially, a tilting manometer filled with dibutyl phthalate and later a capacitance manometer which greatly increased the sensitivity and reading accuracy. The absolute pitot pressure was measured with a Wallace-Ternan gauge.

For low Mach numbers it was found convenient to use the following expression [49] to relate the flow velocity to the difference between static and pitot pressures,

$$p_o - p = 0.5\rho u^2 \left(1 + \frac{M^2}{4} + \frac{2-\gamma}{24} M^4 + \ldots\ldots\right)$$

ρ = mass density of gas mixture

u = flow velocity

M = Mach number

γ = ratio of the specific heats

Since M was less than 0.3, the following formula was used to compute flow velocities,

$$p_o - p \approx 0.5\rho u^2$$

(3) Plasma density scans

Plasma density was analyzed by sweeping an electrostatic probe on a radial arm through the electrical discharge, Figure 3.4, such that the gas flow was perpendicular to the probe axis. The ion-saturation current was collected and analyzed by both velocity dependent and static formulas to estimate the electron density, section 3.6.

The probe was cleaned by ion bombardment before each scan, however, in a static gas and for very low velocities a time dependent phenomena occurred which prevented useful measurements. This problem appeared to have vanished for velocities greater than 10 m/sec and was assumed to have been associated with probe heating.

The probe bias was referenced to the B+ of the discharge supply with the ion current sensed by measuring the voltage across 100 ohms in series with the probe. Most currents were collected at a probe to plasma potential of approximately 60V. Plots of probe current versus angular position were displayed on an X-Y recorder. Details of the probe construction are contained in Table 3-5.

(4) Dissociation of CO_2

The electric discharge may cause considerable dissociation of CO_2 into CO and O_2 as discussed in Chapter 1, section 1.4.

The dissociation equilibration time was determined by monitoring with a photomultiplier the sidelight emission from the CO

Angstrom band (4835 Å). For an initial mixture $CO_2/N_2/He$ - 4/4/6mm, a flow velocity of 40m/sec, and a discharge current of 2A through two rows of electrodes both anode and cathode, initial dissociation equilibration was obtained in approximately one minute. The degree of dissociation was monitored both by observing the gas pressure increase and collecting before and after gas samples for mass spectrometric analyses. Pressures were read after extinquishing the discharge and allowing the gas temperature to return to its initial value. The dissociation fraction ($\delta = N_{CO}/N_{CO} + N_{CO_2}$) was calculated on the assumption of conservation of oxygen. That this was justified was supported by mass spectrometric data, which showed that the quantity of O_2 was approximately one-half that of CO, thus satisfying the dissociation reaction

$$CO_2 \rightleftarrows CO + \frac{1}{2}O_2$$

Both of the methods indicated $\delta = 0.3$ for the conditions cited above. Note that the above tests were conducted within a relatively short period of operation (approximately ten minutes). Over a longer period the dissociation reaction is expected to shift to the right according to Le Chatelier's principle as chemical reaction takes place with the electrodes [50] [51]. For instance a loss of oxygen shifts the reaction to the right. A carbon deposit gradually collected around the copper cathode electrodes which was probably associated with a further disappearance of CO_2.

3.4 Correlation of Side-light Measurements with V-I Characteristics

3.4.1 *Visual Changes in side-light emission*

The cross-flow produced significant changes in the plasma shape and visible side-light emission. The visual variations of the positive glow were recorded in a series of photographs, Figure 3.5, which show the changes with flow velocity as viewed along the laser axis, that is, perpendicular to the gas flow. The flow direction is from left to right. The off-vertical image was the result of a slight upstream shift of the anode rows relative to the cathode. Note that reflections through the salt windows produced a spurious image below the anode (arrow, Figure 3.5(d)). Also, the anode surfaces had small intense "spots" producing over exposure from that region of the discharge. All photographs were taken at constant exposure settings.

Measurement parameters:

Partial pressures - 4/4/6mm of $CO_2/N_2/He$
Discharge current - anode and cathode of two multi-electrode rows each
- 1 A total, 17 mA per electrode pair
Flow velocity - 0 to 80 m/sec, downstream from discharge
Film type - Polaroid 410, ASA 3000
- exposure settings, 4.7 at 1/10 sec.

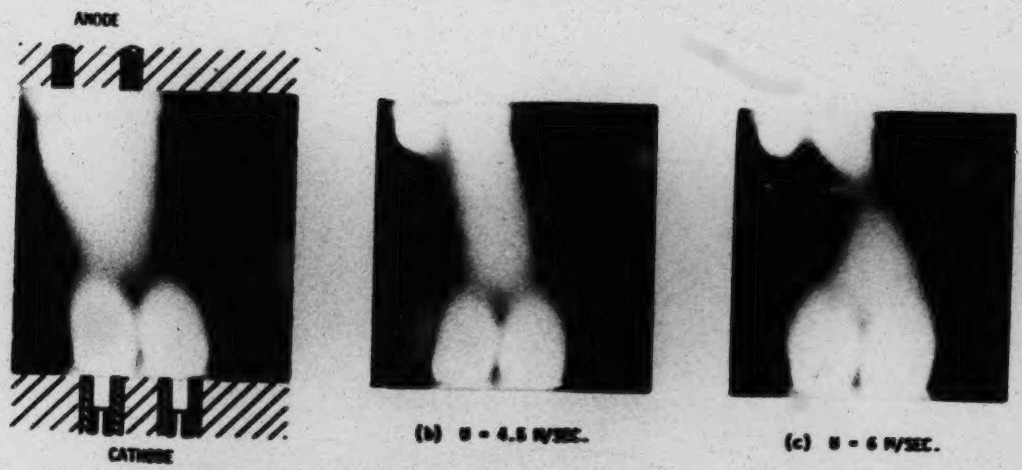

(a) U = 0 M/SEC.

(b) U = 4.5 M/SEC.

(c) U = 6 M/SEC.

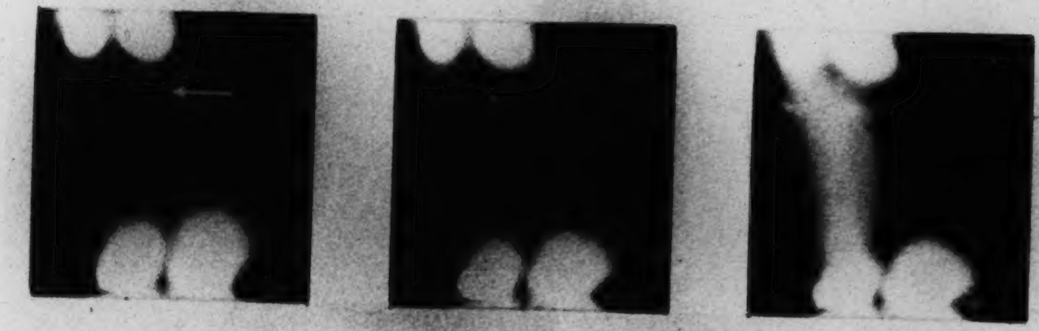

(d) U = 16 M/SEC.

(e) U = 25 M/SEC.

(f) U = 33 M/SEC.

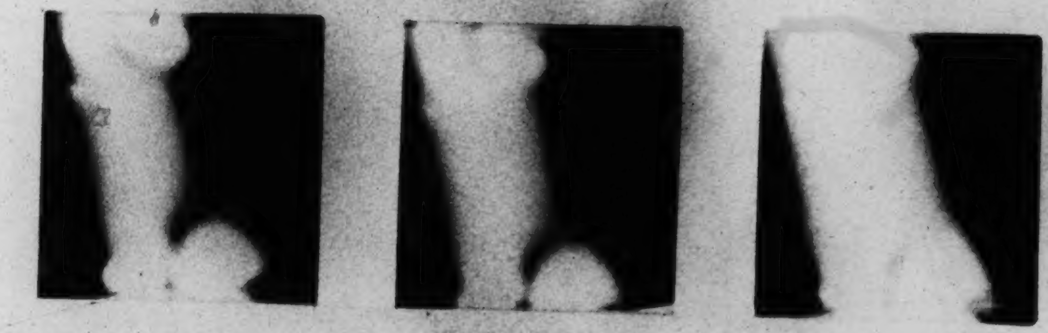

(g) U = 40 M/SEC.

(h) U = 56 M/SEC.

(i) U = 80 M/SEC.

FIGURE 3.5. VISUAL CHANGES OF THE POSITIVE COLUMN WITH FLOW VELOCITY

$CO_2/N_2/He$ -4/4/6 mm; discharge current,1A total; 17 mA per electrode pair; arrow,3.5(d),marks spurious reflections from the Brewster-angle windows.

With no flow, Figure 3.5(a), the column corresponded to the usual contracted glow where the central core was a region of high gas temperature with reduced gas density. There were variations in luminosity just above the hollow cathodes, in the region which would otherwise have been filled with a Faraday dark space in the absence of the ceramic tubes. This phenomena has been explained on the basis of a sheath that is known to build up at bore constrictions [52]. For the low-flow cases much higher ionization density occurred inside the tube than in the laser region, the sheath forming to balance the current flow across the constriction. The condition for the appearance of the sheath is given approximately by $I < A \chi j_e$, where A is the area of the ceramic tube aperture; j_e, the random current density inside the tube; and I, the discharge current [52]. Little experimentation was done with the variation of cathode depth below the constriction, but it is expected that the cathode depth could be reduced to minimize or eliminate this sheath effect at least over a certain range of parameters.

As the flow rate was increased above zero, the positive glow intensity passed through a minimum. Initially the plasma column was bowed downstream by the flow, Figure(b), until the column broke, Figure 3.5(c), and passed through a luminosity minimum, Figure 3.5(d). A further rise in flow caused the positive glow to "re-appear", Figure 3.5(e), increasing in visual intensity thereafter. After reaching a velocity of approximately 30 m/sec the intensification was more gradual. The "second" positive glow was stable against the flow maintaining an almost constant position, however, the visible width of the glow gradually increased over the 30 to 80 m/sec range.

An explanation of the observed events appears to be rather complex. For low flow, gas heating of the discharge core appeared to be a dominant effect. The discharge favoured the lower density of the contracted column and exhibited flexure in the presence of flow. This probably was not unlike the case of high current arc discharges which behave like solid aerodynamic drag bodies when subjected to a cross-flow [53]. It is assumed, therefore, that the contracted glow bowed downstream preserving the low density core until the increased discharge length and gas cooling caused a change in the operating regime. The decrease in luminous intensity at this point may have been associated with electron density changes rather than any decrease in average electron energy. Indications were that E/N increased monotonically with gas velocity. If stepwise excitation was present in the contracted low-flow column then, since this process is proportional to the square of the electron density, a small reduction in density could have a pronounced effect on the luminosity. Higher flow increased the charged-particle loss from the plasma and had a concentrating effect on the ionization density in that the lateral diffusion of the plasma from each electrode pair was reduced. In other words, as will be seen in section 3.5, as the flow was raised, density structure persisted for longer distances behind each electrode pair. It was assumed that, since E/N rose with velocity, the average electron energy likewise increased and that this, coupled with possible electron density effects caused the gradual increase in visible intensity seen in the 30 to 80 m/sec range of Figure 3.5.

3.4.2 *Flow effects on discharge potential*

The discharge potential, Figure 3.6, was monitored as the photographs of Figure 3.5 were taken. The measured discharge potential included the cathode fall which was assumed to be nearly independent of velocity for a given current. Consequently, any changes in plasma impedance were due almost entirely to flow effects on the positive glow. The discharge potential rose monotonically with velocity. The characteristic for a discharge current, I_D, of 1A can be directly correlated with the visual observations of Figure 3.5. By so doing, it was observed that the glow minimum corresponded to the local changes of slope around 20 m/sec. Once the glow became more fully developed a gradual slope prevailed. This fits well with the luminosity changes.

The potential rise with flow was due to an increase in both the gas density and the charged-particle loss from the plasma. Spatial temperature profiles indicated that, for a constant discharge current, the gas temperature fell rapidly as the flow velocity was raised above zero. The associated potential rise is illustrated in Figure 3.6. As the flow was raised further, the downstream temperature approached that of the entering gas. Consequently, gas density effects became less pronounced. For the conditions of Figure 3.6, the potential showed a more gradual rise past 30 m/sec. This was coincident with a gradual increase in luminosity as discussed in section 3.4.1. The reduced electric field, E/N, rose with velocity and it is assumed that convective losses from the plasma resulted in a gradual increase of average electron energy.

Data is also shown in Figure 3.6 for a discharge current of

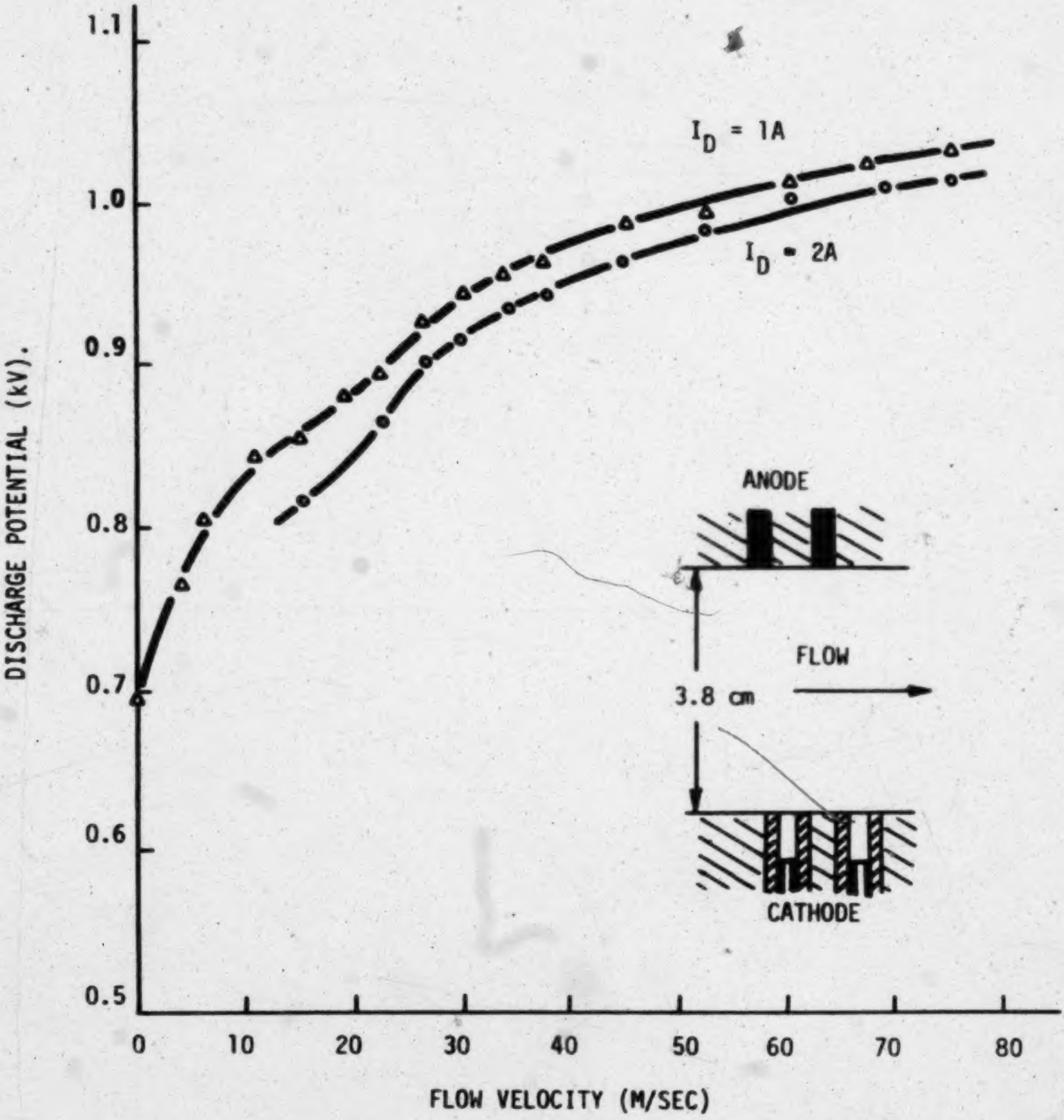

FIGURE 3.6. VARIATION OF DISCHARGE POTENTIAL WITH FLOW VELOCITY. $CO_2/N_2/He$ - 4/4/6 mm; I_D = TOTAL DISCHARGE CURRENT; FLOW VELOCITY MEASURED ALONG CENTER-LINE. E/N was approximately $3.6 \times 10^{-16} cm^2$ volt at I_D=2A and u=35m/sec.

2A. The reduced discharge potential appeared to be associated with gas density changes. This was more evident from V-I characteristics for various velocities. For higher flow, the potential showed a more gradual decrease as the current was raised.

Reiterating, gas density showed a marked change at low flow while plasma losses were dominated by ambipolar diffusion. As a result, for low flow the discharge potential rose primarily due to an increase in gas density. At high flow, gas density changes were small while convective plasma losses became more dominant. Consequently, for high flow, an increase in discharge potential was primarily associated with convective charged particle losses. Assuming that the average electron energy was sufficiently high that vibrational excitation rates were nearly constant with energy, increasing flow was expected to increase the fractional power coupled into electronic excitation with a resultant decrease in laser efficiency [54].

3.5 Translational Temperature Profiles

As indicated previously in Figure 3.1, section 3.3, the gas stream was cooled by flowing tap water through heat exchangers attached externally to the flow ducts and a shroud encompassing the top half of the centrifugal compressor. Spatial temperature profiles were scanned by sweeping a thermocouple through the electrical discharge, as described in section 3.3.3.

Figure 3.7 illustrates temperature profiles scanned in a plane midway between the electrodes versus distance in the flow direction. Distance was referenced to the upstream anode row, while the indicated flow velocities were those measured downstream from

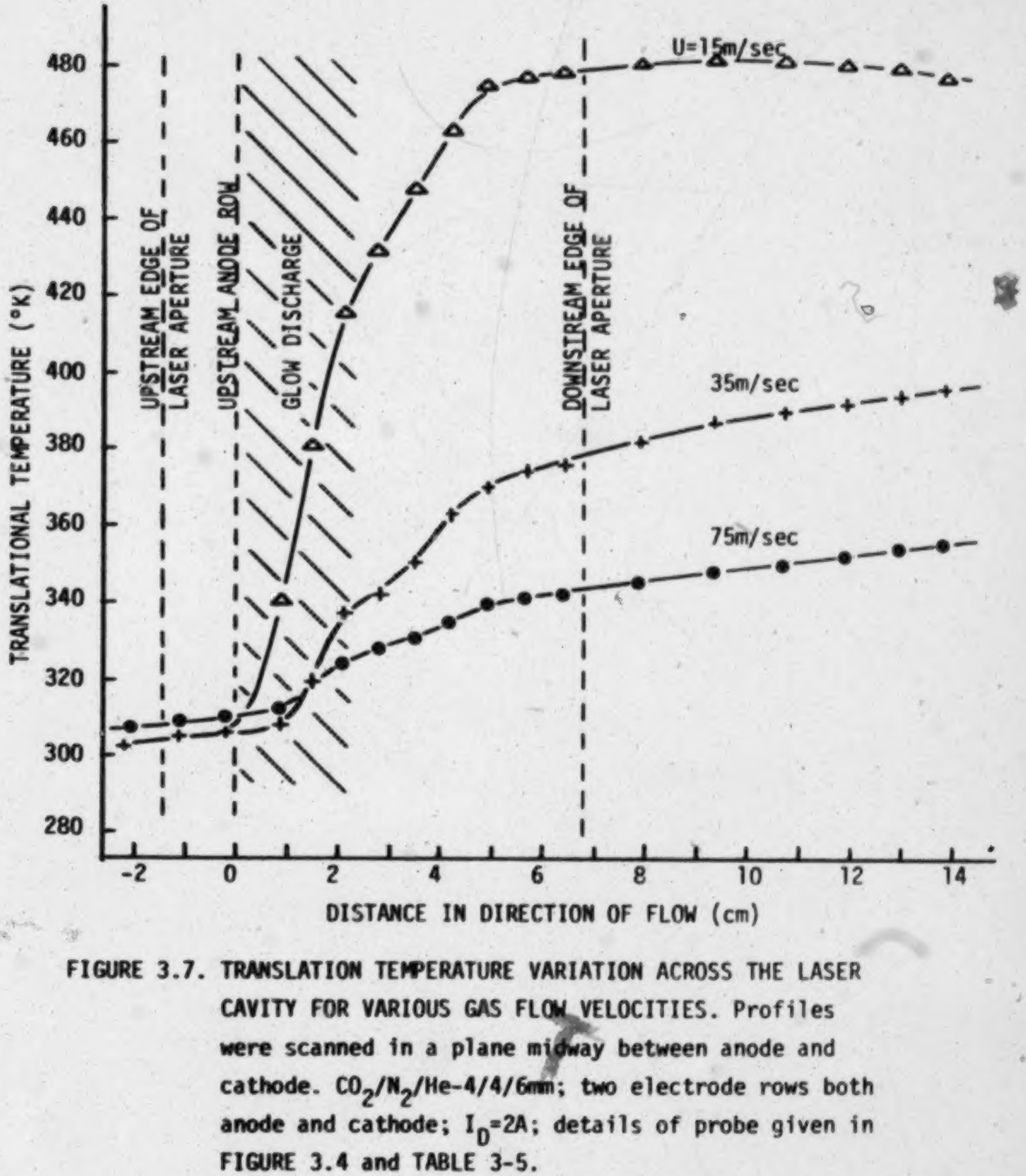

FIGURE 3.7. TRANSLATION TEMPERATURE VARIATION ACROSS THE LASER CAVITY FOR VARIOUS GAS FLOW VELOCITIES. Profiles were scanned in a plane midway between anode and cathode. $CO_2/N_2/He$-4/4/6mm; two electrode rows both anode and cathode; I_D=2A; details of probe given in FIGURE 3.4 and TABLE 3-5.

the electrical discharge. The profiles were recorded with a replacement gas flow rate of approximately 1% of the channel mass flow.

The effect of convective cooling was immediately obvious. Over the flow range shown in Figure 3.7, the downstream temperature decreased by approximately $140^{o}K$ at a discharge current of 2A (an electrical power of approximately 2KW into the positive glow). Although recordings were not conducted for this discharge current in a static fill, because of excessive heating, it was assumed that a temperature of 700 to $800^{o}K$ was not an unreasonable estimate [7]. In other words, a decrease of approximately $500^{o}K$ was effected by raising the velocity to 75 m/sec.

As will be shown later by the electron density scans of section 3.6, the center of the discharge was located at approximately +2cm. The temperature profiles of Figure 3.7 show local peaks near this position. Correlation with electron density data showed that the temperature maximum corresponded to a local peak in the electron density introduced by the segmented electrodes. There was no maximum directly attributable to the effects of radiation and electrical currents as the probe passed through the discharge. Consequently, these effects were assumed small relative to convective heat transfer. Deactivation of vibrational species by the probe surface may have increased the recorded temperature. Here again, the error was reduced by convection. Variations introduced by the changing orientation of probe surface and flow direction likewise appeared to be small.

The largest error appeared to be radiation from the probe to the cool walls. For a wall temperature of 300^{o}K, a probe temperature of 400^{o}K, and a flow velocity of 40m/sec the radiation error was estimated to be not greater than 5^{o}C.

Since the probe was rotated on a long arm (8.6 cm) care had to be exercised to minimize error introduced into recorded probe position. The angular error was taken as $\pm 1^{o}$ of rotation, resulting in a maximum error of $\pm$1.5mm in the direction of flow.

Profiles of translational temperature were used to calculate neutral number densities for estimates of E/N and average electron energy, to correct for mobility and velocity changes in determinations of electron density, and to compare experimental and calculated translational temperatures in computations of laser gain.

3.6 Measurements of Ionization Density

The results of several electrostatic probe and microwave measurements on longitudinal CO_2 laser plasmas have been published. Both single and double probe measurements have been analyzed by standard techniques assuming a Maxwellian distribution of electron velocity [55] [56]. More sophisticated probe techniques, where the actual energy distribution was measured, have shown that the distribution is quite non-Maxwellian [57] [58]. Since the double-probe senses only the high-energy tail of the electron distribution, interpretation of the usual double-probe curve becomes complex.

Collision and diffusion effects at high pressure (ion and electron mean free paths less than the probe sheath diameter) further complicate the analysis of the retarding-field region of the probe characteristics. Consequently, most probe measurements of the CO_2 laser plasma have been confined to pressures of a few torr or less.

Electron-radiation temperatures have also been measured by several investigators [59] [60] [61]. This technique creates no disturbance of the plasma, the average electron energy is related to the measured electron-radiation temperature nearly independent of the velocity distribution [61], and measurements can be extended to high pressures [60]. The spatial resolution relative to that of the electrostatic probe is low.

Average electron densities in longitudinal tube discharges have been measured by microwave techniques [55] [56] [62] [63]. These experiments indicated a more or less linear increase of average density with discharge current. Average densities in the range 0.5 to 1 x $10^{10} cm^{-3}$ were observed for the usual discharge currents.

Since high spatial resolution was desired in the present experiments, a single electrostatic probe was swept through the plasma. Ion saturation current was collected and analyzed by both static and flow-dependent formulas to give an estimate of the spatial ionization density. Average electron energies were estimated from measured values of the reduced electric field, E/N, due to the difficulties of recording and analyzing the retarding-field region of the probe characteristic as mentioned above.

3.6.1 *Experimental profiles of the electrostatic probe currents*

By rotating a cylindrical electrostatic probe through the discharge on a radial arm as outlined in section 3.3.3, the ionization density was effectively sampled both along and transverse to the flow giving a measure of the spatial uniformity of the active medium. Typical scans of ion-saturation current are shown in Figure 3.8. Experimental curves were displayed on an x-y recorder for two different flow rates with the discharge current constant at 2A. For these particular curves the probe bias was constant over the scan. As a result currents collected downstream were somewhat high. These traces are presented to illustrate electron density structure within the discharge where only small variations in space potential were evident. Consequently, constant probe bias was essentially constant probe to plasma potential. Each curve was traced out at least twice and the symmetry was the result of scanning either side of zero, the most upstream point of the probe swing. It is obvious that the structure was more pronounced for higher flow rates. A point to note is the appearance of an additional ion current peak towards the afterglow side of the upper curve, Figure 3.8.

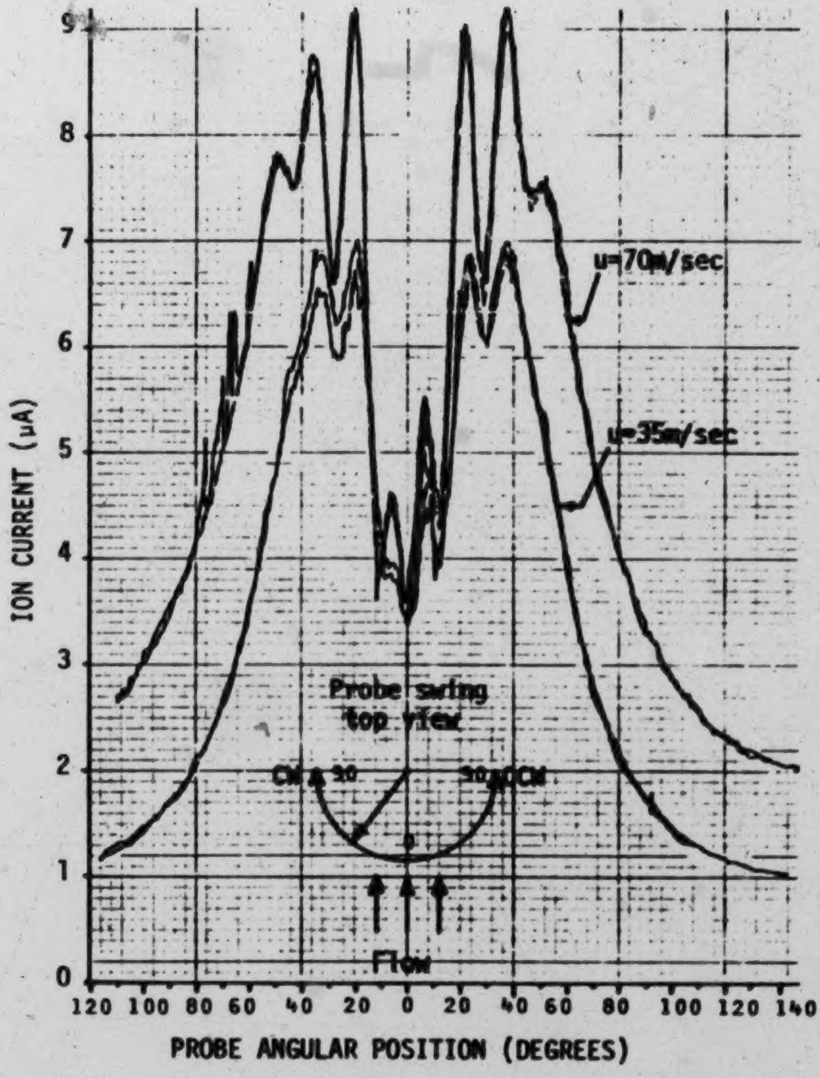

FIGURE 3.8. ION-SATURATION CURRENT TO A CYLINDRICAL ELECTROSTATIC PROBE NORMAL TO THE FLOW. Initial fill, $CO_2/N_2/He$-4/4/6mm; I_D=2A; electrode configuration outlined in FIGURE 3.4.

There is only a slight indication of this peak in the lower velocity scan. By correlation of the probe current with electrode geometry the appearance of this peak gave an indication of the lateral downstream spreading of the charged-particle density between adjacent electrode pairs.

Spatial ion current profiles versus downstream distance, Figure 3.9, were compiled from ion current scans at constant probe to plasma potential and the probe position diagram of Figure 3.4(b). Within the discharge, two curves were generated for each flow rate. The upper curve is drawn through points located directly downstream of the most upstream electrode pairs, while the lower consists of currents measured behind the most downstream pairs. Data are shown for the flow velocities and discharge current of Figure 3.8. Structure present within the discharge rapidly disappeared once within the afterglow. Also, the current variation between adjacent electrode pairs of the downstream row was less pronounced than for the upstream electrodes. It is assumed that the upstream electrodes effectively pre-ionized those downstream. As a result, a slight reduction in running potential was observed in the direction of flow. This was more evident when the electrode structures were extended by additional rows. The decreased gas density as the translational temperature rose through the discharge also contributed to the voltage reduction.

Another feature evident from Figure 3.9 is that substantial ionization existed even at the most downstream point of the probe scan (approximately 10cm from the discharge). The electron energy, however, is assumed to relax rapidly once within the afterglow. An electron relaxation time of the order of a few microseconds [64] was expected in

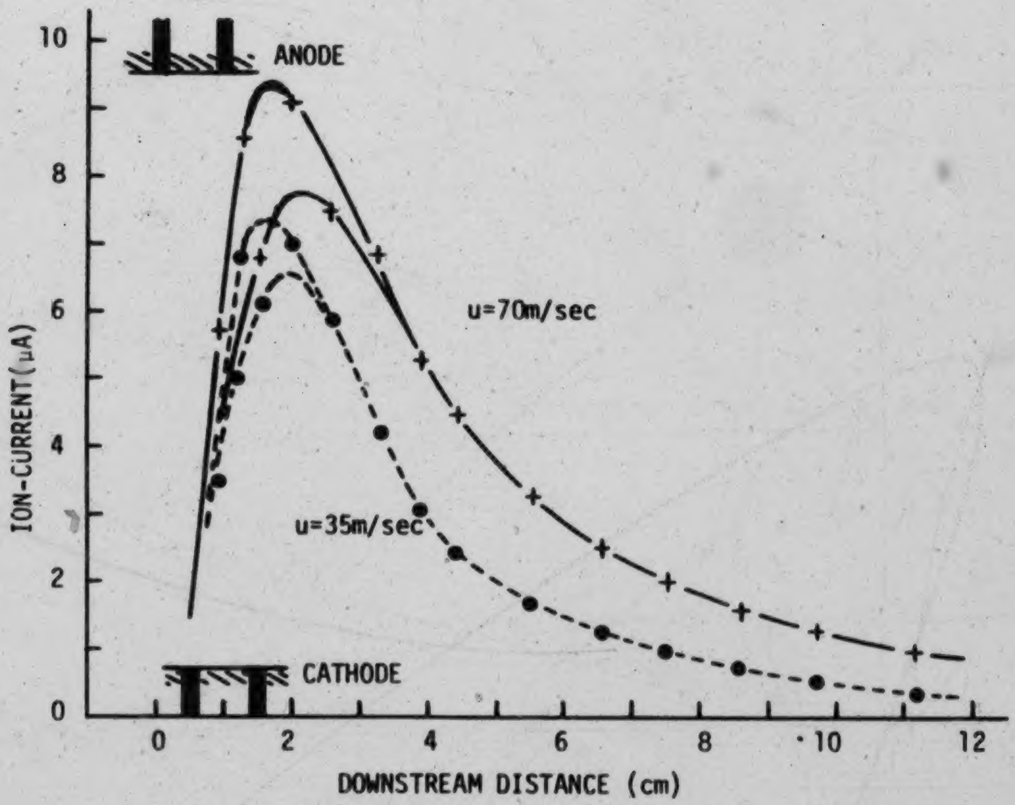

FIGURE 3.9. VARIATION OF ION-SATURATION CURRENT IN DIRECTION OF FLOW. Initial $CO_2/N_2/He$-4/4/6mm; probe to plasma potential,=-60V; I_D=2A; electrodes as in FIGURE 3.4 (1.25cm between adjacent electrodes within each row); scan midway between anode and cathode.

the absence of collisions of the second kind, a time fast relative to flow transit times. The relaxation of the electron energy could be considerably lengthened by electron collisions with vibrationally excited species. The decay of the electron density was expected to be controlled both by ambipolar diffusion losses to the walls and volume recombination. To make conditions even more complex, the ionic species in the afterglow may have been different from those of the active discharge due to processes such as charge transfer. For instance, fast charge-transfer rate constants (10^{10} cm^3 sec^{-1}) have been measured for the reaction of CO_2^+ with O_2 to produce O_2^+ [65].

3.6.2 *Computations of the electron density*

The first aspect in the determination of the ionization density concerned the identification of the major ionic species present in the positive column of a glow discharge in $CO_2/CO/O_2/N_2/He$. This information was required to estimate the ionic mobility used in the various formulas. From ionic sampling done on pure CO_2, the dominant ions in the active discharge were CO_2^+ and O_2^+ [66] [67]. CO_2^+ is assumed to be produced by direct electron impact. O_2 is produced by way of the dissociation of CO_2. It is known that the rate of charge transfer between CO_2^+ and O_2 is rapid [65], therefore, O_2^+ may become the dominant ion if sufficient oxygen is present. Since CO_2 has a low ionization potential relative to the other constituents CO_2^+ and O_2^+ are expected to be dominant in the CO_2 laser plasma. This contention is supported by Wiegand et al [68]. Only a few experimental studies have been done on ion production in the CO_2 laser mixture. Freudenthal analyzed fast ions from near the cathode of a sealed-off discharge and found several ions including abundant C^+, some NO^+, but no O_2^+ [69]. Austin and Smith measured positive ions from a flowing CO_2 laser mixture and found masses 28 and 32 dominant which were identified with N_2^+, CO^+, and O_2^+ [70]. A more recent study by Tannen et al has shown that CO_2^+ was the major initial ion at the cathode of a sealed tube but was rapidly replaced by NO^+ [71]. In a He/CO_2 mixture, however, the initial CO_2^+ ion was replaced by O_2^+.

The ionic mobility, μ_i, was calculated using the quantum mechanical equivalent of Langevin's equation for the case where polarization forces are dominant [72]. For a gas mixture of $CO_2/CO/O_2/N_2/He$ - 2.8/1.2/0.6/4/6mm, corresponding to a dissociation fraction of 0.3, the calculated ionic mobility at $T=300^0K$ ranged from 180 cm^2/volt sec for CO_2^+ to 215 cm^2/volt sec for NO^+.

The regime of probe operation was determined by calculating several non-dimensional parameters, defined as follows:

(1) $\alpha = \frac{\lambda_D}{L}$

λ_D - the Debye length

L - length of a typical probe dimension; $L=2r_p$ for the cylindrical case considered here where r_p=probe radius

$$\lambda_D = \left(\frac{\epsilon_o k T_e}{n_e e^2}\right)^{1/2}$$

ϵ_o - permittivity of free space

k - Boltzmann's constant

T_e - electron temperature

n_e - electron density

e - electronic charge

(2) $\chi = \frac{eV}{kT_e}$

χ - the normalized probe potential

V - probe to plasma potential

(3) $R_e = \frac{u\,L}{\mu_i\left(\frac{kT_e}{e}\right)}$

R_e - the electric Reynold's number

u - flow velocity

μ_i - ionic mobility

The electric Reynold's number, R_e, gives a measure of the flow effects relative to the ionic diffusion velocity. The condition $R_e>1$ suggests that the probe current may be velocity dependent. For $\chi>>1$, convection may be significant for lower values of R_e[73].

Table 3-6 contains calculated parameters describing conditions both within the active discharge and the flowing afterglow.

Table 3-6

Probe and Plasma Parameters

Active Discharge		Afterglow
	$u=10\to80$ m/sec	
	$L=2r_p=10^{-4}$m	
	$\ell_p=2\times10^{-3}$m	
	$V=60V$	
	$\lambda_D=10^{-4}$m	
	$\mu_i=0.02m^2$/volt sec	
	$\lambda_i=2\times10^{-6}$m	
$T_e=20{,}000^{\circ}K$		$T_e=T_g$
$T_g=320\to600^{\circ}K$		$T_g=350\to600^{\circ}K$
$\alpha=1$		$\alpha=0.2$
$\chi=35$		$\chi=1800$
$R_e=0.03\to0.25$		$R_e=3\to12$
$R_e\alpha^2\chi^2=40\to300$		$R_e\alpha^2\chi^2=4\times10^5\to$ 1.5×10^6

λ_i - the ionic mean free path, T_g - the gas temperature,

ℓ_p - the probe length; other symbols as previously defined.

Electron density

The above paragraphs outlined the measured spatial ion currents, the expected ionic species, a calculated ionic mobility, and various non-dimensional parameters describing probe conditions in the discharge and flowing afterglow. This leads now to the calculation of the ionization density. Both static and kinetic formulas were employed. From Table 3-6 it is seen that the ionic mean free path was small relative to the probe diameter and that the Debye length was the order of the probe diameter ($\alpha \approx 1$). Consequently, a "thick" collision-dominated ion sheath was expected. The theory of Schulz and Brown [74] was developed to account for collisions within the ion sheath of a probe immersed in a static plasma. The kinetic theory of Clements and Smy is applicable where the collected ion current is dominated by convection of ions into the sheath. Both thick and thin sheath formulas have been developed [73] [75]. The non-dimensional parameter $R_e\alpha^2\chi^2$ (Table 3-6) determines the regime of operation. A normalized probe potential $\chi >> 1$, and $R_e\alpha^2\chi^2 \geq 1$ suggest that the sheath is thick and that the collected ion current is flow dependent. The sheath becomes thin for the condition $R_e^{-1}\alpha^2 << 1$. The range of the parameters contained in Table 3-6 suggests that thick sheath conditions prevailed. It may be stated further that the thick sheath formula of Clements and Smy appeared to be even more applicable within the afterglow than within the active discharge. The static formula gave densities in the flowing afterglow which were more than an order of magnitude greater than those calculated within the discharge.

Electron densities are shown in Figure 3.10 for a discharge current of 2A, an initial fill of $CO_2/N_2/He$-4/4/6mm and two gas velocities of 35 and 70 m/sec. The kinetic formula has been used for the complete scan while the static formula was used only within the discharge. The formulas are presented in Appendix 3-1, together with the calculation procedure and an explanation of all symbols used. The computations were conducted under the following considerations:

(1) μ_i=200 cm^2 $volt^{-1}$ sec^{-1} as being typical of the ion mobilities,

(2) gas temperature and velocity variable through the zone of heat addition, as calculated from measured quantities; these corrections were of a minor nature,

(3) an average ion current was assumed within the discharge,

(4) The extent of the bars shown in Figure 3.10 was set by recalculating the densities with a change of ±20% in velocity and ±50% in ionic mobility,

(5) other parameters as given in Table 3-6.

The Clements and Smy theory gave peak densities of approximately 5 × 10^{11} per cm^3 while the Schulz and Brown theory was somewhat lower at approximately 2 × 10^{11} per cm^3. It is difficult to compare the calculated values of the present unconfined discharge with those determined experimentally by other investigators for a confined or tube discharge. As discussed at the beginning of this section these have been in the form of an average density measured by microwave techniques. Indications are that densities calculated by the kinetic

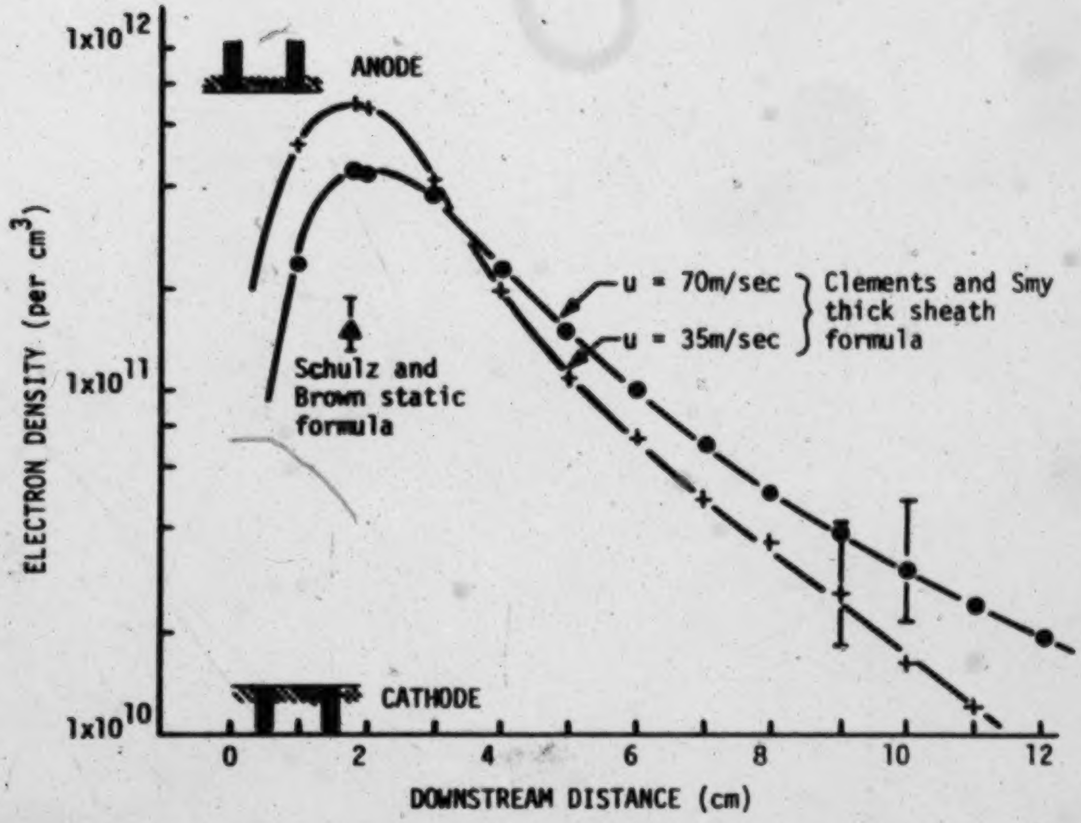

FIGURE 3.10. CALCULATED SPATIAL PROFILES OF THE ELECTRON DENSITY ALONG THE CHANNEL CENTERLINE IN THE DIRECTION OF FLOW.

Initial gas fill $CO_2/N_2/He$ - 4/4/6mm; I_D, 2A; μ_i approximately 200 cm^2/volt/sec; ion-current as given in Figure 3.9 with an average taken within the discharge; bars shown represent densities recalculated with a change of ±20% in gas velocity coupled with a ±50% change in ionic mobility.

formula were high. The cross-over of the two curves of differing velocity suggested that within the active discharge convection of ions to the probe did not completely dominate the collected ion current. Considerable uncertainty existed in the values of ionic mobility, ionic mean free path, and the ratio of the electron and ion temperatures. The kinetic formula is not particularly sensitive to mobility, $n_e \approx (1/\mu_i)^{1/2}$, and is not directly dependent on electron temperature. The static formula, on the other hand, is a strong function of the scattering factor, α_s, which in turn is a function of the ionic mean free path and the ratio of the electron and ion temperatures. The calculated mobilities are comparable to those determined experimentally for single component gases [72] [76]. The range of ±50% in ionic mobility, Figure 3.10, was based on these experimental values.

The "ripple" in electron pump along the laser axis at the peak of the ionization profiles was estimated to have risen to a value of 15% of the average density for a flow velocity of 70 m/sec and the conditions of Figure 3.9. The degree of flow turbulence is expected to have considerable influence on the lateral spreading or diffusion of the electron density and the vibrationally excited CO_2. Low flow ambipolar diffusion is augmented by turbulent diffusion for flows of high Reynold's number [77] thereby improving the uniformity of the active medium of a resonator placed within the flowing afterglow.

Summarizing briefly, the electron density was sampled by sweeping an electrostatic probe through the discharge. As expected the "structure" within the active discharge became more pronounced for higher flow. From calculated densities the pump ripple along the laser axis was estimated to be 15% of the average density for the highest flow investigated here (70m/sec). This structure disappeared rapidly in the flowing afterglow possibly as a result of turbulent diffusion introduced by the flow. A peak density of $2\text{-}5 \times 10^{11}$ cm^{-3} was calculated for a discharge current of 2A.

3.7 Experimental Spatial Small-Signal Gain Profiles

The small signal gain for various spatial positions was monitored by passing the beam from a low power oscillator (<0.5W in a fundamental mode diameter of 3mm operating on the P20 transition) through the cross-flow amplifying medium as shown in Figure 3.11. By collecting the test beam with a concave mirror and arranging the detector near the focus, the full laser aperture was probed by means of a two mirror scanner without moving the detector head. Scan position was monitored by precision potentiometers. This signal plus that from the detector was fed to an X-Y recorder giving a continuous read-out of the small signal amplification.

Typical horizontal-gain profiles are shown in Figure 3.12 for various vertical positions. As illustrated the discharge was established between two electrode rows, both anode and cathode, with a discharge current of 1.5A. The gas flow velocity was approximately 40 m/sec in a mixture of total pressure 20mm ($CO_2/N_2/He$-5.2/8.1/7.0mm). The small signal gain was rather insensitive to the gas mixture for high speed cross-flow. A ratio of N_2 to CO_2 of approximately 1.5 gave maximum gain for total pressures up to 30mm. The low proportion of He used for the data of Figure 3.12 reflects the fact that it appeared to have little effect on gain, contrary to the behavior observed for the

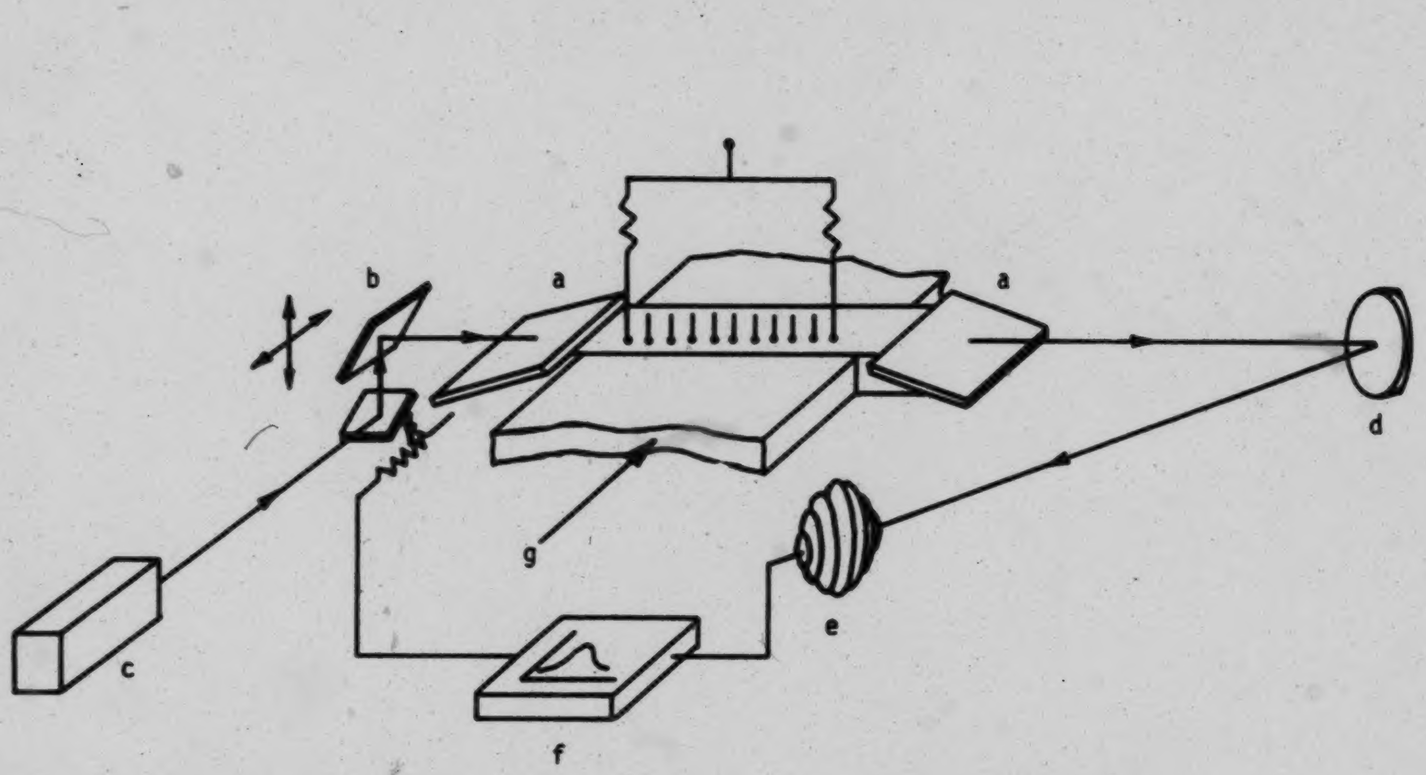

a- cross-flow laser with Brewster-angle windows
b- two mirror scanner
c- probe oscillator
d- spherical mirror
e- thermopile detector
f- X-Y recorder
g- gas flow

FIGURE 3.11. EXPERIMENTAL ARRANGEMENT FOR RECORDING SPATIAL GAIN PROFILES OF THE CROSS-FLOW LASER.

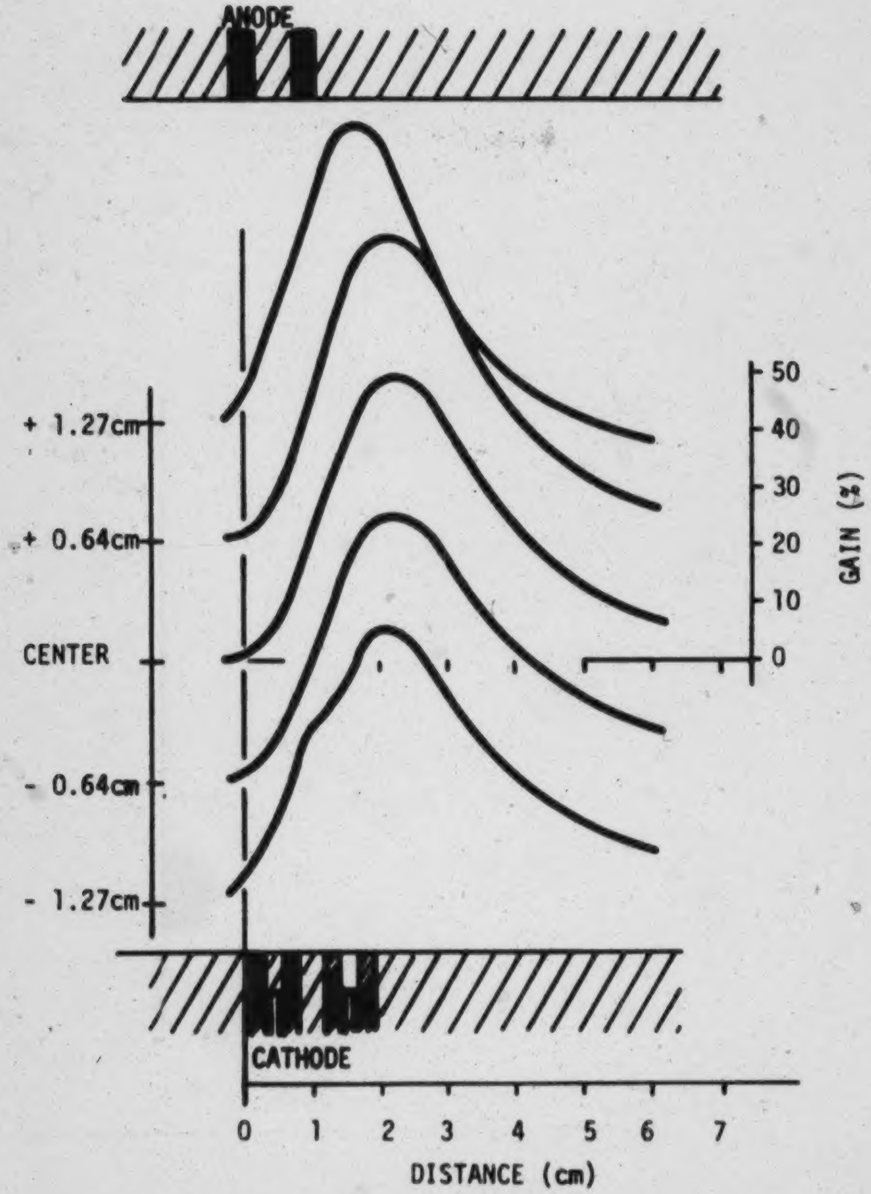

FIGURE 3.12. HORIZONTAL GAIN PROFILES.
$CO_2/N_2/He$ - 5.2/8.1/7.0mm; DISCHARGE CURRENT, 1.5A; DISCHARGE INPUT POWER, 2.3KW; GAS FLOW VELOCITY, 40m/sec; ANODE TO CATHODE DISTANCE = 3.8 cm; small-signal gain is defined as the ratio of the difference between probe oscillator power with and without an amplifying discharge to that without.

low axial flow of Chapter 2. This was interpreted as due to a lowering of the translational temperature by He in the conduction limited low flow case. The role of He in high speed cross-flow was expected to have a greater influence on output power, due to efficient relaxation of the CO_2 bending mode and thereby the lower laser level. CO, however, as a by product of CO_2 dissociation, also provided efficient lower level relaxation. Helium pressure became significant when sufficient energy was deposited in the gas that the upstream translational temperature rose. This suggested that the higher thermal conductivity of the gas mixture with added He provided more efficient cooling in the return circuit. Increasing the percentage of He was expected to raise the current at which the discharge contracted due to local gas heating. Helium was also expected to influence the lateral diffusion of vibrationally excited species within the discharge and flowing afterglow.

The decay of gain within the flowing afterglow was sensitive to the replacement gas flow rate. Little change was observed for a replacement rate above 1 to 2% of the channel mass flow rate and as a result the gain profiles were recorded using this small replacement flow. It was assumed that the "make-up" gas reduced the build-up of contaminants released from the electrodes and system walls and possibly discharge generated species.

Returning to Figure 3.12, the outer profiles had slightly higher peak gain and more rapid decay within the afterglow than the central scan for this particular discharge current. This reflected changes in the velocity, gas temperature, and electron density across the channel height. For higher input power the central gain rose above that close to the electrodes as shown in Figure 3.13 for a single pair of electrode rows.

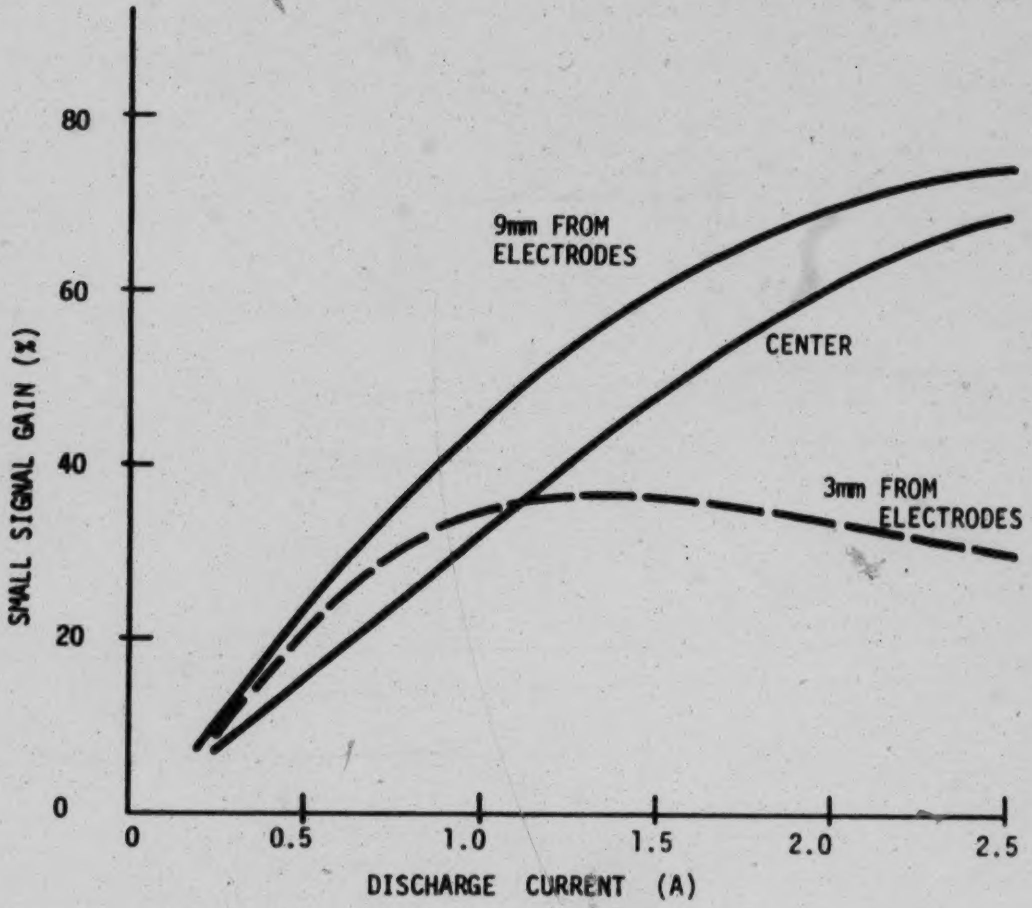

FIGURE 3.13. THE VARIATION OF SMALL-SIGNAL GAIN WITH DISCHARGE CURRENT FOR VARIOUS POSITIONS OF THE PROBE BEAM BETWEEN THE ELECTRODES.

Initial gas mixture, $CO_2/N_2/He$ - 3/4/4mm; gas flow velocity, u = 40 m/sec; one row of electrodes both anode and cathode as illustrated in Figure 3.2(b); probe oscillator operating on the P20 transition; beam diameter approximately 3mm.

The gas pressure and number of electrodes were reduced to more clearly show the saturation of gain with current. The gain obviously saturated at lower currents adjacent to the electrodes. Since the electron density was higher near the electrodes the effect of electron deactivation of the vibrations was expected to show up at lower discharge currents. In addition gas heating was expected to be higher with the transition of the discharge through the boundary layer.

The variation of small-signal gain with mass flow rate is shown in Figure 3.14. The gain was scanned along the channel center for a discharge current of 2A and a total pressure of 14mm(CO_2/N_2/He - 4/4/6mm). The peak gain coefficient rose rapidly to approximately 1.5% per cm for low flows and the active medium expanded in the direction of flow due to convection and a lowering of the translational temperature. For very low flow the active medium was sufficiently narrow that the finite width of the probe beam and alignment broadened the recorded gain peak.

For a given discharge width and current, a velocity was reached for which the gas residence time did not allow the gain to rise to its equilibrium or saturated value, as shown by the 75 m/sec profile, Figure 3.14. Although the peak gain was reduced past a certain velocity, the rate of transfer of vibrationally excited CO_2 into the flowing afterglow increased. Consequently the area under the gain profile tended to remain constant. Of course, as the velocity was raised to bring the gain out of current saturation the input power could be raised to provide approximately the same peak gain.

The variation of small-signal gain with discharge current is illustrated in Figure 3.15 for different flow rates. Since the peak shifted upstream with current, the probe beam was positioned at maximum

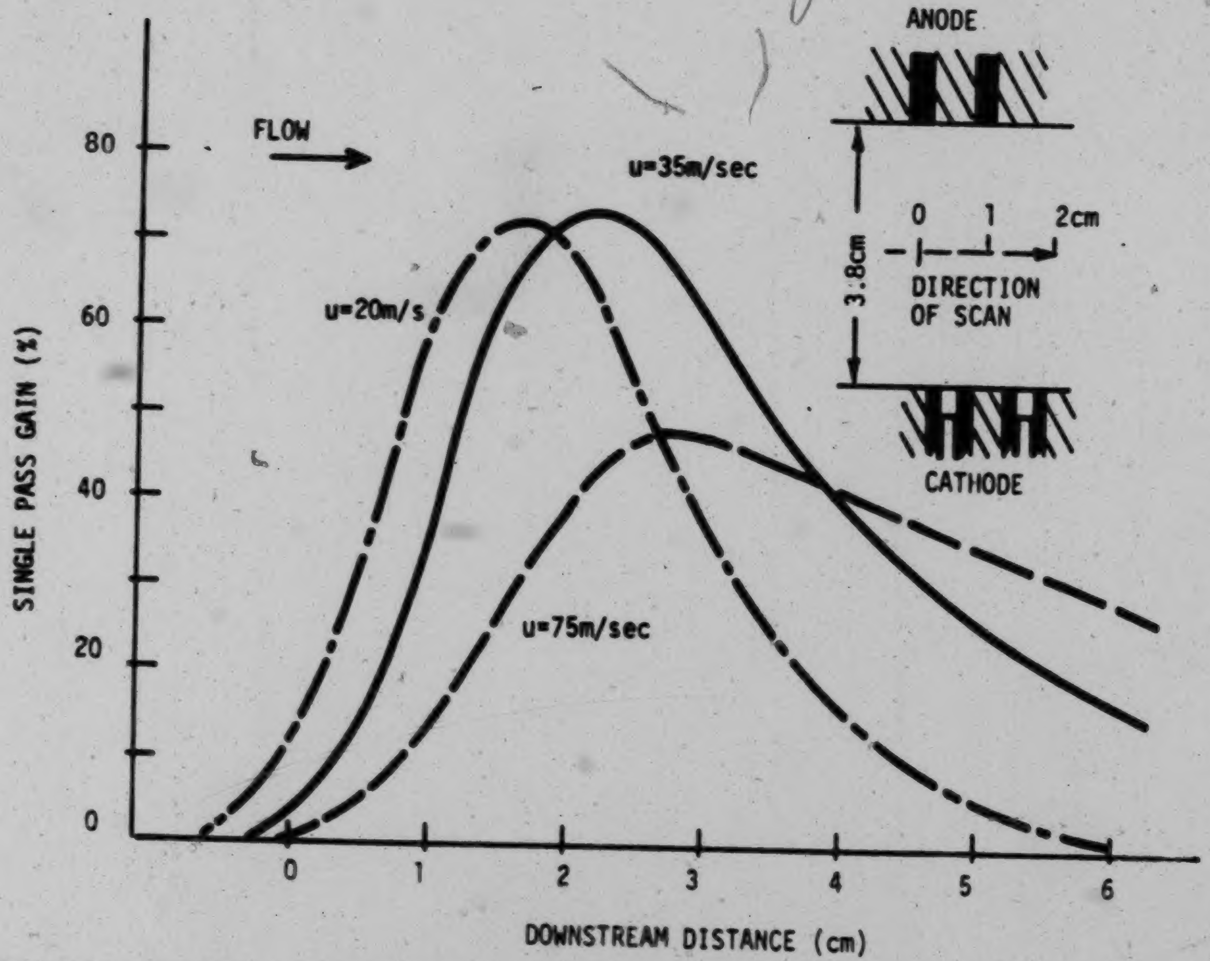

FIGURE 3.14. THE SPATIAL VARIATION OF SMALL-SIGNAL GAIN WITH GAS FLOW VELOCITY. Initial gas mixture, $CO_2/N_2/He$-4/4/6mm; discharge current, 2A; mass flow approximately 0.011, 0.02, .043 lbm/sec for 20, 35, 75 m/sec respectively; probe oscillator operating on the P20 transition; gas velocity measured on channel centerline.

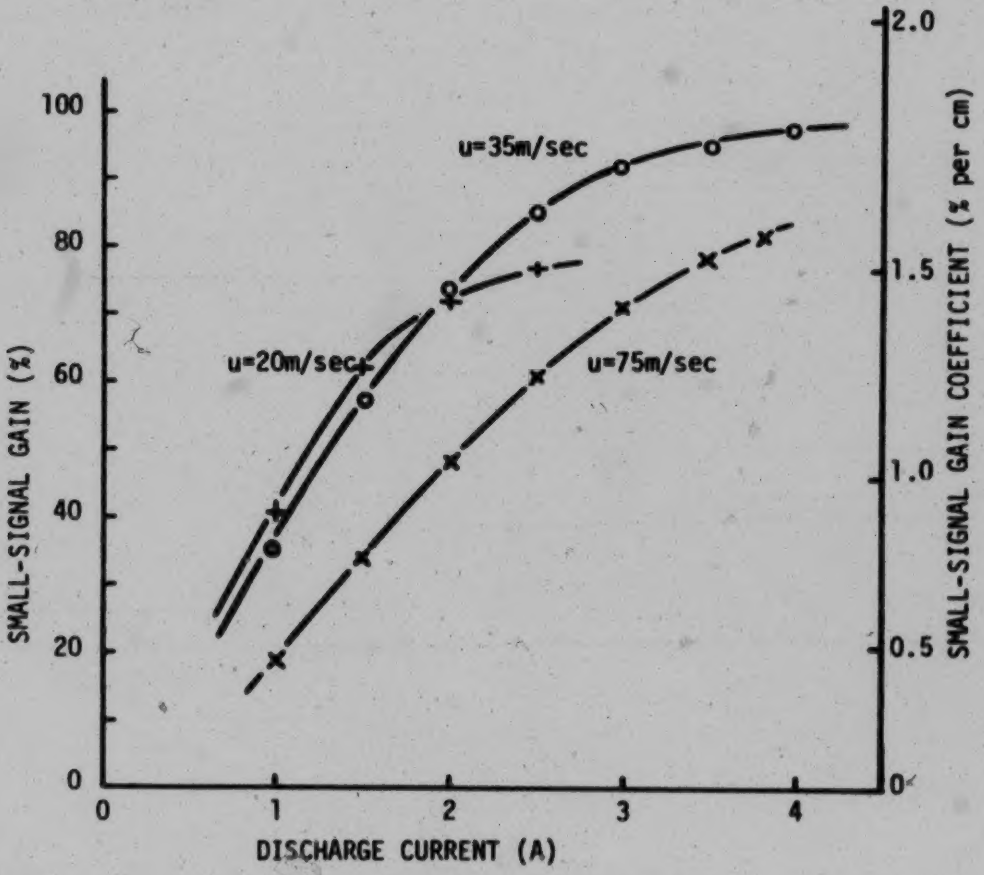

FIGURE 3.15. THE VARIATION OF SMALL-SIGNAL GAIN WITH DISCHARGE CURRENT FOR VARIOUS FLOW RATES.

Initial gas mixture, $CO_2/N_2/He$-4/4/6mm; two electrode rows both anode and cathode as illustrated in Figure 3.14; P20 transition; probe oscillator beam midway between the electrodes at position of the spatial gain peak.

gain for each discharge current. The gains plotted in Figure 3.15 were obtained along the channel center. The maximum small-signal gain coefficient observed, was in the order of 2% per cm. For low flow the gain was assumed to have been temperature limited. As the flow was raised up to 30 m/sec the rise in saturated gain became less pronounced, although the current at which saturation did occur continued to increase. As shown in Figure 3.13 and demonstrated by the experiments of Buczek et al [78], once the gain had saturated, it declined only slowly with further raising of the current. Supported by the calculations of section 3.8, the form of the gain curves was due to the combined effect of gas heating and deactivation of vibrational energy by electrons. The maximum gain for a given velocity was controlled by collisions of the second kind with electrons. The increase of maximum gain with velocity was attributed to a lowering of the translational temperature by convective cooling.

Having discussed the experimental observations of gain in the above paragraphs attention is now turned to a comparison with theoretical computations.

3.8 Comparison of Theoretical and Experimental Small-Signal Gains

One of the first considerations was the choice of an analytic function to represent the spatial variation of electron energy and density through the glow discharge. The electron density profile was analyzed in section 3.6. The average electron energy was expected to have a quite different form. Within the flowing afterglow relaxation of the average electron energy was expected to be influenced by collisions of the second kind as recent experiments of

Sahni and Jennings suggest [79]. The present analysis was simplified, however, by assuming that the relaxation distance was short. This was based primarily on the fact that afterglow gain and translational temperature could be simulated by heavy particle collisions alone.

From the calculations of reference [35] the excitation rates are not expected to be a strong function of electron energy above approximately 0.5eV. The effect of the spatial variation of electron energy in the central region of the discharge may, therefore, be lessened by this fact.

The effective pump profile was taken as the difference between electron excitation and deactivation. The pump term for each vibrational species was simplified to the product of the peak electron density, $n_e(z_p)$, the neutral number density, N_s, of species s, the effective vibrational excitation rate $K_{ois}(z_p)$ of mode i of species s, and an assumed pump function, $f_{ep}(z)$, representing the combined spatial variation of n_e and K_{ois}. The deactivation term was similar with K_{ois} replaced by the effective rate for collisions of the second kind, K_{ios}, and N_s replaced by the population density, N_i, of the vibrational modes, i. The pump for the CO_2 asymmetric mode was further simplified by the assumption that the asymmetric mode was in equilibrium, at vibrational temperature T_3, with the modes of N_2 and CO. This led to the following expression for the effective electron pump.

$$n_e(z_p)\ f_{ep}(z)\ K'_{03}\left[1-K_R\exp(-3380/T_3)\right]$$

K'_{03} - the effective excitation rate for a particular gas mixture

K'_{30} - the effective deactivation rate

K_R - the electron excitation-deactivation ratio

$= K'_{30}/K'_{03}$

To provide an electron pump of various shapes, f_{ep} was divided into the following branches,

$$f_{ep}(z \le z_m) = f_m\left(\frac{z}{z_m}\right)^2$$

$$f_{ep}(z > z_m) = 1 + (f_m - 1)\left(\frac{z - z_p}{z_m - z_p}\right)^2$$

$$f_{ep}(z > z_o) = 0$$

The above equations introduce essentially a parabolic spatial distribution about the point of peak electron density, where z represents distance in the direction of flow; z_m, the function matching point; z_p, the position of peak electron density; z_o, the point at which $f_{ep}(z)$ becomes negative and f_m, the ratio of the electron density-excitation product at the matching point and the peak.

Computations were conducted with a constant dissociation fraction of $\delta = 0.3$ (section 3.3.3). The use of constant δ for varying discharge current, I_D, and flow velocity, u, was justified by the following reasoning. Although the dissociation reaction is reversible, the relatively long equilibration time suggested that once equilibrium had been established at a given I_D and u, very little variation of composition occurred through the discharge. From the work of

Gasilevich et al [80], δ was expected to rise slowly with I_D. Likewise, δ was expected to rise with u as a result of increasing electron energy with charged-particle loss. This is equivalent to a reduction of the tube diameter of a confined discharge [80]. Since E/N rose slowly with u, this effect was assumed to be of low order.

3.8.1 Calculated gain profiles

The above pump profile was combined with the energy balance and gas dynamic equations of section 3.2 to compute the small-signal gain. The equations were solved numerically by an IBM 360-APL computer program employing the Hamming predictor-corrector method [81].

Initially gain profiles were produced with the bending and symmetric modes in equilibrium with each other but not with translation. The vibrational temperature, T_2, of these modes, however, did not rise appreciably above the translational temperature, T. In addition, electron pumping of the bending and symmetric modes did not appear to be significant for the rates given by reference [35]. This is consistent with the findings of reference [21]. On the basis of these observations and the experimental results of reference [36], the electron deactivation process was simplified to a direct relaxation into translation.

The computerized simulations employed the experimentally measured parameters of gas flow velocity, mixture, and pressure, and electron density with accepted heavy particle relaxation rates (section 3.2.2) and the above electron pump profile. Electron excitation and deactivation rates were adjusted to reproduce the experimental gain and translational temperature. In view of the various approximations, results were expected to be only of a semi-quantitative nature. Computations did strongly indicate, however, that a substantial electron relaxation rate was necessary in the present model to explain observed experimental data. The ratio of the downward to upward rates was expressed by the parameter K_R. K_R was chosen so that the calculated saturation of gain with n_e approximated the experimental variation of gain with I_D. Values of K_R were typically in the range 5 to 10. A factor of 5 less than experiments of reference [36]. The stimulated emission cross-section, X_R, was calculated with a constant collision cross-section for rotational relaxation. For the gas pressures used in this thesis, the laser line is both homogeneously and Doppler broadened. X_R had values of approximately $4 \times 10^{-18} cm^2$ at $T=300^0K$, for the P20 transition, decreasing to near $3.5 \times 10^{-18} cm^2$ at $T=500^0K$.

Typical computed profiles of gain and translational temperature are presented in Figure 3.16, for the following conditions:

1. initial gas mixture $CO_2/N_2/He$ - 4/4/6mm
2. dissociation fraction, $\delta=0.3$
3. total operating pressure (discharge ignited), p=15.4mm
4. total discharge current, $I_D=2A$
5. center-line flow velocity downstream from discharge as indicated in Figures 3.16 (a) and (b)
6. electron density - effective excitation rate product, $n_e K'_{03}$, at peak pump =570 sec^{-1} per CO_2 molecule
7. electron deactivation - excitation ratio, $K_R=6$
8. heavy particle relaxations rates and temperature dependence as given in section 3.2.2

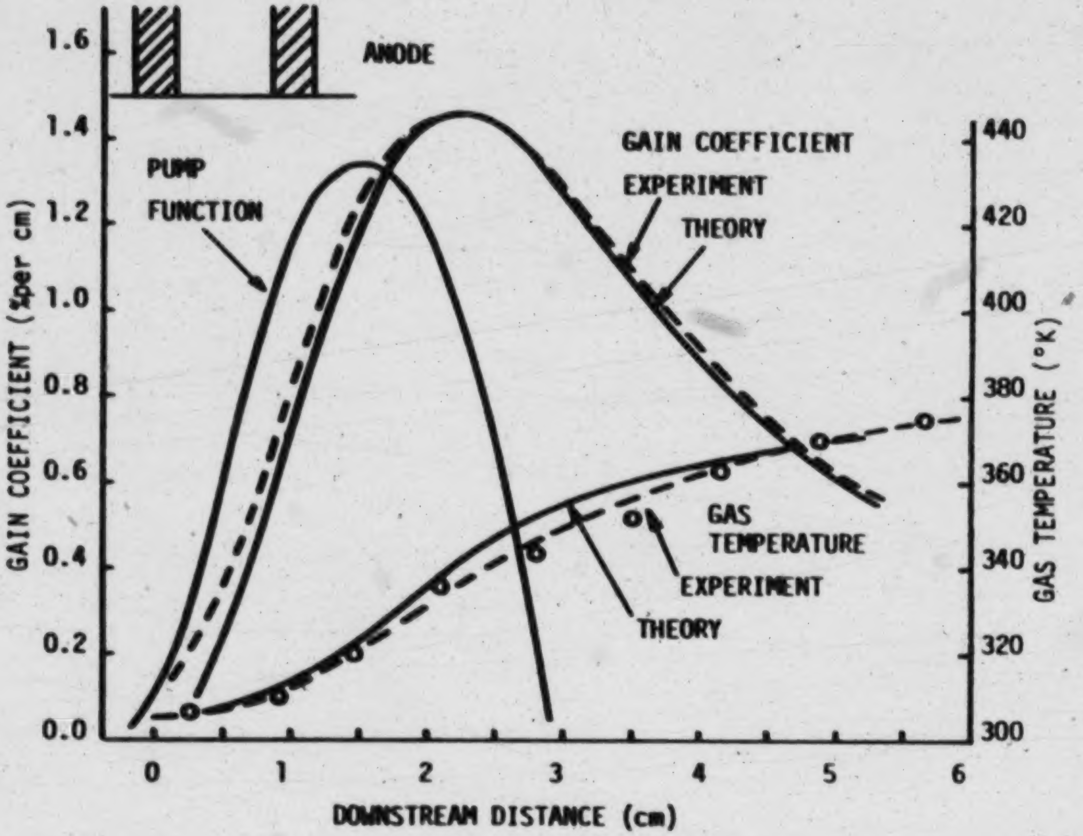

FIGURE 3.16(a). CALCULATED SMALL-SIGNAL GAIN COEFFICIENT AND TRANSLATIONAL TEMPERATURE COMPARED WITH EXPERIMENT FOR A CENTERLINE FLOW VELOCITY OF 35m/sec.

Initial gas mixture, $CO_2/N_2/He$ - 4/4/6mm; δ=0.3; u(z=3.75 cm), 35m/sec; experimental I_D, 2A; two row multi-electrode arrangement as outlined in Tables 3-3 and 3-4; 33mA per electrode pair; theoretical curves computed with the peak product of electron density and effective excitation rate equal to 570 sec^{-1}; K_R, 6; X_R(z=0), 4.08 x 10^{-18} cm^2 and X_R(z=5), 3.85 x 10^{-18} cm^2; heavy particle relaxation rates as given in section 3.2.2.

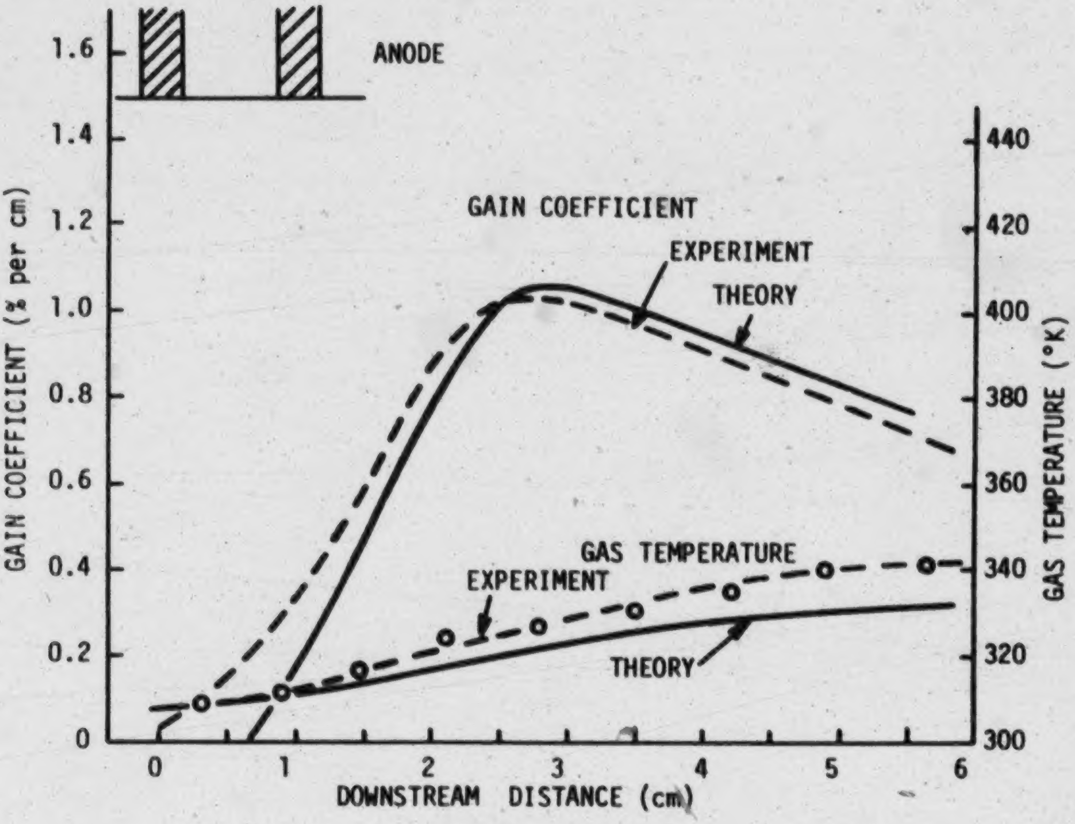

FIGURE 3.16(b). COMPUTED GAIN COEFFICIENT AND TRANSLATIONAL TEMPERATURE COMPARED WITH EXPERIMENT FOR A CENTERLINE FLOW VELOCITY OF APPROXIMATELY 75m/sec. Conditions are as outlined in Figure 3.16(a) except for the following: u(z=3.75cm),≈75m/sec; X_R(z=0cm),4.04x10^{-18}cm^2 and X_R(z=5cm),3.97x10^{-18}cm^2 for the P20 transition.

The electron pump function, f_{ep}, is shown in Figure 3.16(a). The entering gas velocity used in the program was adjusted to reproduce approximately the experimental value at its point of measurement. The flow velocity increased through the discharge and afterglow by approximately 5m/sec in Figure 3.16(a), for example. As shown in Figure 3.16(a), for u=35m/sec, both gain and translational temperature were closely simulated for the parameters listed above. Using the parameters of Figure 3.16(a) the predicted gain for u=75m/sec, Figure 3.16(b), showed close agreement with experiment. The translational temperature, however, was a few degrees low. By maintaining the parameters of Figure 3.16 and changing only the flow rate experimental gains and temperatures were closely reproduced over a velocity range of at least four, that is over the range of experimental data.

Figure 3.16 was produced with a peak electron density - effective excitation product of 570 sec^{-1} per CO_2 molecule, for the CO_2 asymmetric mode. From section 3.6, peak electron density corresponded to approximately $5 \times 10^{11} cm^{-3}$ at an I_D of 2A. This gave an effective excitation rate of $1.14 \times 10^{-9} cm^3\ sec^{-1}$ which is a factor of 40 less than the calculated rate of reference [35]. This rather poor agreement may be explained by a difference in gas mixtures, discharge generated impurities in the closed cycle flow, and particularly an overestimation of the electron density. By using the calculated excitation rate, an electron density near $10^{10} cm^{-3}$ was predicted. This compares more closely with experimentally measured values [63].

Figure 3.17 illustrates the calculated variation of peak small-signal gain with the peak effective excitation product, $n_e K'_{03}$. Comparison is made with experiment on the basis of a linear relationship between discharge current and peak electron density.

?

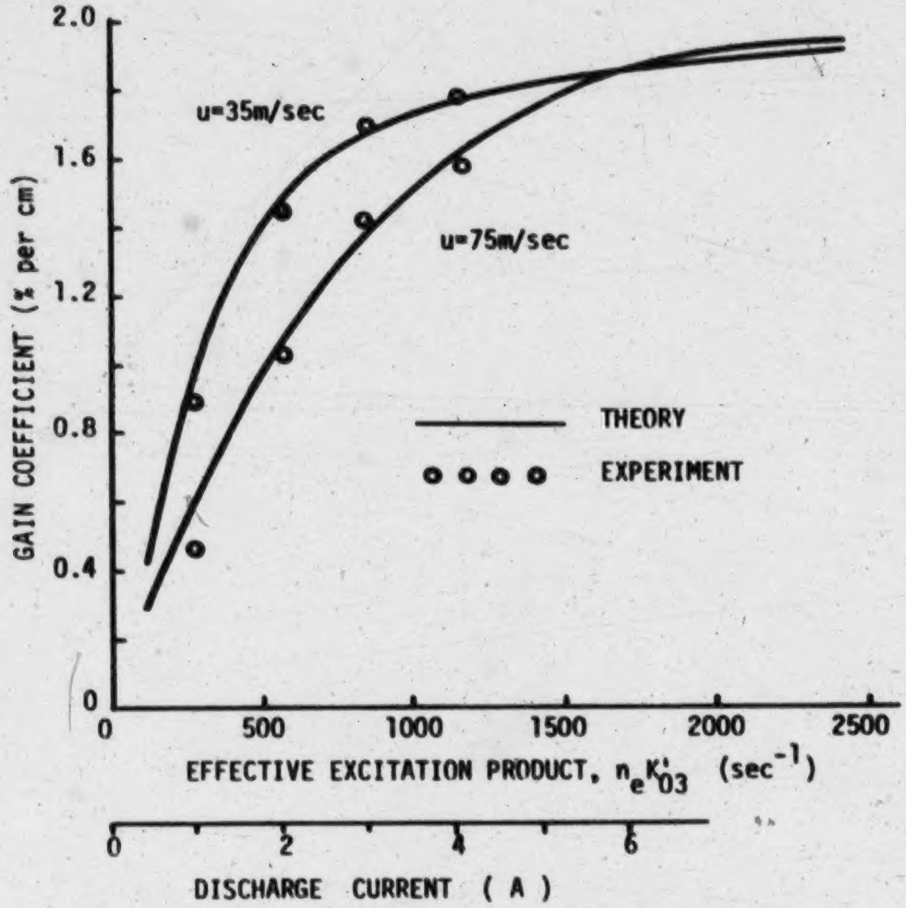

FIGURE 3.17. CALCULATED SMALL-SIGNAL GAIN COEFFICIENT AS A FUNCTION OF THE EFFECTIVE EXCITATION PRODUCT AT THE SPATIAL PEAK OF THE ELECTRON PUMP. Initial gas mixture, $CO_2/N_2/He$ - 4/4/6mm; δ=0.3; two multi-electrode rows both anode and cathode as outlined in Tables 3-3 and 3-4; electron deactivation-excitation ratio, K_R=6; experimental points are plotted against the total experimental discharge current.

K_R again has the value six. Likewise other parameters were unchanged from Figure 3.16. In fact plots such as those of Figure 3.17 assisted in the choice of K_R, since the magnitude of K_R controlled the saturation of gain with current. The peak gains of previous Figure 3.16 represent two points on Figure 3.17. Experimental data is shown, for this gas mixture up to the point of saturation. By referring to the experimental curves of Figure 3.13, section 3.7, and other experimental observation also at lower gas pressure, peak gain declined only slowly once saturated. This is consistent with the work of Buczek [78]. This effect is somewhat misleading in that although the peak gain remained high over a large current range, the average gain decreased rapidly at high current. This resulted from the fact that the gain peak moved upstream with I_D while high gas temperature severely limited gain in the flowing afterglow.

Consistent with experiment, the peak gain saturated at higher I_D for increased flow rate, with the magnitude being essentially independent of velocity above approximately 20m/sec. For lesser values, saturated gain was reduced by thermal heating. This velocity dependence appears to differ somewhat from that of Buczek [78]. The saturated gain of reference [78] continued to rise to higher values over the full range of velocity investigation, 50m/sec. A possible explanation lies in that the two discharges may have been operating in different regimes. As outlined in section 3.4.1 the transverse discharge of this thesis showed bowing in the direction of flow only at velocities less than 10m/sec. This flexing was explained on the basis of a low density high temperature core which disappeared above approximately

10m/sec. The geometric arrangement and flexural properties demonstrated in reference [78] suggest that a low density high temperature core persisted to high gas velocities giving thermal effects on the saturated gain that were only observed at relatively low flow rates in this thesis.

Figure 3.18 shows the predicted peak gain as a function of gas velocity using the above parameters for an I_D of 2A. Experimental data is also shown. The calculated curves follow closely the experimentally points. The benefit of convective flow is clearly demonstrated. Gain shows a rapid rise at low flow, peaks out in the 20 to 40 m/sec range and then gradually declines. The shape of the curve is readily explained by recalling that this case represents essentially constant input power to a short (in the direction of flow) discharge width. In the absence of thermal heating and current saturation, peak gain is expected to be inversely proportional to u. With thermal heating and low velocity, the slope is positive as heat is removed by convection. A velocity is reached, however, at which the peak gain is governed by the discharge residence time resulting in a negative slope. Current saturation had the effect of broadening the maximum of Figure 3.18 and displacing the negative characteristic to higher velocities, as expected.

The above paragraphs have outlined the results of an analysis employing energy balance and gas dynamic equations to predict small-signal gain and gas temperature. A substantial electron deactivation rate was found necessary in the simulations of experimental data. The values of K_R so deduced were consistent with limited published data.

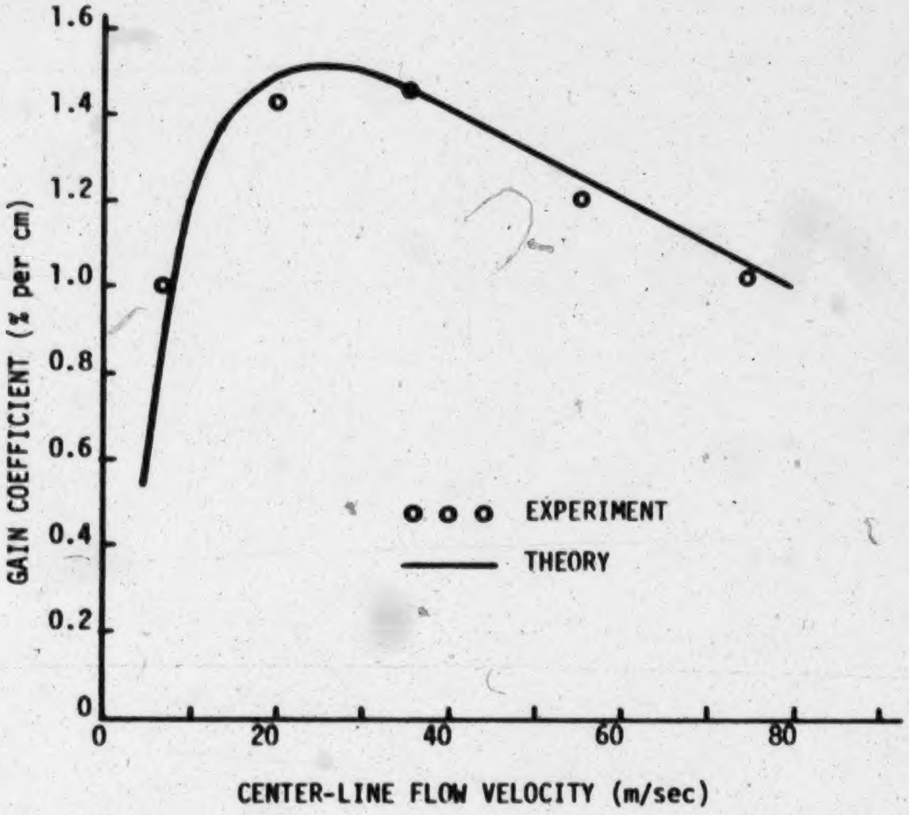

FIGURE 3.18. THE VARIATION OF THE CALCULATED SMALL-SIGNAL GAIN COEFFICIENT WITH CENTER-LINE GAS VELOCITY FOR CONSTANT DISCHARGE CURRENT.

Initial gas mixture, $CO_2/N_2/He$-4/4/6mm; δ=0.3; experimental I_D, 2A; two multi-electrode rows both anode and cathode; $n_e K'_{03}$ for theoretical curve, 570 sec^{-1}; K_R, 6.

Good agreement was found with experiment in the predictions of the variation of gain and gas temperature with flow velocity. An effective vibrational excitation rate was estimated, however, poor agreement was found with a theoretically expected rate. This may have been aggravated by errors in the experimental electron density, use of a gas mixture different from the theoretical calculations and discharge generated impurities.

3.9 Laser Output Power

3.9.1 *Resonator Design*

Several resonator configurations were tested; these included single and multiple pass *stable* arrangements and a positive branch *unstable* configuration, Figure 3.19, similar to that of Krupke and Sooy [82].

Both external and internal resonators were used. In the external case, however, the intracavity NaCl windows were subjected to high intensities which caused *cross-hatched* patterns to appear [83]. For the unstable resonator this cross-hatching caused the mode quality to deteriorate to such an extent that a near-field annulus of uniform intensity was no longer obtainable. The unstable resonator was placed internally with the output beam coupled from the system by an NaCl flat at the Brewster-angle. The NaCl was then subjected only to the much lower output intensities and appeared to have little influence over mode quality.

In order to couple effectively to the active medium, a resonator of high Fresnel number, N ≈ 40, was required. For the stable resonator, this produced a high-order rectangular mode, such that the intensity appeared almost uniform across the beam width. For mode stability the lowest order transverse mode is desired. For the stable case this corresponded to a mode volume small relative to that of the active medium. The large lowest-order mode of the unstable case, however, can be more easily matched to the active medium. With this consideration and to avoid thermal-runaway problems associated with germanium output mirrors, an unstable resonator was built using only reflective optics. A

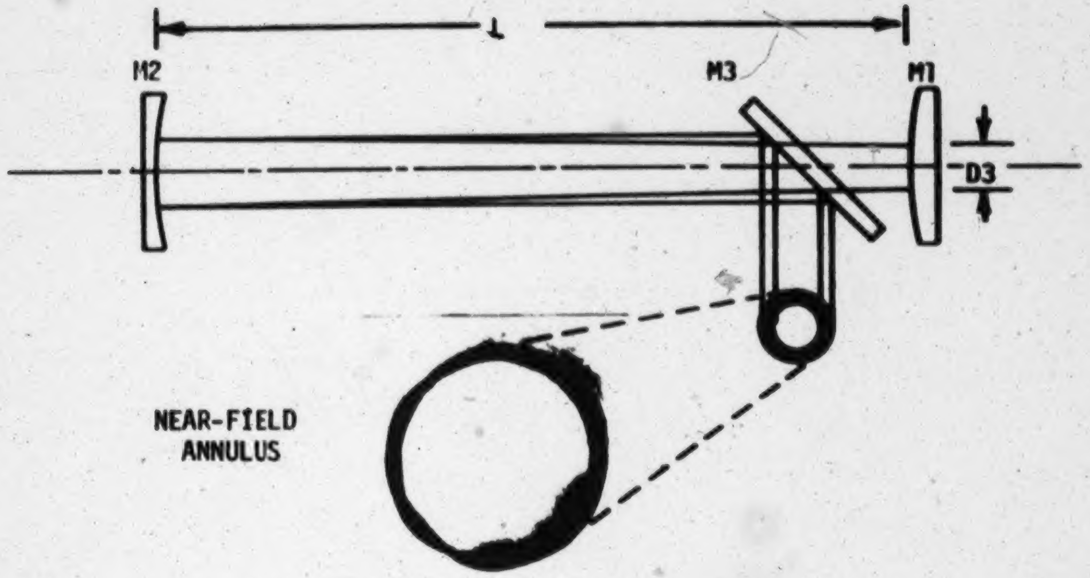

FIGURE 3.19. SCHEMATIC OF THE UNSTABLE RESONATOR. The near-field annulus was recorded by inserting a white card into the output beam approximately 30cm from M3. Active medium between 5 anode and 4 cathode electrode rows; total gas pressure 28mm; $CO_2/N_2/He$-4/9/15mm;u=40m/sec.

TABLE 3-9

UNSTABLE RESONATOR PARAMETERS

R_1 = -16.5m $\quad$ R_2 = 21.5m

$g_1 = 1-L/R_1$ $\quad$ $g_2 = 1-L/R_2$

= 1.0667 $\quad$ = 0.9488

M = 1.255 = round-trip magnification

δ = 0.14 = output coupling fraction

L = 1.1m = resonator length

D_3 = 0.025m = hole diameter of output coupler collimated output was desired but since the resonator was constructed using an existing concave mirror, a slightly divergent system was designed, Table 3-9. The calculation procedure, as presented in Appendix 3-2, follows that of Siegman [84]. The fundamental mode of an unstable resonator is an annulus of uniform intensity in the near field. The near field mode pattern, shown in Figure 3.19, was recorded on a piece of heavy white paper with a short exposure to the beam. For a collimated beam the far-field pattern contains a main central lobe with concentric rings; likewise, the focussed spot from a divergent configuration [84].

Stainless steel optics were used for all reflection components of the various resonators. These were coated with an evaporated layer of gold or silver. Since alignment tolerances are small for both the unstable and multiple-path stable configurations, mirror mounts were designed with adjusting screws of 80 threads per inch. Also, on the suggestion of reference [84], the interior of the output coupling hole was ground smooth, so that the edge was free of "nicks".

3.9.2 *Laser Power at* 10.6μ

First, the benefits of convective cooling are illustrated by comparing the laser power with and without convective flow. Figure 3.20 gives the laser power as a function of input power to the discharge for externally coupled resonators. A single path active medium extending 38cm along the laser axis was generated between two electrode rows for both anode and cathode. The replacement or make-up gas rate was approximately 1% of the channel mass flow rate. With no cross-flow, curve A, a maximum single path output of 11 W was obtained at an input

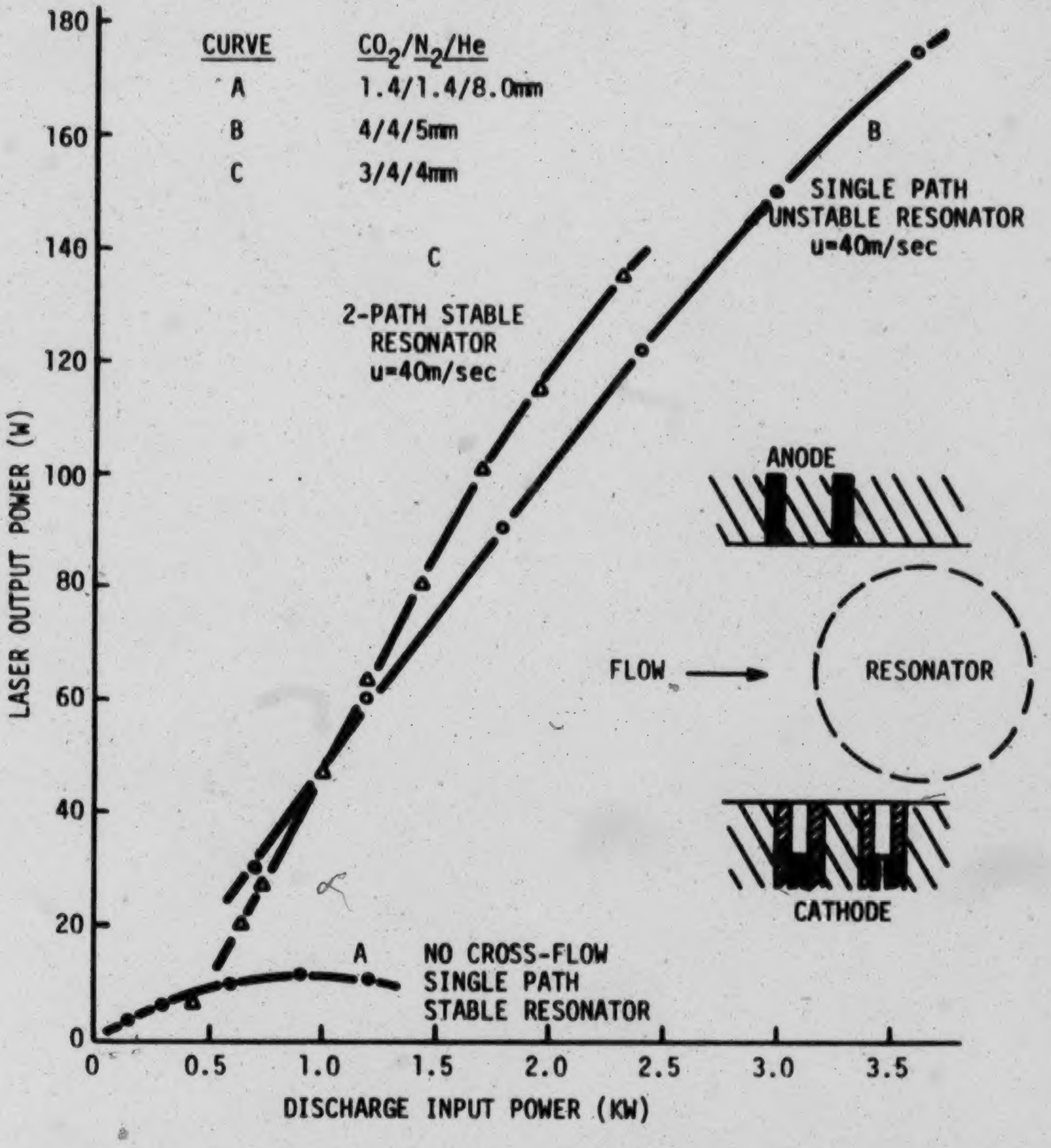

FIGURE 3.20. LASER POWER VERSUS ELECTRICAL INPUT POWER FOR VARIOUS EXTERNALLY COUPLED RESONATORS AND FLOW CONDITIONS. Single-path active medium of 38cm; anode and cathode of two multi-electrode rows each as outlined in Tables 3-3 and 3-4; resonator details as outlined below.

Curve A; Output δ of 0.1 through a coated NaCl flat; 21.5mR concave mirror; resonator length, L=80 cm.

Curve B; Resonator outlined in Figure 3-19 and Table 3-9.

Curve C; Stainless steel flat; intermediate 21.5mR concave mirror; Ge output flat (δ=0.23); L=2m.

of 1 KW. The output was a strong function of gas pressure and the constituents. The partial pressure of He, by virtue of its high thermal conductivity, had a strong influence on output. Curves B and C demonstrate the great improvement in both volumetric and electrical conversion efficiency to be gained through convective cooling. Curve B gives the output with a flow velocity of 40 m/sec for a single path unstable resonator. For comparison curve C was obtained for a folded 2-path stable configuration. Both B and C show more than an order of magnitude improvement in laser output. For instance, 175 W was obtained for the unstable resonator at an input of 3.5 KW compared to a maximum of 11 W at 1 KW for no cross-flow. The gas composition and overall gas pressure were less critical for convective flow, with the role of He being greatly reduced at low input powers.

For the above case, the two electrode rows did not generate an active medium to fill the resonator mode volume uniformly. The unstable resonator mode was annular but not of uniform intensity. Upon expansion of the active medium, mode quality improved but was still degraded by the internal windows. An annular mode of near uniform intensity, Figure 3.19, was produced when the mirrors were mounted internally. Note that the burn pattern of Figure 3.19 was obtained for a total operating pressure of 28mm. Even more uniform patterns were observed at lower gas pressures.

The variation of output power with flow velocity is illustrated in Figure 3.21. The data were collected at constant discharge current through an active medium expanded to five rows of anode electrodes and four cathode rows. The resonator consisted of a two-path stable

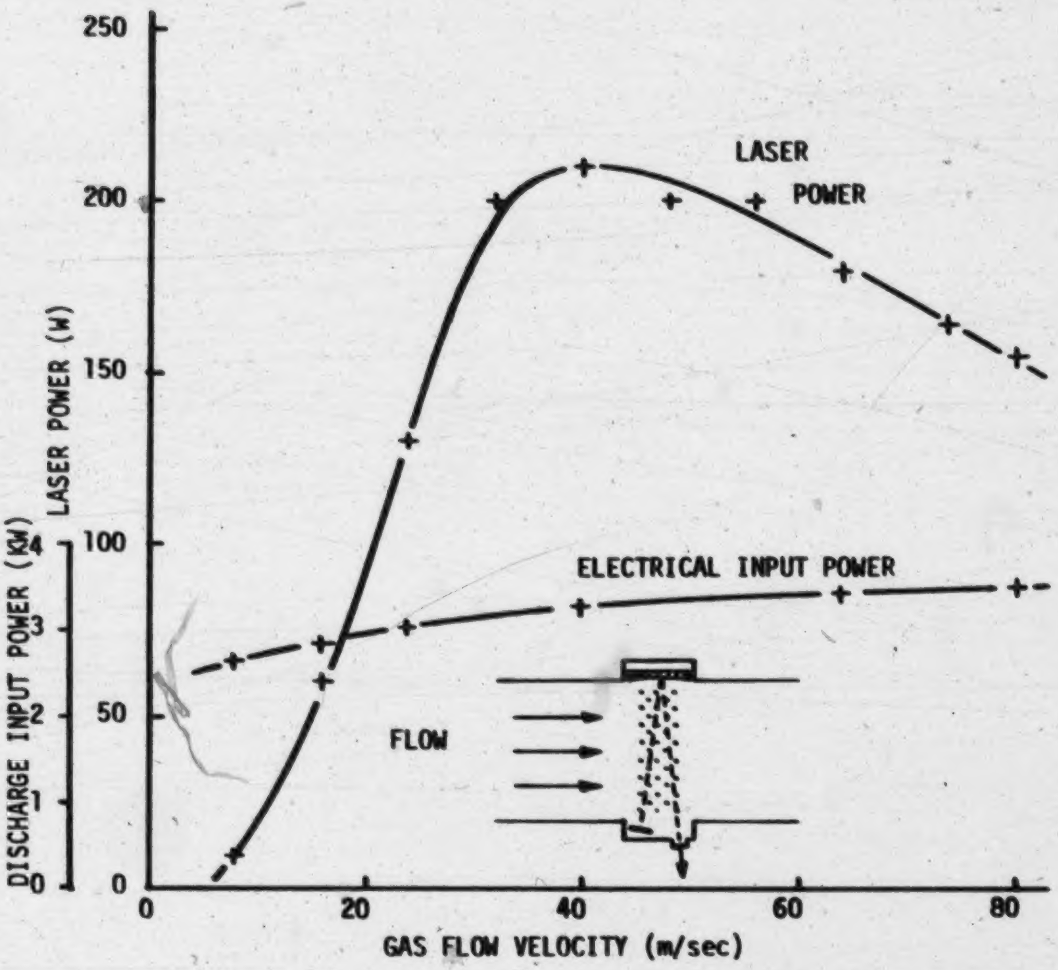

FIGURE 3.21 MULTIMODE LASER POWER AS A FUNCTION OF FLOW VELOCITY FOR CONSTANT DISCHARGE CURRENT.

Initial gas mixture, $CO_2/N_2/He$ - 4/6/15mm; I_D, 3A; 5 anode rows and 4 cathode rows as illustrated in Figure 3.3; internal double path stable resonator consisting of a stainless steel flat, an intermediate stainless steel spherical mirror of 21.5mR, and a water-cooled output flat of Ge.

arrangement outlined in Figure 3.21. Laser power increased steeply up to 30 m/sec as heat was convected from the laser region. In the range 30 to 60 m/sec output was rather insensitive to flow indicating that translational temperature effects had been alleviated. For velocities past 60 m/sec laser power declined. This appeared to be associated with a gradual mismatching of the active medium and the resonator. Although the electrical discharge showed little movement in the direction of flow, the active medium moved downstream as illustrated by the gain scans of Figure 3.14, section 3.7. In other words, optimum resonator position shifted downstream with velocity, as expected. The relatively short channel aperture did not permit investigation of laser power from a resonator located downstream from the discharge. Some power reduction may have been associated with structure in the active medium generated by the segmented electrodes. For higher velocities structure persisted for longer distances as verified by the electron density measurements of section 3.6. Consequently to maintain a certain uniformity of active medium the resonator shifted in the direction of flow.

The lower curve of Figure 3.21, gives the increase of input power with velocity for constant discharge current. The initial rise was attributed to increased gas density as the translational temperature was lowered by convective cooling. As previously discussed in section 3.4.2 the more gradual slope past 30 m/sec was attributed to convective charged-particle loss from the plasma.

The laser output versus discharge input power is given in Figure 3.22 for the expanded active medium. The data were obtained for the 2-path stable resonator of Figure 3.21. The optimum alignment was

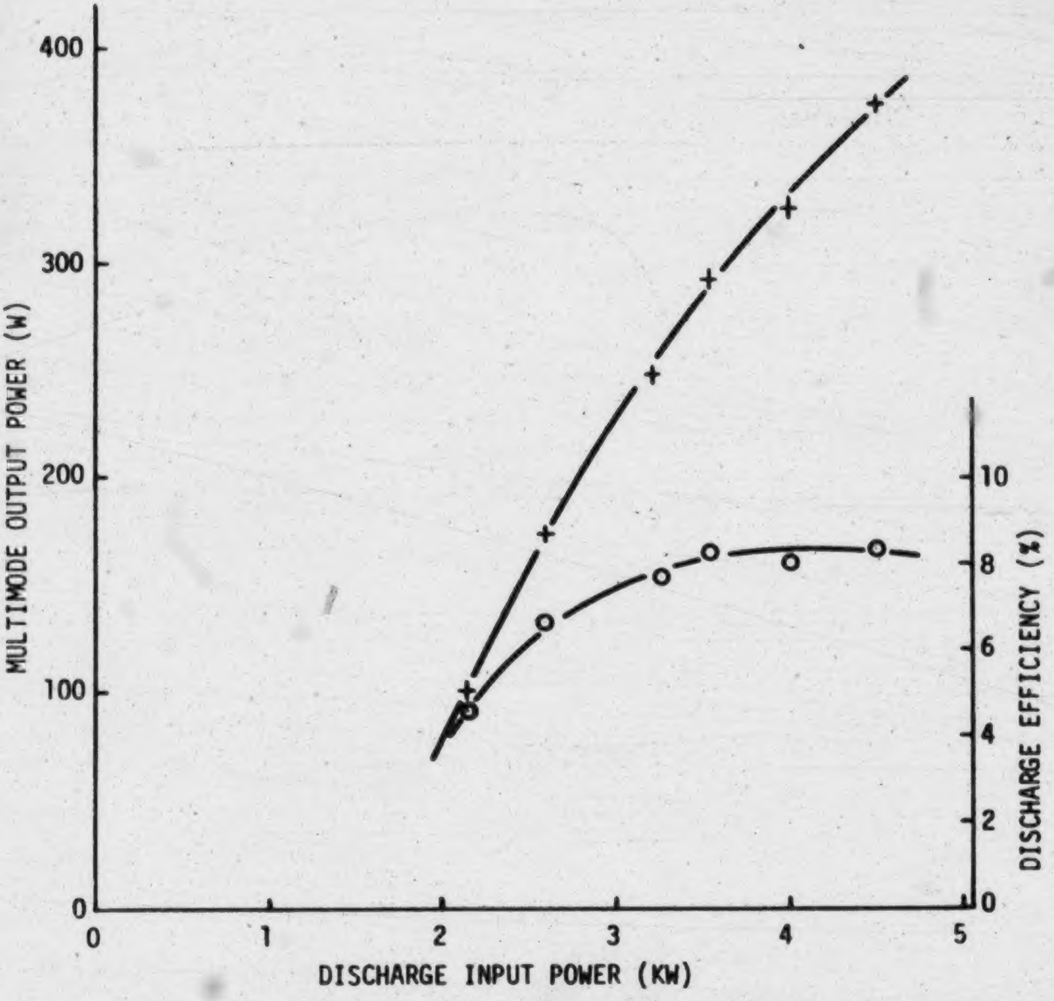

FIGURE 3.22. LASER POWER AND EFFICIENCY VERSUS DISCHARGE INPUT POWER FOR AN INTERNAL TWO-PATH RESONATOR.

Initial gas mixture, $CO_2/N_2/He$ - 4/6/15mm; u, 40m/sec; mass flow approximately 0.029 lbm/sec; 5 anode rows and 4 cathode rows as illustrated in Figure 3.3; internal double path resonator consisting of a gold-surfaced stainless steel flat, an intermediate gold-surfaced stainless steel spherical mirror (21.5mR) and a water-cooled Ge output flat; efficiency is based on the electrical power dissipated in the glow discharge.

sought for an optimum mixture of $CO_2/N_2/He$-4/6/15mm and flow velocity of 40 m/sec. The output coupling, however, was not optimized. The highest laser power was near 400 W with a discharge conversion efficiency of greater than 8%. The overall efficiency, including power dissipated in the glow discharge, the ballast, and the compressor motor, was approximately 5%. For the data of Figure 3.22, the compressor speed was 5000 RPM with an electrical input to the motor of 0.5 KW representing approximately 5% of the total input to the system at maximum laser power.

The loading of the discharge is characterized by discharge specific power defined as the ratio of the discharge input power and the mass flow rate. The mass flow rate for Figure 3.22 was calculated as 0.013 Kg/sec (0.029 lbm/sec) giving a discharge specific power of approximately 150 KW/lbm/sec. Optical output may be limited by either the onset of discharge instabilities or gas heating. Gas heating appears to limit discharge specific powers to the range 200-300 KW/lbm/sec [85]. In closed cycle systems, however, discharge generated impurities tend to reduce the stable power loading [86]. One form of discharge instability expected for the segmented electrode structures of this thesis was the break-up of the discharge into discrete columns at high pressure and/or high discharge current. Sufficient power loading was unavailable to produce this condition. For the parameters of Figure 3.22 there was no visual evidence of filamentation of the discharge.

In summary, reasonably efficient (>5% overall) laser operation was obtained for the transversely excited cross-flow system. Even greater efficiency and power were expected for an optimized output coupling and a larger discharge specific power. High order modes were produced from a 2-path stable resonator. High power single mode operation was achieved with a single pass unstable resonator. The maximum output of 400 W clearly did not represent the maximum volumetric efficiency obtainable from this system.

REFERENCES

1. T.J. Bridges and C.K.N. Patel, "High-Power Brewster Window Laser at 10.6 Microns", Appl. Phys. Lett., Vol. 7, No. , p. 244, November 1965.

2. P.K. Cheo and H.G. Cooper, "Gain Characteristics of CO_2 Laser Amplifiers at 10.6 Microns", IEEE J. Quantum Electronics, Vol., OE-3, No. 2, p. 79, February 1967.

3. D.L. Franzen and R.J. Collins, "Radial Gain Profiles in CO_2 Laser Discharges", IEEE J. Quantum Electronics, Vol. QE-8, No. 4, April 1972.

4. A.G. Sviridov, N.N. Sobolev, and G.G. Tselikov, "Plasma Gas Temperatures in the Discharges Used for CO_2 Lasers", JETP Lett., Vol. 6, No. 3, p. 62, August 1967.

5. W.J. Wiegand, M.C. Fowler, and J.A. Benda, "Carbon Monoxide Formation in CO_2 Lasers", Vol. 16, No. 6, p. 237, March 1970.

6. A.J. Laderman and S.R. Byron, "Temperature Rise and Radial Profiles in CO_2 Lasers", J.Appl. Phys., Vol. 42, No. 8, p. 3138, July 1971.

7. J.H. Waszink and J.A.J.M. van Vliet, "Measurements of the Gas Temperatures in CO_2-N_2-He and CO_2-N_2-H_2O-He Discharges," J.Appl. Phys., Vol. 42, No. 9, p. 3374, August 1971.

8. J.Wilson, "Nitrogen Laser Action in a Supersonic Flow", Appl. Phys. Lett., Vol. 8, No. 7, p. 159, April 1966.

9. W.B. Tiffany, R. Targ, and J.D. Foster, "Kilowatt CO_2 Gas-Transport Laser", Appl. Phys. Lett., Vol. 15, No. 3, p. 91, August 1969.

10. T.A. Cool and J.A. Shirley, "Gain Measurements in a Fluid Mixing CO_2 Laser System", Appl. Phys. Lett., Vol. 14, No. 2, p. 70, January 1969.

11. T.F. Deutsch, F.A. Horrigan, and R.I. Rudko, "CW Operation of High-Pressure Flowing CO_2 Lasers", Appl. Phys. Lett., Vol. 15, No. 3, p. 88, August 1969.

12. C.J. Buczek, R.J. Wayne, P. Chenausky, and R.J. Freiberg, "Magnetically Stabilized Cross-Field CO_2 Laser", Appl. Phys. Lett., Vol. 16, No. 8, p. 321, April 1970.

13. H.J. Seguin and G. Sedgwick, "Low Voltage Gas Transport TE CO_2 Laser", Appl. Optics, Vol. 11, No. 4, p. 745, April 1972.

14. C.O. Brown, "High-Power CO_2 Electric Discharge Mixing Laser", Appl. Phys. Lett., Vol. 17, No. 9 p. 388, November 1970.

15. A.E. Hill, "Uniform Electrical Excitation of Large-Volume High-Pressure Near-Sonic CO_2-N_2-He Flowstream", Appl. Phys. Lett., Vol. 18, No. 5, p. 194, March 1971.

16. C.O. Brown and J.W. Davis, "Closed-Cycle Performance of a High-Power Electric-Discharge Laser", Appl. Phys. Lett., Vol. 21, No. 10, p. 480, November 1972.

17. B.F. Gordietz, N.N. Sobolev, V.V. Sokovikov, and L.A. Shelepin, "Population Inversion of the Vibrational Levels in CO_2 Lasers", IEEE J.Quantum Electronics, Vol. QE-4, No. 11, p. 796, November 1968.

18. H.W. Liepmann and A. Roshko, "Elements of Gas dynamics" (Wiley, New York, 1957)

19. R.J. Carbone and W.J. Witteman, "Vibrational Energy Transfer in CO_2 Under Laser Conditions With and Without Water Vapor", IEEE J. Quantum Electronics, Vol. QE-5, No. 9, p. 442, September 1969.

20. J. Tulip, "Gain Saturation of the Carbon Dioxide Laser", Vol. QE-6, No. 4, p. 206, April 1970.

21. M.C. Fowler, "Influence of Plasma Kinetic Processes on Electrically Excited CO_2 Laser Performance", J. Appl. Phys., Vol. 43, No. 8, p. 3480, August 1972.

22. W.G. Vincenti and C.H. Kruger, "Introduction to Physical Gas Dynamics"(Wiley, New York, 1965).

23. R.N. Schwartz, Z.I. Slawsky, and K.F. Herzfeld, "Calculation of Vibrational Relaxation Times in Gases", J. Chem. Phys., Vol. 20, No. 10, p. 1591, October 1952.

24. W.J. Witteman, "Vibrational Relaxation of Carbon Dioxide", J. Chem. Phys., Vol. 35, p. 1, July 1961.

25. P.O. Hocker, M.A. Kovak, C.K. Rhodes, G.W. Flynn, and A. Javan, "Vibrational Relaxation Measurements in CO_2 Using an Induced Fluorescence Technique", Phys. Rev. Lett., Vol. 17, p. 233, August 1966.

26. P.K. Cheo, "CO_2 Lasers" Lasers, Vol. 3, (Marcel Dekker, New York, 1971) p. 151.

27. W.A. Rosser, E. Hoag, and E.T. Gerry, "Relaxation of Excess Populations in the Lower Laser Level CO_2 (100)", J. Chem. Phys., Vol. 57, No. 10, p. 4153, November 1972.

28. R.L. Taylor and S. Bitterman, "Survey of Vibrational Relaxation Data for Processes Important in the CO_2 - N_2 Laser System", Rev. Mod. Phys., Vol. 41, No. 1, p. 26, January 1969.

29. W.A. Rosser, A.D. Wood, and E.T. Gerry, "Deactivation of Vibrationally Excited Carbon Dioxide (ν_3) by Collisions with Carbon Dioxide or with Nitrogen", J. Chem. Phys., Vol. 50, No. 11, p. 4996, June 1969.

30. R.L. Kerber, N. Cohen and G. Emanuel, "A Kinetic Model and Computer Simulation for a Pulsed DF-CO_2 Chemical Transfer Laser", IEEE J. Quantum Electronics, Vol. QE-9, No. 1, January 1973.

31. C.B. Moore, R.E. Wood, B. Hu, and J.T. Yardley, "Vibrational Energy Transfer in CO_2 Lasers", J. Chem. Phys., Vol. 46, No. 11, p. 4222, June 1967.

32. P.K. Cheo, "Relaxation of CO_2 Laser Levels by Collisions with Foreign Gases", IEEE J. Quantum Electronics, Vol. QE-4, No. 10, October 1968.

33. W.A. Rosser, R.D. Sharma, and E.T. Gerry, "Deactivation of Vibrationally Excited Carbon Dioxide (001) by Collisions with Carbon Monoxide", J. Chem. Phys., Vol. 54, No. 3, p. 1196, February 1971.

34. W.A. Rosser and E.T. Gerry, "De-excitation of Vibrationally Excited $CO_2(\nu_3)$ by Collisions with He, O_2 and H_2O", J. Chem. Phys. Vol. 51, p. 2286, 1964.

35. W.L. Nighan, "Electron Energy Distributions and Collision Rates in Electrically Excited N_2, CO, and CO_2", Phys. Rev. A, Vol. 2, No. 5, p. 1989, November 1970.

36. M. C. Gower and A.I. Carswell, "Vibration-Translation Rates in CO_2 Glow Discharges", Appl. Phys. Lett., Vol. 22, No. 7, p. 321, April 1973.

37. K.R. Manes and H.J. Seguin, "Analysis of the CO_2 TEA Laser", J. Appl. Phys., Vol. 43, No. 12, p. 5073, December 1972.

38. G. Herzberg, "Molecular Spectra and Molecular Structure" (Van Nostrand, Princeton, New Jersey, 1950), Vol. I, p. 125 and Vol. II, p. 395.

39. E.T. Gerry and D.A. Leonard, "Measurement of 10.6μ CO_2 Laser Transition Probability and Optical Broadening Cross-Sections", Appl. Phys. Lett., Vol. 8, No. 9, p. 227, May 1966.

40. A. Maitland and M.H. Dunn, "Laser Physics" (North-Holland, Amsterdam, 1969) pp. 180, 384.

41. A.E. Siegman, "An Introduction to Lasers and Masers" (McGraw-Hill, New York, 1971) pp. 120, 359.

42. J.A. Owczarek, "Fundamentals of Gas Dynamics", (International, Scranton, Pennsylvania) p. 236.

43. A. Ralston, "A First Course in Numerical Analysis" (McGraw-Hill, New York) p. 189.

44. A.C. Eckbreth and F.S. Owen, "Flow Conditioning in Electric Discharge Convection Lasers", Rev. Sci. Instr., Vol. 43, No. 7, p. 995, July 1972.

45. R.G. Standerwick and W.J. King, "Superchargers for Aircraft Engines", Trans. A.S.M.E., Vol. 66, p. 61, January 1944.

46. A.J. Stepanoff, "Turboblowers", (Wiley, New York, 1955)

47. A.B. Cambel and B.H. Jennings, "Gas Dynamics" (Dover, New York, 1958) p. 275.

48. T.M. Stickney, "Recovery and Time-Response Characteristics of Six Thermocouple Probes in Subsonic and Supersonic Flow", NACA TN 3455, July 1955.

49. Reference [47], p. 61

50. R.J. Carbone, "Long-Term Operation of a Sealed CO_2 Laser", IEEE J. Quantum Electronics, Vol. QE-3, No. 9, p. 373, September, 1967.

51. N. Karube and E. Yamaka, "Mass Spectrometric Studies of a Sealed CO_2 Laser", J. Appl. Phys., Vol. 41, No. 5, p. 2031, April 1970.

52. G. Francis, "The Glow Discharge at Low Pressure", H. der Physik, Vol. XXII, p. 147.

53. W.C. Roman and T.W. Myers, "Experimental Investigation of an Electric Arc in Transverse Aerodynamic and Magnetic Fields", AIAA Jr., Vol. 5, No. 11, p. 2011, November 1967.

54. R.H. Bullis, W.L. Nighan, M.C. Fowler, and W.J. Wiegand, "Physics of CO_2 Electric Discharge Lasers", AIAA Jr., Vol. 10, No. 4, P. 407, April 1972.

55. P.O. Clark and M.R. Smith, "An Investigation of the Effect of Gas Additives on the Electron Temperature and Density in a CO_2 Laser Discharge", Appl. Phys. Lett., Vol. 9, No. 10, p. 367, November 1966.

56. A.I. Carswell and J.I. Wood, "Plasma Properties of a CO_2 Laser Discharge", J. Appl. Phys., Vol. 38, p. 3028, 1967.

57. P. Bletzinger and A. Garscadden, "The CO_2 Laser Plasma", IEEE Proc., Vol. 59, No. 4, p. 675, April 1971.

58. M.Z. Novgorodov, A.G. Sviridov, and N.N. Sobolev, "Electron Energy Distribution in CO_2 Laser Discharges", IEEE J. Quantum Electronics, Vol. QE-7, No. 11, p. 508, November 1971.

59. J.H. Noon, R.R. Blaszuk, and E.H. Holt, "Electron Radiation Temperature Measurements in a CO_2 Laser Amplifier", J. Appl. Phys., Vol. 39, No. 12, p. 5518, November 1968.

60. D.C. Tyte and R.W. Sage, "Electron Temperature Measurements in CO_2 Laser Plasmas", Proc. IERE Conf. on Lasers and Opto-Electronics (Southampton, England, March 1969), No. 14 p. 238.

61. J. Polman and W.J. Witteman, "Electron-Radiation Temperature Measurements in a Sealed-Off CO_2 Laser System", IEEE J. Quantum Electronics, Vol. QE-6, No. 3, p. 154, March 1970.

62. P.O. Clark and J.Y. Wada, "The Influence of Xenon on Sealed-Off CO_2 Lasers", IEEE J. Quantum Electronics, Vol. QE-4, No. 5, p. 263, May 1968.

63. M.Z. Novgorodov, A.G. Sviridov, and N.N. Sobolev, "Electron Density and Collision Frequency in a CO_2 Laser", Soviet Phys. - Tech. Phys., Vol. 16, No. 4, p. 589, October 1971.

64. H.S.W. Massey, "Electronic and Ionic Impact Phenomena", Vol. II (Oxford University Press, 1969) p. 764.

65. E.E. Ferguson, F.C. Fehsenfeld, and A.L. Schmeltekopf, "Ion-Molecule Reaction Rates Measured in a Discharge Afterglow", Advances in Chemistry Series 80, (R.F. Gould, editor) American Chemical Soc. 1969, p. 83.

66. P.H. Dawson and A.W. Tickner, "Positive Ions in the Carbon Dioxide Glow Discharge", Proc. Intern. Conf. Ionization Phenomena in Gases, 6th, Paris France, Vol. 2, p. 79, July 1963.

67. H.E. Evans and P.P. Jennings, "Mass Spectrometric Study of the Species Present in R.F. Discharges in CO_2, CO and O_2", Trans. Faraday Soc. 61, 2153 (1965).

68. W.J. Wiegand, M.C. Fowler, and J.A. Benda, "Influence of Discharge Properties on CO_2 Laser Gain", Appl. Phys. Lett., Vol. 18, No. 9, p. 365, May, 1971.

69. J. Freudenthal, "Collision Processes in a CO_2 Laser Plasma", J. Appl. Phys., Vol. 41, No. 6, p. 2447, May 1970.

70. J.M. Austin and A.L.S. Smith, "Analysis of Positive Ions in CO_2 Gas Laser System", J. Phys. D. Appl. Phys., Vol. 5, p. 468, 1972.

71. P.D. Tannen, P. Bletzinger, and A. Garscadden, "Species Composition in a CO_2 Laser Discharge", Third Conf. on Chemical and Molecular Lasers, St. Louis, Missouri, May 1972, paper MC-6.

P.D. Tannen, P. Bletzinger and A. Garscadden, "Species Composition in the CO_2 Discharge Laser", submitted to IEEE J. Quantum Electronics, obtained by private communication.

72. E.W. McDaniel, "Collision Phenomena in Ionized Gases", (Wiley, New-York, 1964) pp. 428, 446, 455.

73. R.M. Clements and P.R. Smy, "Electrostatic-Probe Studies in a Flame Plasma", J. Appl. Phys., Vol. 40, No. 11, p. 4553, October 1969.

74. G.J. Schulz and S.C. Brown, "Microwave Study of Positive Ion Collection by Probes", Phys. Rev., Vol. 98, No. 6, p. 1642, June 1955.

75. R.M. Clements and P.R. Smy, "Ion Current from a Collision-Dominated Flowing Plasma to a Cylindrical Electrode Surrounded by a Thin Sheath", J. Appl. Phys., Vol. 41, No. 9, p. 3745, August 1970.

76. S.C. Brown, "Basic Data of Plasma Physics" (Wiley, New York, 1959)

77. G.A. Garosi, G. Bekefi, and M. Schulz, "Response of a Weakly Ionized Plasma to Turbulent Gas Flow", Phys. Fluids, Vol. 13, No. 11, p. 2795, November 1970.

78. C.J. Buczek, R.J. Freiberg, P.P. Chenausky, R.J. Wayne, "Magnetic Stabilization of the Plasma Column in Flowing Molecular Lasers", IEEE Proceedings, Vol. 59, No. 4, p. 659, April 1971.

79. O. Sahni and W.C. Jennings, "Microwave Technique for Measuring Vibrational Temperature in Pulsed Nitrogen Discharges", Appl. Phys. Lett., Vol. 22, No. 8, p. 375, April 1973.

80. E.S. Gasilevich, V.A. Ivanov, E.N. Lotkova, V.N. Ochkin, N.N. Sobolev, and N.G. Yaroslavskii, "Carbon Dioxide Dissociation in a CO_2 Laser", Soviet Physics - Technical Phys., Vol. 14, No. 1 p. 86, July 1969.

81. A.Ralston, "A First Course in Numerical Analysis" (McGraw-Hill Book Company 1965), p. 189.

82. W.F. Krupke and W.R. Sooy, "Properties of an Unstable Confocal Resonator CO_2 Laser System", IEEE J. Quantum Electronics, Vol. QE-5, No. 12, December 1969.

83. F. Horrigan, C. Klein, R. Rudko and D. Wilson, "Windows for High-Power Lasers", Microwaves, Vol. 8, No. 1, p. 68, January 1969.

84. A.E. Siegman, "Stabilizing Output with Unstable Resonators", Laser Focus, Vol. 7, No.5, p. 42, May 1971.

85. A.C. Eckbreth and J.W. Davis, "RF Augmentation in CO_2 Closed-Cycle DC Electric-Discharge Convection Lasers", Appl. Phys. Letters, Vol. 21, No. 1, p. 25, July 1972.

86. P.Bletzinger, D.A. La Borde, W.F. Bailey, W.H. Long, P.D. Tannen, and A. Garscadden, "Influence of Contaminants on the CO_2 Electric Discharge Laser", submitted to IEEE J. Quantum Electronics, obtained by private communication.

87. N.G. Kulgein, "Ion Collection from Low-Speed Ionized Gas", AIAA Journal, Vol. 6, No. 1, p. 151, January 1968.

88. L. Sevigny, D. Heckman, and P. Caron, "Ion Density Measurements in the Wake of a Hypersonic Sphere", Can. J. Phys., Vol. 50, p. 2970, 1972.

89. A.E. Siegman and H. Y. Miller, "Unstable Optical Resonator Loss Calculations Using the Prony Method", Appl. Optics, Vol. 9, No. 12, p. 2729, December 1970.

Appendix 3-1

Electron Density of the Cross-flow Laser Plasma

Theory of Schulz and Brown

The theory of Schulz and Brown [74] was developed to account for collisions within the sheath, however, the theory was developed for a static plasma. The following equations are presented in reference [74] for collision dominated current flow:

$$I_i = \frac{2\pi\mu_i\varepsilon_o\ell_p V^2}{r_p^2\gamma^2} \tag{A3.1}$$

$$I_i = 2\pi r_p \ell_p J_r \left(\frac{a}{r_p}\right)\left(\frac{3}{2\alpha_s p}\right) \tag{A3.2}$$

$$J_r = en_i\left(\frac{kT_i}{2\pi M}\right)^{1/2} \tag{A3.3}$$

$$\gamma = \left[\left(\frac{a}{r_p}\right)^2 - 1\right]^{1/2} - \left(\frac{a}{r_p}\right) \ell n\left(\frac{a}{r_p} + \left[\left(\frac{a}{r_p}\right)^2 - 1\right]^{1/2}\right) \tag{A4.4}$$

I_i - ion current collected by probe

μ_i - ionic mobility

ε_o - permittivity of free space

ℓ_p - probe length

V - probe bias

r_p - probe radius

γ - function of the ratio of sheath radius, a, to probe radius, r_p, as given by expression (A3.4)

J_r - random current density within undisturbed plasma

T_i - ion temperature

n_i - ion number density

M - molecular weight of ions

α_s - scattering factor due to collisions within the sheath

p - gas pressure in millimeters of Hg.

The following expression derived by Kulgein [87] was used for α_s:

$$\alpha_s = \frac{9r_p \ln(\ell_p/r_p)}{8p\lambda_i(1+T_e/T_i)} \qquad \text{(A3.5)}$$

where λ_i is the ionic mean free path, and T_e, the electron temperature.

Equation (A3.4) was used in the form presented by Sevigny et al [88].

$$\frac{a}{r_p} = \exp\left[0.0451(\ln\gamma)^2 + 0.3663(\ln\gamma) + 0.7717\right] \qquad \text{(A3.6)}$$

The electron density ($n_i = n_e$) was calculated by the following procedure:

(1) γ was calculated from (A3.1)

(2) a/r_p from (A3.6)

(3) α_s from (A3.5)

(4) n_e by substituting above parameters and (A3.3) into (A3.2)

Theory of Clements and Smy

Clements and Smy [73] [75] have presented theories which take into account convection of ions into the sheath. Both a thick sheath and a thin sheath theory have been developed. The non-dimensional parameter $R\alpha^2\chi^2$ determines the regime of operation as outlined in Chapter 3, section 3.6. From Table 3-6, Chapter 3, section 3.6, thick sheath conditions prevailed for the probe dimensions and bias potentials used in this thesis. The following expression relates the collected ion current and the ion number density.

$$I_i = \frac{2\ell_p\left(\pi\mu_i\varepsilon_o\right)^{1/3}\left(n_i euV\right)^{2/3}}{\left(\ell n\, \frac{I_i}{2n_i eur_p\ell_p}\right)^{2/3}} \qquad \text{(A3.7)}$$

where u is the flow velocity, e, electronic charge, and the remaining symbols as defined previously.

Appendix 3-2

Design of a Single-ended Positive Branch Unstable Resonator

The procedure presented here is a special case but is representative of calculations used generally. The unstable resonator was designed around an existing concave mirror. Due to this restriction a slightly diverging output was necessary to increase the output coupling over the confocal case. The formulas were taken from Krupke and Sooy [82] and Siegman [84].

Specifications

The following parameters were dictated by the experimental system:

(1) Raduis of curvature, R_2, of concave mirror, M2

(2) approximate output coupling coefficient, δ

(3) resonator length, L

(4) laser cavity height, H

A diagram of the resonator is illustrated in Chapter 3, section 3.9.1. The unknown parameters are the radius of curvature, R_1, of the convex mirror, M1, and the hole diameter, D_3, of the output coupler, M3. The calculation procedure is outlined below.

Definition of Parameters

An equivalent Fresnel number [84] is defined for the symmetric case by

$$N_{eq} = \frac{N}{2}\left(M - \frac{1}{M}\right)$$

where N is the Fresnel number and M the one-way magnification factor.

Using equivalence relations defined in reference [89] the asymmetric or single-ended case becomes

$$N_{eq} = \frac{N_1}{4g_2}\left(M - \frac{1}{M}\right) \qquad \text{(A3-8)}$$

$$N_1 = \frac{D_1^{\,2}}{4\lambda L} \qquad \text{(A3-9)}$$

= Fresnel number of convex mirror, M1

D_1 = effective diameter of M1

λ = radiation wavelength = 10.6μm

$g_2 = 1 - L/R_2$

$g_1 = 1 - L/R_1$

M = round-trip magnification for single-ended output [84]

The mode output diameter can not exceed the cavity height, H, that is $D_1 \leq H/M$ where $D_1 = D_3$, the hole diameter in the output coupler M3. Substitution of (A3-9) into (A3-8) yields

$$N_{eq} = \frac{D_1^{\,2}}{16g_2\lambda L}\left(M - \frac{1}{M}\right) \qquad \text{(A3-10)}$$

From reference [84], N_{eq} is defined for transverse mode discrimination by

$$N_{eq} = m/2 \qquad \text{(A3-11)}$$

$m = 1, 3, 5, \ldots\ldots$

The magnification is given by the following approximate relationships [84],

$$\frac{M^2-1}{M^2} = \begin{cases} 1.44\delta - 0.44\delta^2 & (m=1) \\ 1.06\delta - 0.06\delta^2 & (m=3) \\ \delta & (m=5) \end{cases} \qquad \text{(A3-12)}$$

Calculation Procedure

(1) M was calculated from one of (A3-12) and the desired output coupling, δ.

(2) From (A3-11) and (A3-10), $D_1 = D_3$ was calculated.

(3) D_3 was optimized by adjustments of M, δ, and m to give a large mode volume subject to the condition $D_3 \leq H/M$.

(4) Having selected M, the parameter g_1 was calculated from the single-ended magnification [84],

$$M = 2g_1g_2 + (2g_1g_2(g_1g_2-1))^{1/2} - 1$$

(5) Finally R_1, the convex mirror radius, is given by

$$R_1 = \frac{L}{1 - g_1}$$

CHAPTER 4

CONCLUSIONS AND SUGGESTIONS FOR FUTURE RESEARCH

4.1 Summary of Results and Conclusions

The previous chapters reported the results of an investigation of glow discharge geometries applied transverse to the laser axis and subjected either to slow axial (along the laser axis) gas flow or to high velocity cross-flow.

Chapter 1 was introduced by a brief review of related CO_2 laser developments. This was followed by a discussion of various spatial regions of a DC cold-cathode glow discharge. The negative glow and Faraday dark space are regions of low laser gain. Most of the useful laser power is generated in the positive glow. The importance of a low cathode-fall potential was stressed for short discharge lengths where the potential fall can be greater than the potential across the positive glow or active medium, causing a great reduction in laser power efficiency. In addition, power dissipated in the cathode regions may cause considerable gas heating with subsequent lowering of the laser gain and output power.

Glow to arc transitions were discussed with respect to the power loading of a discharge generated between large area electrodes. Discharge input may be limited by a transition of the normal or abnormal glow discharge to the highly contracted arc mode. This causes damage to the electrode surfaces and a great reduction of the active medium. Cathode surfaces having low heats of sublimation or containing insulation inclusions appear to be conducive to the initiation of a glow to arc transition. Gas heating may also cause a transition by a local reduction of the plasma impedance. The high power dissipated in the cathode region contributes to this problem.

Significant energy transfer processes were also outlined in Chapter 1. These included vibration - vibration transfer between N_2, CO and the CO_2 asymmetric mode; the relaxation of the upper laser level (00^01) by intramolecular processes; the deactivation of the lower laser level (10^00) to translation via the bending mode; vibrational excitation by electron impact; and the deactivation of vibrational energy via collisions of the second kind with electrons. It was also pointed out that the published results of fractional energy transfer calculations indicate that an optimum average electron energy lies in the range 0.5 to 1 eV. Higher electron energies result in decreased laser efficiency as a larger fraction of the input power is coupled into electronic excitation.

Experimental investigations of CO_2 dissociation were reviewed with respect to the equilibrium dissociation fraction as a function of discharge current, gas pressure, and tube diameter (average electron energy). CO appears to be particularly beneficial in a discharge without N_2. CO vibrations have a large cross-section for excitation by electron impact. Resonant transfer of CO vibrational energy then takes place to the CO_2 asymmetric mode. The role of CO is reduced when N_2 is present. Oxygen plays an active role in electrode surface chemistry and can lead to the eventual depletion of CO_2 in a closed cycle system. In addition O_2 may be active in discharge chemistry producing such compounds as NO and N_2O which have been shown to be detrimental to discharge stability.

In Chapter 2, transverse (to the laser axis) DC glow discharge arrangements were applied to an axial (along the laser axis) open-cycle flow. Glow to arc transitions limited operation of the initial large area electrodes to low gas pressure (<1mm) and low current densities. To reduce this problem a segmented cathode was employed with a single strip anode. The remoteness of the containing side walls permitted the discharge to operate without a positive column. Wire mesh grids were installed between the anode and cathode to intensify the positive glow and therefore the laser gain and output power.

A model was set up to analyze the interaction of the grid with the discharge plasma. From this model it appeared that the grid attenuated the low-energy diffusion-dominated current of the Faraday dark space. Further, it had considerable control over ambipolar diffusion losses from the active medium and therefore the average electron energy. This was demonstrated by the variation of positive glow intensity with grid bias potential.

Various electrode materials and geometries were studied. This eventually led to a multi-element cathode, with individually ballasted elements, and a single strip anode, all of water-cooled copper. The cathode surfaces contained annular grooves in order to exploit the properties of a hollow cathode in that the cathode fall potential and negative glow length were reduced from the flat surface case.

The V-I characteristics of the discharge were extensively studied with respect to grid position, mesh size, bias potential, gas mixture, and total gas pressure. The grid exhibited stable control over the discharge when located just past the anode end of the negative glow, in what had formerly been the Faraday dark space. The mesh size was assumed to have been governed by the sheath thickness about each wire. The fact that stable operation occurred when the grid was separated from the positive glow by a thin but observable dark sheath suggested an overlapping of the sheaths from individual grid wires. Stable operation was possible with an electrically isolated grid. By applying a self-bias resistive network the range of stable operation was extended. The most efficient bias potentials were, however, still negative with respect to plasma potential.

The results of studies of laser gain and output power were also presented in Chapter 2. Both gain and laser power were increased by a factor of two to three over the no grid case. Maximum gain was observed at low discharge current while maximum power was obtained for high current, similar to the behavior of conventional tube lasers. A multimode output power of 3 W was obtained at 1 A and 550 V for $CO_2/N_2/He$ - 1.4/1.4/8.3 flowing axially at approximately 6.5 liters/sec. The discharge conversion efficiency was approximately 0.5%. This is low compared to the usual 15 to 20% for a conventional tube laser. Laser power was expected to rise considerably by moving the cathode elements closer together, extending the mode diameter to more closely match the grid to anode separation, and optimizing the output coupling. Power consumed in the cathode fall, however, was the primary cause of low efficiency. By considering only the power dissipated in the positive column and anode glow the efficiency rose to over 3%. Overall discharge efficiency could be improved by using a larger anode to cathode separation and an electrode material of lower fall potential, say a thermionically emitting surface.

By applying the same volumetric flow transverse to both the laser and discharge axes, a factor of two improvement in output power was observed over the axial case. It was assumed that this was due to convective heat removal and improved column to column uniformity with regard to CO_2 dissociation. The substantial improvement in performance observed with low cross-flow (<0.5m/sec) led to the high-velocity cross-flow system of Chapter 3.

In Chapter 3, a laser system was described in which a DC glow discharge transverse to the laser axis was subjected to high velocity closed-cycle cross-flow. The laser, the flow, and the discharge axes were mutually perpendicular. An order of magnitude improvement in volumetric and electrical conversion efficiency was obtained by employing convective cooling of the laser mixture.

Although large area electrodes, continuous across the full channel width, were employed initially, discharge power loading was again limited by glow to arc transitions. Individually ballasted multiple electrode assemblies for both the anode and cathode improved the power loading and stability. Observation of the performance of the large surface electrodes suggested that localized gas heating within the positive glow caused filamentation with rapid degeneration into a highly contracted arc. This points out the importance of flow uniformity in raising the useful power loading of the electrical discharge.

The anode consisted of copper pins mounted flush with the flow channel. The opposite channel wall contained an array of hollow cathodes, recessed into small diameter ceramic tubes. For low pressure operation (the order of 10mm) charged-particle losses to the tube walls confined the negative glow and Faraday dark space to the interior of the tubes and out of the laser volume. At higher pressure the role of these tubes was expected to be reduced since the cathode regions of the discharge contract towards the electrode surface with increasing gas density.

Further in Chapter 3, the effects of flow on positive glow luminosity were recorded photographically and correlated with discharge potential. For constant discharge current, the potential rose rapidly at low gas velocity. This was attributed to an increase in gas density upon lowering of the translational temperature by convective cooling. The gas density change was verified by translational temperatures recorded by a thermocouple scanned through the laser region. In the low velocity range (<10 m/sec) the positive glow attempted to preserve a high temperature low density core while bowing in the direction of flow. At a velocity of approximately 10 m/sec the column broke with a marked reduction in visible intensity. This was assumed to have resulted primarily from a sudden change of the electron density. The change may have been amplified by the effects of stepwise electronic excitation. Upon further raising of the gas velocity, the positive glow gradually intensified with a corresponding increase in E/N. The glow position was stable against the flow, contrary to the low velocity case. In this regime, charged-particle loss by diffusion and recombination was superceded by that due to convection. The gradual intensification of the glow suggested that the fractional power coupled into electronic excitation was likewise rising. Consequently, a discharge having short width (along the flow axis), and operating in the second regime, may show a gradual decrease of efficiency with flow velocity.

The electron density was investigated by sweeping an electrostatic probe through the discharge and afterglow. Ion saturation current was collected and analyzed by flow-dependent and static formulas to estimate the electron density. The probe had sufficient resolution to indicate structure introduced into the positive glow by the multi-element electrodes. As expected the structure increased and persisted for longer distances downstream as the gas velocity was raised. The spatial ripple in ionization density was reduced as the flow progressed past succeeding rows of electrodes. Upstream electrodes effectively preionized those downstream. Structure or ripple within the flowing afterglow disappeared in a distance of a few centimeters. In this connection lateral spreading of the ionization by ambipolar diffusion may have been augmented by diffusion due to turbulence of the flow. Calculated densities agreed qualitatively with those determined by standard microwave methods. A comparison was difficult due to the vastly different discharge geometries. Calculations were expected to give only order of magnitude accuracy in a determination of the absolute density in view of uncertainties involved with identification of the ionic species, the mobility of the ions, and the applicability of the formulas to this pressure and velocity regime.

The spatial behavior of the laser small-signal gain was studied by passing the beam of a low power oscillator along the laser axis and scanning in the direction of flow. Gain rose rapidly at the upstream edge of the discharge and decayed relatively slowly in the flowing afterglow; the rate of rise and decay being dependent on flow velocity, discharge current, and gas density. Maximum gain was approximately 2%/cm which compared with published results of other convection systems.

The gain at the spatial peak varied more or less linearly with low discharge current. Current saturation did occur which was attributed primarily to collisions of the second kind between the vibrationally excited species and electrons, rather than thermal effects. This contention was supported by records of the translational temperature and computed gains from a theoretical model of laser processes. This model was set up using vibrational energy balance equations incorporated into gas dynamic equations describing the flow. Substantial electron deactivation was required in the model to simulate the behavior of gain with discharge current. Good agreement was found with experiment on the spatial behavior of gain and translational temperature with flow rate. By employing electron densities calculated from the experimental data, rather poor agreement was found between an experimental effective vibrational excitation rate and that computed from published theoretical results for a somewhat different gas mixture. The agreement probably was substantially better since calculated densities appeared to be high by an order of magnitude. A more definitive comparison of the model and experiment is dependent on more accurate knowledge of electron densities and excitation rates for a given gas mixture.

Finally, in Chapter 3, laser output power was investigated for varying flow and discharge input using both stable and unstable resonator arrangements. Laser power with convective cross-flow showed at least an order of magnitude increase over that for diffusion-dominated flow. In addition the sensitivity of laser power to the gas constituents was greatly reduced. For constant discharge current, laser power showed a rapid rise with flow up to a certain velocity (≈30 m/sec) after which output remained nearly constant. The turnover point corresponded to a lowering of the translational temperature to a point where thermal effects were now small. For high velocities ($\approx$80 m/sec) output decreased, due primarily, it was assumed, to inefficient matching of the resonator to the active medium as a result of a limited laser aperture. Investigations were limited by power supply capability to pressures less than 30mm. Substantially higher volumetric efficiency was expected by increasing the gas density. This is dependent, however, on a high stable power loading of a high pressure discharge. The maximum power loading of the discharge was not reached for pressures less than 30mm. Power loadings used were, however, comparable with published results of other convective systems, that is, in the range of 150 - 200 KW/lbm/sec. Maximum laser power of near 400 W, with an overall efficiency of 5%, was obtained for a two path stable resonator, a flow velocity of 40 m/sec, and a mass flow of approximately 0.01 Kg/sec. This corresponded to approximately 1 W/cm^3 of mode volume compared with a value of 4 W/cm^3 published for the Buczek magnetically stabilized system. Greater discharge power loading improved heat exchangers, optimization of the output coupling, and improved matching of the mode volume and active medium were expected to substantially increase the volumetric efficiency of the cross-flow system described in this thesis.

4.2 Suggestions For Future Research

Further work is required to ascertain the maximum stable-discharge power loading of a convective cross-flow system employing multi-element electrodes as described in this thesis. In this connection, a study of power loading at higher pressures may lead to substantially higher output per unit volume since laser power is expected to scale with gas density.

Investigation is required on the role of flow turbulence in the production of or dissipation of discharge filamentation at high power loading. Flow conditioning may permit larger electrode surfaces providing a more uniform active medium and alleviating construction problems. Some very preliminary experiments on the cross-flow system indicated that upstream ionization may be useful for supporting a CW discharge between large area electrodes.

At present high-flow closed-cycle systems give improved output with the use of a small replacement or make-up flow. This appears to be connected to discharge generated impurities. An investigation of the role of these species on discharge stability and laser gain may lead to a reduction or elimination of replacement flow.

The above suggestions have concentrated on discharge stability, a major problem in the generation of large volume high pressure discharges. Theoretical and experimental work would also appear to be useful on the physics of the laser process. For, instance, the model outlined in this thesis may provide insight into the effects of convective flow on the saturation of the intra-cavity radiation field.

In conclusion, the above paragraphs suggest only a few of many topics for research in the continuing development of a compact high power CO_2 laser for industrial applications.